André Filipe Rato Bispo

Licenciado em Ciências da
Engenharia Electrotécnica e de Computadores

Using an LED as a Sensor and Visible Light Communication Device in a Smart Illumination System

Dissertação para obtenção do Grau de
Mestre em Engenharia Electrotécnica e de Computadores

Orientador: João Pedro Abreu de Oliveira, Professor Doutor, FCT-UNL

Júri:

Presidente:	Prof. Doutor Luís Augusto Bica Gomes de Oliveira, FCT-UNL
Arguente:	Prof. Doutor Carlos Manuel Ferreira Carvalho, ISEL
Vogal:	Prof. Doutor João Pedro Abreu de Oliveira, FCT-UNL

FACULDADE DE CIÊNCIAS E TECNOLOGIA
UNIVERSIDADE NOVA DE LISBOA

MARÇO, 2015

Using an LED as a Sensor and Visible Light Communication Device in a Smart Illumination System

Ao Vicente.

ACKNOWLEDGEMENTS

First and foremost, I would like to thank Professor João Pedro Oliveira for his support, patience, and words of encouragement when things went haywire. Also I cannot ignore all the people, from professors to faculty staff, who took part in this journey of mine. Thank you all.

I would also like to thank my dear colleagues, especially Filipe Quendera, Ricardo Madeira, Miguel Curvelo, and Daniel Batista who put up with me over this last stressful year. May we all watch our hair grow grey together.

To all my "Conhecidos do Velho do Restelo" friends, with whom I shared incredible moments over these past years. And to Daniel, for all the incredible film recommendations.

À minha família, que sempre me apoiou, não obstante o meu silêncio quando me perguntavam "Então, como vai a tese?". Ao meu pai, que me ensinou a soldar, e me incutiu o gosto pela electrónica e pela mecânica. À minha mãe, que nunca deixou de me apoiar e mostrou que se deve sempre trabalhar mais, e melhor [1]. À minha irmã, pelos conselhos sábios de quem já passou por aqui. Ao Marco, pelas noitadas de copos e PlayStation.

Ao João, ao Pedro e ao Bernardo, dos ALF, com quem partilhei muitas horas, muitos palcos, e muitos quilómetros de estrada nestes últimos 6 anos. Fizeram-me crescer enquanto músico e enquanto pessoa. Podemos não ter privado assim tanto neste último ano, mas nunca me esquecerei das histórias que partilhámos juntos.

Obrigado ao Blake Mills, ao Steve Reich, ao Rodrigo Amarante e ao B Fachada, pela *companhia*.

[1] Já agora, obrigado pela sopa.

ABSTRACT

The need for more efficient illumination systems has led to the proliferation of Solid-State Lighting (SSL) systems, which offer optimized power consumption. SSL systems are comprised of LED devices which are intrinsically fast devices and permit very fast light modulation. This, along with the congestion of the radio frequency spectrum has paved the path for the emergence of Visible Light Communication (VLC) systems. VLC uses free space to convey information by using light modulation. Notwithstanding, as VLC systems proliferate and cost competitiveness ensues, there are two important aspects to be considered.

State-of-the-art VLC implementations use power demanding PAs, and thus it is important to investigate if regular, existent Switched-Mode Power Supply (SMPS) circuits can be adapted for VLC use. A 28 W buck regulator was implemented using a off-the-shelf LED Driver integrated circuit, using both series and parallel dimming techniques. Results show that optical clock frequencies up to 500 kHz are achievable without any major modification besides adequate component sizing.

The use of an LED as a sensor was investigated, in a short-range, low-data-rate perspective. Results show successful communication in an LED-to-LED configuration, with enhanced range when using LED strings as sensors. Besides, LEDs present spectral selective sensitivity, which makes them good contenders for a multi-colour LED-to-LED system, such as in the use of RGB displays and lamps.

Ultimately, the present work shows evidence that LEDs can be used as a dual-purpose device, enabling not only illumination, but also bi-directional data communication.

Keywords: LED, Visible Light Communication, Solid-state Lighting, Internet-of-Things, IoT, Smart Lighting, Smart Grids, Low-Voltage Direct Current, Energy Efficiency, LED as Sensor

RESUMO

A procura por sistemas de iluminação cada vez mais eficientes levou à proliferação de sistemas de iluminação com dispositivos de estado sólido (SSL), devido à sua maior eficiência energética. O LED é um dispositivo integrante destes sistemas, e sendo um dispositivo inerentemente rápido, permite a modulação de luz a altas frequências. Esta característica, aliada ao recente congestionamento na banda de RF levou ao aparecimento de sistemas de Comunicação digital com Luz Visível (VLC). Estes sistemas usam o espaço como meio de transmissão de informação através da modulação de luz.

Contudo, e antes de mais, é necessário averiguar se os circuitos de alimentação para LED, baseados em topologias de fontes de alimentação comutadas (SMPS), podem ser adaptados para uso em sistemas VLC. Neste trabalho documenta-se a implementação de um regulador buck de 28 W usando um circuito integrado comercial. Resultados experimentais mostram que o circuito permite frequências de clock óptico até 500 kHz.

Adicionalmente, estuda-se também o comportamento de um LED enquanto fotodíodo. Resultados experimentais mostram comunicação entre dois LEDs, sendo que o alcance da mesma é reforçado caso se use uma montagem de múltiplos LEDs em série. Os LEDs apresentam uma elevada selectividade no que diz respeito à sua sensibilidade espectral, possibilitando o seu uso num sistema LED-LED em que haja uma pluralidade de cores, tal qual se encontraria num ecrã ou numa lâmpada RGB.

Em suma, este trabalho demonstra a possibilidade do uso de um LED enquanto um dispositivo não só de iluminação, mas também de comunicação.

Palavras-chave: LED, Visible Light Communication, Internet-of-Things, IoT, Smart Lighting, Low-Voltage Direct Current, Energy Efficiency, LED as Sensor

CONTENTS

List of Figures

List of Tables

ACRONYMS

μC Micro-controller.

AlInGaN Aluminium gallium indium nitride.

AlInGaP Aluminium gallium indium phosphide.

BER Bit error rate.

CLC Chip Level Conversion.

CMC Current-Mode Control.

CRI Colour Rendering Index.

CSK Colour Shift Keying.

DUT Device Under Test.

EMI Electromagnetic Interference.

ESD Electrostatic-sensitive device.

ESR Equivalent Series Resistance.

FDM Frequency Division Multiplexing.

GaAs Gallium arsenide.

GaN Gallium nitride.

GaP Gallium phosphide.

IM/DD Intensity Modulation/Direct Detection.

InGaP Indium gallium phosphide.

IoT Internet of Things.

LED Light Emitting Device.

lm Lumen.

LVDC Low-Voltage DC.

MFTP Maximum Flickering Time Period.

MSM Multiple-Subcarrier Modulation.

OFDM Orthogonal Frequency Division Multiplexing.

OOK On-Off Keying.

PA Power Amplifiers.

PFC Power Factor Correction.

PLC Power Line Communication.

PoE Power over Ethernet.

PPM Pulse Position Modulation.

PWM Pulse Width Modulation.

SCM Single-Carrier Modulation.

SMD Surface-mounted device.

SMPS Switch Mode Power Supply.

SNR Signal-to-noise ratio.

SSL Solid-State Lighting.

TRIAC Triode for Alternating Current.

UWB Ultra-Wide Bandwidth.

VLC Visible Light Communication.

VMC Voltage-Mode Control.

VPPM Variable Pulse Position Modulation.

WDM Wavelength-division Multiplexing.

CHAPTER 1

INTRODUCTION

1.1 Background and Motivation

The ongoing search for *greener* technologies is crescent. With the demand for more sustainable energy generation provided by renewable energy sources such as solar and wind energy, the end-user energy consumption paradigm has changed. Energy efficiency is now a part of our everyday vocabulary, and not only must the energy source be as least intrusive as possible regarding our planet's natural resources, the end-user must also be able to seize this harvested energy as best as he can.

Solid-State Lighting (SSL), using LED technology, and the concept of Smart Lighting are part of this tendency. Illumination costs for buildings urbanized areas are immense. The use of LED technology in such an important aspect of our daily lives - illumination - allows for a significant increase in power efficiency, also reducing long term costs such as maintenance, due to their long lifetime. The concept of Smart Lighting adds to the former, with the possibility, from the user's standpoint, to adjust lighting not only to a specific use but to a specific time usage profile.

The recent trend of Internet of Things (IoT) [1, 2] and Smart Grids [3, 4], together with SSL and Smart Lighting, envisions the merge of sensor networks, smart appliances, portable devices and illumination. In that regard comes Visible Light Communication (VLC). The modulation of such a non-intrusive electromagnetic radiation (in the visible spectrum), permits the de-congestion of other, mainly in the radiowave spectrum. After all, VLC is merely taking advantage of such an important hallmark of modern civilization that is artificial lighting and doubling

its purpose, not only as a means of illumination, but also as a communication means.

Motivation for this thesis branches on two aspects which, given the newness of VLC, have not been much discussed in the literature. Firstly, the LED Driver. The existent LED-based luminaires and LED lighting systems use driving circuitry based on Switch Mode Power Supply (SMPS) topologies. These allow for very high efficiencies, and in most cases are compatible with Smart Lighting systems, enabling the dimming of light intensity [5]. Thus, the most direct approach to VLC would be to use the existing circuits. However, the frequencies at which these circuits operate are limited to the tens of kHz, enabling low data rates. The state-of-the-art VLC systems use modulation frequencies up to MHz, and require the use of high-speed Power Amplifiers (PA) [6, 7], which are current demanding and go against the entire notions of energy efficiency in a joint illumination/communication system. Therefore, it is necessary to investigate whether the current, off-the-shelf SMPS circuits can be applied to VLC systems, and if so, what changes (if any) are required. A LED Driver based on an off-the-shelf LT3763 (Linear Technologies) was designed and tested, using two different PWM Dimming techniques.

Secondly, the VLC receiver. State-of-the-art VLC systems use either PIN or Avalanche photodiodes, which offer increased sensibility and response over common photodiodes and phototransistors. However, they lack cost competitiveness, especially if their spectral sensitivity lies in the visible range (as opposed to the IR or UV range). It it thus necessary to find alternative, low-cost solutions. Exploring the concept of *electroluminescence* on semiconductor devices, light sensitivity on LEDs was investigated. As remarked by Mims [8, 9, 10], LEDs behave as spectral selective photodiodes, and a similar technique was used by Dietz et al. [11]. LED constraints, such as construction types and presence or absence of Electrostatic-sensitive device (ESD) protection, as well as the behaviour of multiple LEDs (either in series, or parallel) were studied and are thoroughly documented below.

1.2 Thesis Organization

This present thesis summarizes a first approach to a joint VLC and illumination system, and exposes some essential considerations. Considering this framework, the following thesis is organized in a total of 6 chapters, excluding this introductory one.

Chapter 2 introduces basic concepts such as SSL and Light Generation, as well

as a more in-depth analysis on VLC. Chapter 3 provides insight on the LED device and its respective driver, as well as considerations about the use of both in VLC systems.

Chapter 4 presents a thorough review on using and LED as a light sensor. Circuit topologies, the effects of junction capacitance and physical constraints on performance are detailed, along with experimental results that show LEDs' response to light of different wavelengths. A SPICE model is also proposed to assess LED discharge waveforms when used as sensors, in series or parallel.

Chapter 5 describes the proposed VLC system, which includes the LED Driver, the LED String and a Micro-controller (μC) as its main blocks. The sizing of the LED String and LED Driver are detailed in extent. Additionally, a developed Simulink model is shown for the LED Driver. Finally, remaining building blocks as well as their integration in Low-Voltage DC (LVDC) grids are documented.

Following, Chapter 6 shows details on the Driver's circuit board layout, as well as the obtained experimental results. Finally, a Low Data-Rate LED-to-LED communication configuration is described. Symbol Width was reduced to $t = 100\ \mu$s, improving raw data-rate reported by other systems in the literature. The use of multiple LEDs in series is shown to enable communication ranges up to 90 cm.

Finally, Chapter 7 summarizes the conclusions obtained from the developed work, and oversees further work.

Appendixes A and B illustrate details on compensation networks for Voltage-Mode Control (VMC) regulators and the proposed driver's final schematics. Appendix C lists the code of the LED-to-LED configuration.

1.3 Contributions

The development of this thesis allowed for a deeper understanding of VLC networks, LEDs, p-n junctions and their reverse-bias characteristics, as well as the behaviour and working principle of DC-DC converters and its intricacies. Furthermore, it has allowed the author to develop his SMD soldering and PCB layout skills, as well as the opportunity to participate in every stage of a prototype design - from electrical simulation, to manufacture and experimental validation.

Chapter 4, 5 and 6, which comprise the LED-as-sensor study, system analysis and its implementation originated a paper entitled *Using an LED as a Sensor and Visible Light Communication Device in a Smart Illumination System* which has been submitted to the *IEEE Transactions on Industrial Electronics* journal for review.

CHAPTER 2

SMART LIGHTING: A SYSTEM OVERVIEW

2.1 Artificial Lighting

The chronology of artificial lighting can be decomposed in three unique periods. The first one being the discovery of fire itself. It gave Man not only light, but shelter, security, and a means to cook. First torches, which consisted of a burning fibre cloth soaked in molten fat, date back 5×10^5 years. Oil and gas lamps make up the second period, which saw its decline to start around the end of the XIX century. In fact, the first electrical and solid-state lighting devices were documented throughout the XIX century, paving the way for the filament and gas discharge lamps that would follow. Hence, the third period. With the advent of electricity, incandescent lamps (Edison, Thomas and Swan, Joseph, ca. 1879) and mercury vapour lamps (Hewitt, Peter ca. 1901) were realized, and for the first time permitted light production without combustion, odour or smoke [12]. The XX century saw the birth of many other light sources, including low- and high-pressure sodium vapour lamps (1919,1964), fluorescent tubes and compact fluorescent lamps (1927,1997), but the main revolution is said to be the solid state lighting device known as the LED. Some of these are depicted in Figure 2.1.

Figure 2.1: Lamp examples (not at scale). From left to right: incandescent lamp, sodium vapour lamp, CFL lamp, LED lamp.

2.1.1 Solid-state Lighting

SSL describes light production using semiconductor devices, mainly LEDs[1]. SSL Lighting has a number of advantages over older technologies - such as incandescent and fluorescent - mainly smaller footprint, higher luminous efficiency and longer lifetime. Although gas discharge lamps generally have higher luminous efficiencies, they have lower Colour Rendering Index (CRI) [13].

Whereas filament, vapour and fluorescent lamps are examples of both *incandescence* and *gas discharge*, light emission in LEDs is due to a transversely different physical phenomenon, called *electroluminescence*. The first known report of electroluminescence, which marks the birth of the first LED, dates back to 1907, by Henry Round. During experiments with current flow through silicon carbide (SiC), Round noticed that a voltage potential of $\sim$10 V caused the emission of a yellowish light by the crystallite. Oleg Losev reported further detailed investigations (1927) of this luminescence phenomenon, and noted that this light could be switched on and off at significant speeds. By 1962, compound semiconductors such as the Gallium nitride (GaN), Gallium phosphide (GaP) and the Gallium arsenide (GaAs) were used in red, amber and green LED production. By the 1990s, heterojunction applications with as Indium gallium phosphide (InGaP), Aluminium gallium indium phosphide (AlInGaP) and Aluminium gallium indium nitride (AlInGaN) revolutionized LED production, culminating in the production of a blue LED which, by that time, was considered by many as impossible to manufacture. The production of the blue LED is a fundamental cornerstone in semiconductor devices - now that the missing wavelength (blue) had been achieved, white light creation by LEDs was finally possible (Chapter 1) [12].

[1]LEDs can be produced using either inorganic or organic materials - the former are hence called OLEDs (Organic LEDs). However, for the purposes of this thesis, attention will be focused on the inorganic technology - simply LED.

White Light Generation

White light is the electromagnetic radiation of all wavelengths that fall in the visible region of the electromagnetic spectrum (380 - 700 nm). While *incandescent* and *gas discharge* light sources emit over a broad wavelength spectrum, LEDs have a very narrow emission band, and thus white light generation is achieved either (i) by colour mixing or (ii) by *fluorescence*. White light production via colour mixing can be achieved by using different coloured LEDs simultaneously (blue+yellow or red+green+blue colour mixtures). White light production via fluorescence involves the use of a phosphorous layer on top of a single blue LED [2]. The phosphor layer absorbs the most higher energy blue radiation, and emits a yellowish, lower energy radiation. Both non-absorbed blue radiation and yellow radiation mix, producing white light. Figure 2.2 shows the emission spectrum of a white LED (blue chip with added phosphor). Note the spectral peaks at 440 and 550 nm, resultant from blue chip and the blue+yellow colour mixing respectively.

The former method allows good control over the desired colour of the light (or, specific to white light, colour temperature), although its CRI [3] and luminous efficiency are mediocre. CRI can be improved by adding extra LEDs, such as amber, or yellow. Additionally, associated circuitry is more complex. The latter method is of very simple implementation and has significant improvements on both luminous efficiency and CRI (70-90). It does, however, permit small colour temperature variations (Chapter 15) [12].

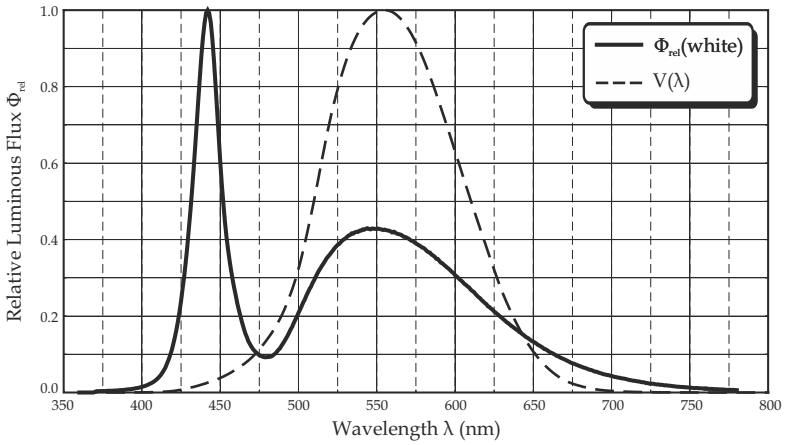

Figure 2.2: White LED Emission Spectrum, and Photopic Vision Curve (from [14]).

[2] The same concept is used in fluorescent lamps, where UV light excites internal phosphorous coating

[3] Colour Rendering is a light source's ability to reproduce the colours of the lit objects comparatively to an ideal light source. The CRI is its associated quantitative unit, and has a maximum value of 100

2.1.2 Smart Lighting

Smart lighting is a design philosophy driven towards energy efficiency. It spans from using high-efficiency lamps, to the use of daylight sensors, to automatic occupancy sensing. Smart lighting fits in the concept of *Building Automation*, as does IoT.

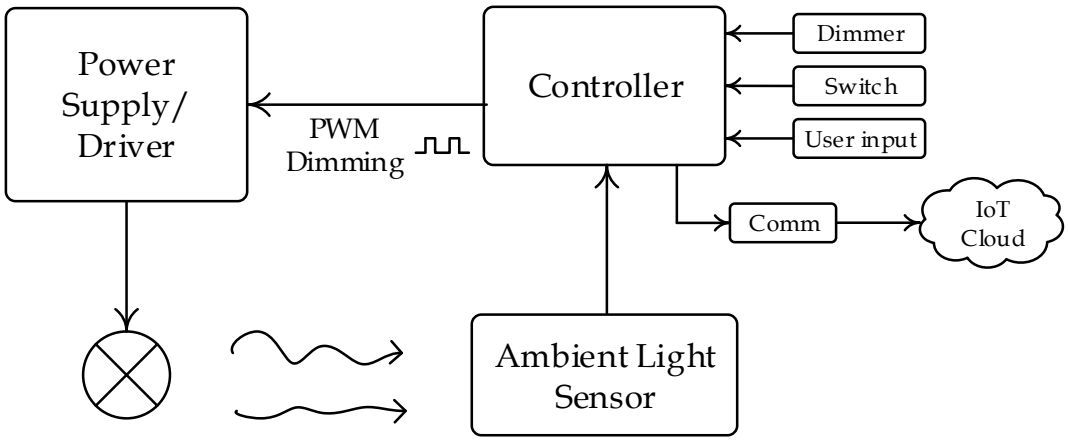

Figure 2.3: Typical Smart Lighting System.

Dimming is one of the basic functions of Smart Lighting. Dimming an AC load such as an incandescent lamp is rather straightforward, accomplished by using Triode for Alternating Current (TRIAC)s, or auto-transformers. Dimming fluorescent lamps is somewhat complicated, as it requires ballast internal frequency adjustment, before DC-AC conversion. LEDs, on the other hand, are very simple to dim. As they are a constant-current load, dimming can be done simply by altering their forward current. There is, however, one drawback to this method as forward current altering leads to colour shifts in the emission wavelength. Therefore, an alternative way can be put in practice, using LED's inherent fast response. By switching LEDs on and off, and controlling the on-time, dimming is achieved. In reality, LED Dimming is very similar to TRIAC dimming of incandescent lamps - dimming is achieved by controlling the time where the load is on - thus, by adjusting the pulse's width. However, given the LED's fast response, switching can be done at much higher frequencies.

Dimming under a Smart Lighting scheme can be achieved both ways: either by manual user input, or by sensor network feedback. DALI and DMX512 are examples of existent standardized interfaces for lighting control [13]. A typical example of Smart Lighting using sensor networks is to have light sensors scattered around a workplace, measuring ambient light, which then feed this information back into the main controller (Figure 2.3). Artificial light is then adjusted accordingly. As

daylight changes throughout the day, so should the artificial lighting. Furthermore, different rooms and areas may require a higher or a lower lighting level. An area close to a window that has sufficient daylight penetration may not need as much artificial lighting as a confined room within the interior of the building.

However, and in an IoT and Smart Lighting perspective, efficient lighting through dimming is the not the only benefit LEDs can provide, as seen in the following section.

2.2 Visible Light Communication

Light-based communication dates back to 1880 and Alexander Bell's invention - the Photophone - which allowed for the transmission of sound via light modulation. Fiber-optic communication, for instance, also employs modulated visible light, although through a physical means of transmission. VLC, however, explores data communication using light in free space. With the proliferation of LEDs and LED fixtures, and due to their susceptibility to current modulation at frequencies high enough in order to guarantee meaningful data rates, without compromising their main illumination function, VLC has seen increased interest [7]. In fact, VLC builds on a previously proposed high-speed wireless digital communication using infrared radiation [15].

VLC relies on visible electromagnetic radiation to convey information in free space. The transmitter converts an electric signal into an optical signal, and the receiver converts the optical power back into an electrical current (in a process called Intensity Modulation/Direct Detection (IM/DD)), and its big challenge is to accomplish this using incoherent, off-the-shelf devices [7, 16]. As stated earlier, white light generation using LEDs results by phosphorescent or RGB LEDs. Due to the slower response of the phosphorescent material, VLC modulation bandwidth may be compromised. On the other hand, by using RGB LEDs, three individual colour channels are formed, resulting in a higher system throughput, notwithstanding the added system complexity.

VLC has many advantages over other communication systems. Firstly, the available visible light bandwidth is vast - it spans from 380 to 700 nm, which translates into a frequency bandwidth of roughly 360 THz[4] (as seen in Figure 2.4). Furthermore, given it is a *visible* means, available to all, it is not licensed.

[4]The visible light spectrum of 380-700 nm translates into a frequency range of 789-428 THz, which is broader than the RF bandwidth by 1200 times.

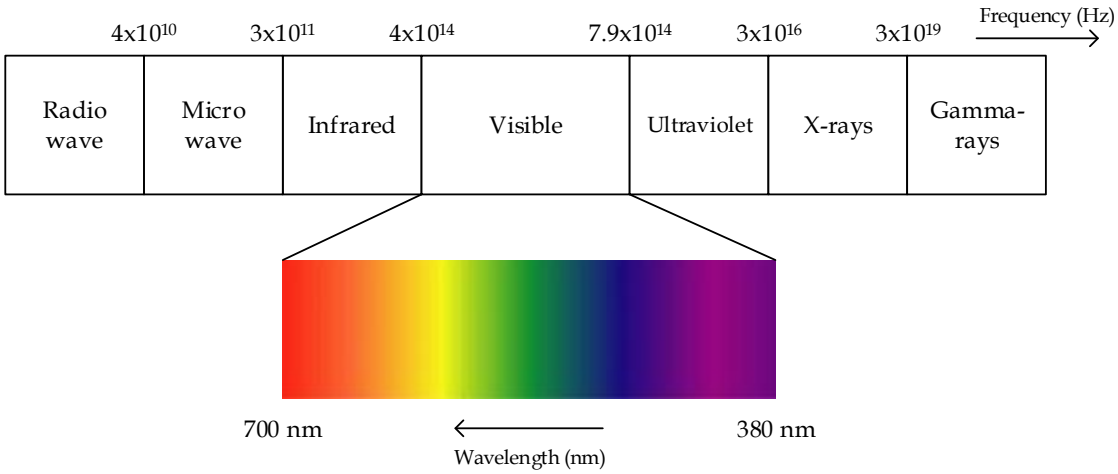

Figure 2.4: Electromagnetic spectrum and its respective regions.

Secondly, there is minimal susceptibility to Electromagnetic Interference (EMI) with existing radio systems, permitting its use in sensitive areas, such as aircrafts, and hospitals. Finally, its inability to transmit through opaque materials, such as walls, permits VLC to be a high security communication system. VLC, however, does not come without constraints - like all systems, it suffers from noise. Any light source, including sunlight light, adjacent lamps, and monitors emit photons which are collected by the receiver's detector, and cannot be separated from the VLC transmitter's photons. Although constant intensity sources impose a DC offset that can be easily filtered, spurious light is a completely different matter, and filtering in both electrical and optical domains must be carried out. Additionally, the optical characteristics of VLC systems cause the receiver's Signal-to-noise ratio (SNR) to be inherently dependent on propagation distance - or channel length - which consequently limit its data-rate. VLC, is not, however a disruptive technology, as is not aimed to replace existent RF communications. Instead, it should be thought of as a complement to existing RF systems. Given its broad bandwidth, and inability to transmit through walls it should provide a far higher spatial density of communication rates, compared to RF, [7]. However, its ability to transmit over long links is limited, contrarily to RF. It is the integration of VLC with existing systems that will determine its success.

The potential for VLC is immense, and various VLC applications have surfaced.

- *Li-Fi*, VLC's equivalent to Wi-Fi, this would allow Internet access to areas where radio communication is forbidden, such as Hospitals, Chemical Plants, or even aircrafts.

- Automotive Lighting for Vehicle Safety has been proposed in [17, 18], with

V2I (Vehicle-to-Infrastructure) and V2V (Vehicle-to-Vehicle) applications.

- Indoor GPS - by data transmission via the building's lighting system, indoor GPS positioning is possible. By using low data-rates, and taking advantage of cameras' positions on portable devices (such as smartphones), indoor positioning is possible at very low-costs, as both physical structures (the building's lighting system as a transmitter and the smartphones as the receiver) already co-exist [7, 19].

As of September 2011 the IEEE 802.15.7 Visible Light Communication Task Group published the IEEE Standard for VLC, where both PHY and MAC layers are defined. This standard supports high-data-rate visible light communication up to 96Mb/s [20, 21]. Some important and inherent aspects of VLC are discussed below.

2.2.1 Network Topologies

Three distinct device classes are considered for VLC, as shown in Table 2.1

Table 2.1: VLC Device Classification

	Infrastructure	Mobile	Vehicle
Fixed Coordinator	Yes	No	No
Power Supply	Ample	Limited	Moderate
Form Factor	Unconstrained	Constrained	Unconstrained
Light Source	Intense	Weak	Intense
Physical mobility	No	Yes	Yes
Range	Short/long	Short	Long
Data rates	High/low	High	Low

These three distinct devices classes may interact mutually via three different topologies: *peer-to-peer*, *star* and *broadcast*. These are depicted in Figure 2.5.

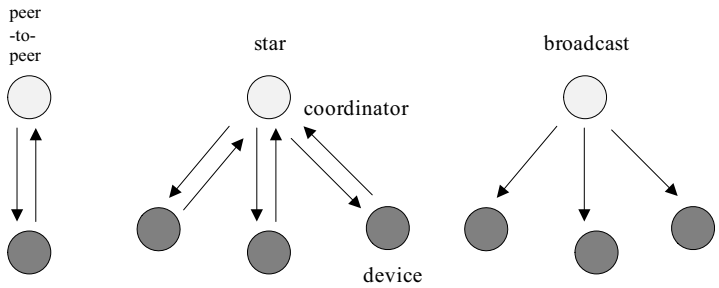

Figure 2.5: Supported MAC topologies.

Peer-to-peer topology

In this topology, each device is capable of communicating with any other device within its coverage area, and one of the peers acts as a coordinator [21].

Star topology

All star networks operate independently from all other nearby star networks currently in operation, by choosing a VPAN identifier that is not currently used by any other network within the coverage area. Once the VPAN identifier is chosen, the coordinator allows other devices to join the network [21].

Broadcast topology

A device in a broadcast mode can transmit a signal to other devices without forming a network - communication is uni-directional and the destination address is not required [21].

2.2.2 PHY Layer Types

Three different PHY Layer types can coexist, although they do not interoperate. Table 2.2 summarizes defined modulation schemes and data-rates for each layer type.

- PHY I: this layer type is intended for outdoor use with low data rate applications. It uses both On-Off Keying (OOK) and Variable Pulse Position Modulation (VPPM).
- PHY II: this layer type is intended for indoor usage with moderate data rate applications. This mode uses both OOK and VPPM modulations.
- PHY III: this layer type is intended for applications using Colour Shift Keying (CSK) that have multiple light sources and detectors with data rates in the tens of Mb/s.

Spectrally speaking, PHY I occupies a different spectral regions than PHY II and PHY III the modulation-domain spectrum (Figure 2.6), which permits PHY I-PHY II and PHY I-PHY III coexistence if a Frequency Division Multiplexing (FDM) mechanism is used. However, optical clock frequencies used for PHY II and PHY III overlap, causing significant overlap in the frequency domain spectrum. Due to the fact that PHY II devices may not all support multiple optical frequency

Table 2.2: PHY Layer Types Summary

Layer	Modulation	RLL Code	Optical Clock Rate	Data Rate
PHY I	OOK	Manchester	200 kHz	11.67 - 100 kb/s
	VPPM	4B6B	400 kHz	35.56 - 266.6 kb/s
PHY II	VPPM	4B6B	3.75 - 7.5 MHz	1.25 - 5 MB/s
	OOK	8B10B	15 - 120 MHz	6 - 96 Mb/s
PHY III	4 to 8-CSK	-	12 MHz	12 - 18 Mb/s
	4 to 16-CSK	-	24 MHz	24 - 96 Mb/s

bands required for PHY III, there is need to include a PHY II device on all PHY III devices to support PHY II-PHY III coexistence [21].

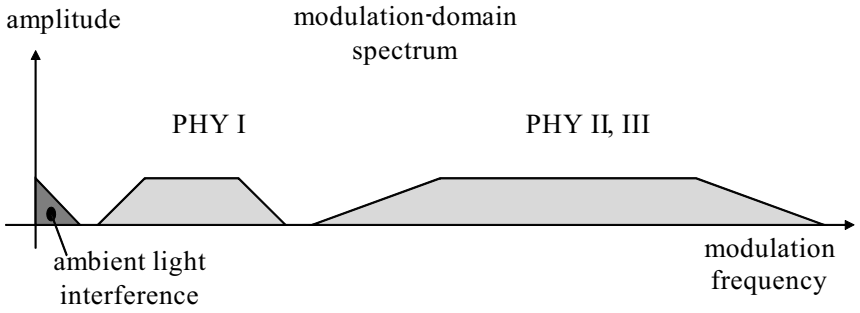

Figure 2.6: FDM separation of the PHY types in the modulation domain (from [21]).

2.2.3 Dimming and VLC Coexistence

Dimming capabilities poses a great challenge in VLC link. During idle of Rx periods, flicker-free visibility has to be maintained and adjoining both communication and illumination while still permitting light dimming is a crucial aspect in VLC. *Flicker* refers to light brightness fluctuations, which can have negative physiological impact on humans. Human eye response to light flickering is closely related to *Flicker Fusion Threshold*, and changes in brightness in VLC links must fall below the Maximum Flickering Time Period (MFTP) [20].

Flicker Fusion Threshold

The Flicker Fusion Threshold (Flicker Fusion Frequency or Flicker Fusion Rate) is a psychophysics vision phenomenon, which defines the frequency beyond a periodic light stimulus appears steady to a given observer [22]. The determination of this threshold is dependent on distinct parameters, such as the frequency and amplitude of the modulation, the average intensity, the wavelength bandwidth,

previous exposure to dark, and specific aspects to the observer, such as the position, age and fatigue of the viewer. It is mostly a statistical threshold rather than an absolute one. This phenomenon is of critical importance in any application that uses light, such as video or display applications, or illumination applications, such as luminaries and luminous billboards.

One of the challenges in not only in light communication, but in all illumination systems, is mitigating any flicker that could cause negative physiological changes in humans. More than causing epileptic responses on humans, there is evidence that flicker may cause eyestrain and headaches [23, 24]. Although there is no general consensus in literature, a frequency greater than 200Hz (MFTP < 5ms) is generally considered to be safe for observers [23, 24].

Light Perception in Humans

One other aspect that cannot be despised is how the Human Eye perceives and responds to various light levels. In fact, on how all human senses respond to various stimulus - vision, audition, gustation, olfaction and tactition. The Weber-Fechner law describes that the relationship a stimulus and its perception is logarithmic, and is given by Equation (2.1) and depicted in Figure 2.7.

$$\text{Perceived light (\%)} = 100 \times \sqrt{\frac{\text{Measured light (\%)}}{100}} \tag{2.1}$$

For a light source that is dimmed down to 10%, the human eye perceives it as being dimmed down to only 32%. Thus, light sources need to be dimmed over a very large range, to provide linear luminous reduction perception to the human eye. While this is important in ordinary LED luminaires, it also poses a challenge in VLC links, where communication must be provided regardless of light dimming.

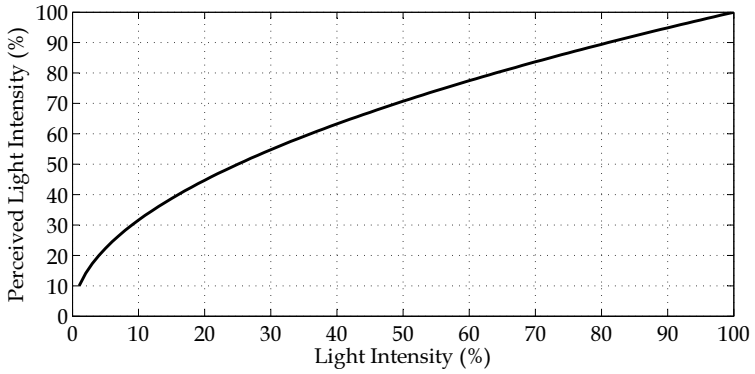

Figure 2.7: Human Light Perception according to Weber-Fechner's law.

The different modulation schemes used in the various PHY layer types have different trade-offs between data rates and dimming ranges. OOK provides variable dimming range and thus variable data rate by inserting compensation times, while VPPM provides variable dimming range while maintaining data rate constant by adjusting pulse width [20].

2.2.3.1 OOK Modulation and Dimming Method

OOK modulation is the simplest modulation scheme for VLC - LEDs are pulsed on and off depending on the data bit being 1 or 0. It uses Manchester Coding to ensure equal periods of positive and negative (null) pulses, providing a DC balanced code. Dimming when using OOK modulation is achieved by redefining the *on* and/or *off* levels or by adding "compensation" times in the data structure, since Manchester Coding has an inherent 50% duty-cycle. While first method provides constant-rate as light is dimmed, it may cause color shift due to the change in LED current, which is to be avoided. The latter method will imply reduced data rate albeit with constant range. An example of the OOK dimming structure is shown in Figure 2.8 [20, 21].

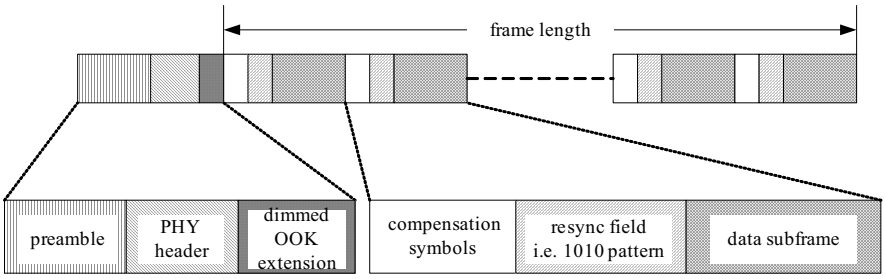

Figure 2.8: OOK dimming structure (from [21]).

2.2.3.2 VPPM Modulation and Dimming Method

VPPM Modulation improves on Pulse Position Modulation (PPM) by changing the duty-cycle of each encoded symbol, whose distinction is done by their pulse position. By changing each symbol's duty-cycle, light dimming is achieved without any color-shift risk, as per Figure 2.9. VPPM is inherently flicker-free due to the fact that average brightness is equal on both 0 and 1 bits. Light intensity for preamble and header can be adjusted by inserting compensation symbols. 4B6B RLL coding is used with VPPM, which allows for a DC balanced code [20, 21].

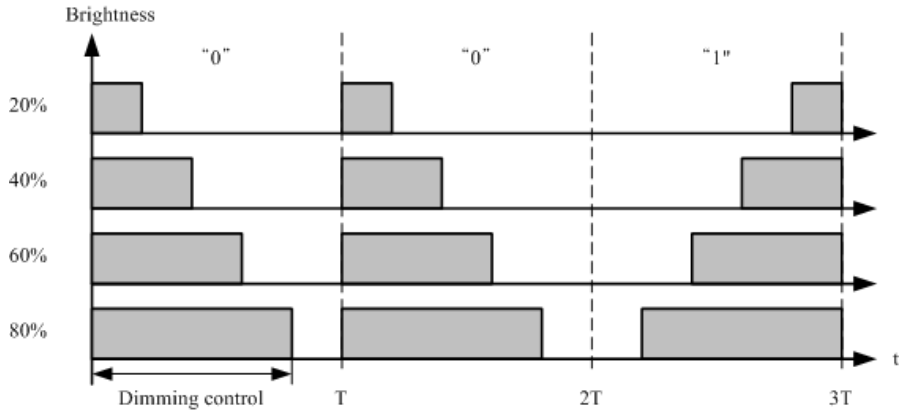

Figure 2.9: Schematic mechanism for VPPM dimming (from [21]).

2.2.3.3 CSK Modulation and Dimming Method

CSK Modulation employs amplitude dimming and controls the brightness by changing the current that drives the LEDs. Therefore, a colour shift of the light source may arise [20, 21].

2.2.3.4 VLC extended to OFDM

In addition to the Single-Carrier Modulation (SCM) techniques described above, Multiple-Subcarrier Modulation (MSM) has been proposed in [25] by use of Orthogonal Frequency Division Multiplexing (OFDM). Using OFDM avoids inter-symbol interference that arrives with increase of transmission rates, when using SCM. However, conventional OFDM signals (bipolar and complex-valued) are not compatible with IM/DD systems (which, in their turn use real and unipolar values) - therefore, OFDM need to be transformed. Tsonev et al [25] propose four OFDM modulation techniques, compatible with IM/DD, including direct-current-biased optical OFDM (DCO-OFDM), asymmetrically clipped optical OFDM (ACO-OFDM), pulse-amplitude-modulated discrete multitone modulation (PAM-DMT) and unipolar orthogonal frequency division multiplexing (U-OFDM). Reported highest data-rates for VLC are 500Mb/s and 3.4Gb/s using OFDM modulation with single white LEDs and RGB LEDs respectively, [26, 27]. Also, extra modulation dimming techniques for VLC have been proposed [28].

CHAPTER 3

THE LIGHT EMITTING DIODE AND CIRCUIT DRIVERS

The 20th Century watched the rise and decline of *thermionic* electronic devices, which were surpassed by solid-state electronics. A similar process is occurring with optoelectronics. In fact, the *incandescent bulb* was once the lighting standard but it has been slowly replaced by the more efficient halogen and fluorescent bulbs, and more recently by the solid-state equivalent: the LED, the cornerstone of SSL. The first visible spectrum red LED was developed by Nick Holonyak Jr. in 1962, and it made its industry debut in 1968, by Monsanto Company. It has seen great development in the last 25 years, with the advances in blue emission LED manufacturing and it allowed for the creation of white light, and consequent proliferation in both illumination and display technologies, [12, 29].

3.1 The Light Emitting Diode

A p-n junction is formed between two adjacent, distinctly semiconductor doped regions (p-type and n-type). The concentration gradient caused by the excess of electron in the n-type region, causes electrons to re-arrange themselves and diffuse from the n-type region to the p-type region. This diffusion carrier movement generates an electric field E, and an equilibrium is reached when it equals the concentration gradient. The region over which the electric field extends is called *depletion region*, and the built in voltage V_{diff} is the integration of electric field E over the depletion region, as seen in Figure 3.1, [30]. Equating the integral of

the electric field to the difference between Fermi levels on the depletion region boundaries (X_n and X_p), the built in voltage (diffusion voltage) V_{diff} is computed by Equation (3.1) [30, 31].

$$V_{diff} = \int_{X_p}^{X_n} E(x)dx = (E_{Fn} - E_{Fp})\frac{1}{e} = \frac{k_B T}{e} ln\left(\frac{N_A N_D}{ni^2}\right), \tag{3.1}$$

where N_A and N_D are the carrier concentration for acceptors and donors, respectively, k_B is the Boltzmann constant, T is the room temperature, and ni^2 is the number of electrons excited from the valence to the conduction band. For $N_A = 1 \times 10^{16} \cdot cm^{-3}$ and $N_D = 2 \times 10^{16} \cdot cm^{-3}$, diffusion voltage results in $V_{diff} = 711$ mV.

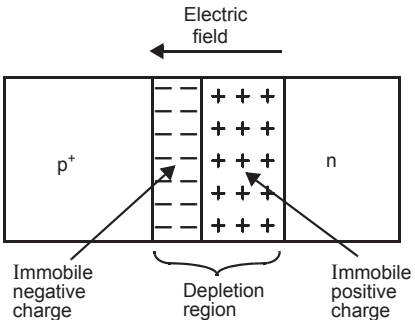

Figure 3.1: Simplified model of a p-n juction (from [31]).

Light emission from a p-n junction is an optical and electrical phenomenon called *Electroluminescence*, which describes the emission of light by a material when subject to an electrical current or electric field. *Electroluminescence* is fundamentally different from *Incandescence*, as it can occur at room temperature. *Incandescence* describes the emission of electromagnetic radiation by a material which is heated to high enough temperature, [29].

When an LED is forward-biased the imposed electric field causes electrons on the *n side* to move towards the *p side*, and fill the existent holes therein. The electron *jump* between the two distinctly doped materials occurs in the junction between the two - depletion region. As the electrons jump from the *n-type* region to the *p-side* region and adjoin with holes, they fall into a lower energy level (from conduction band E_C to the valence band E_V) and most excess energy is emitted in form of a photon - thus, light emission (as per Figure 3.2b). This energy *bandgap* eV defines the emission wavelength. The higher it is, the higher the photon energy, and thus the lower the wavelength λ. The relationship between a photon's energy and its wavelength can be extracted from Planck's Quantum Hypothesis [32], by Equation (3.2))

$$E = h\nu = h\frac{c}{\lambda}. \tag{3.2}$$

A photon's energy is inversely proportional to its wavelength.

Thus, photons from a blue light source (∼475 nm) are in higher energy levels than those from a red light source (∼650 nm). In reality, LED's emission is confined to a narrow band rather than a wavelength (*quasi-monochromatic* emission).

Figure 3.2 shows the bandgap differences between an LED in both off and on states (no bias and forward bias, respectively). When forward-biased, the holes and electrons on both *p* and *n* sides respectively are pushed toward the junction, thus reducing the depletion region width. As forward-bias voltage increases, this region becomes thin enough that the existent built in electric field can no longer counteract carrier motion, thus reducing electrical resistance. Additionally, Figure 3.2b illustrates the *Electroluminescence* phenomenon, [12].

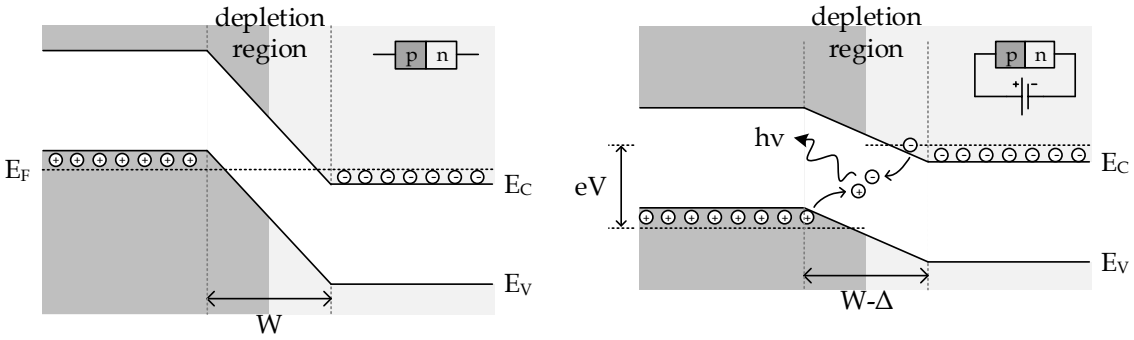

(a) No Bias (b) Forward Bias

Figure 3.2: LED's bandgap energy levels (adapted from [33]).

3.2 LED Drivers

The most efficient way to drive an LED string is by means of an LED Driver - essentially a SMPS, optimized for LED use, [34]. These are the power supply for an LED System, much like a ballast is to a fluorescent lighting system. They allow the use of LEDs in a constant I/V bias point, which in turn allows for constant thermal dissipation as well as constant luminous intensity. LED Drivers can operate either in a constant voltage or a constant current mode. They can easily enable the dimming of a given LED string via Pulse Width Modulation (PWM), by modulating the delivered current. By altering the *duty-cycle* of the signal that drives the LED string - that is, by altering the pulse's *width*, as $D = t_{ON}/t_{SW}$ - LEDs are always operated at the same I/V bias point, resulting in no colour shift. Figure 3.3 shows a typical PWM waveform.

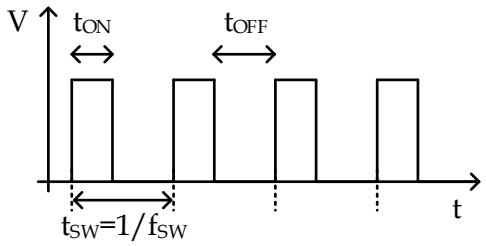

Figure 3.3: Typical PWM Signal.

3.2.1 Buck vs. Boost

Buck or Boost topologies are amongst the most popular SMPS topologies used in LED based circuits for SSL. A Buck Driver regulates a higher source voltage into a lower output voltage level - $V_o < V_s$. Contrarily, a Boost driver regulates a lower source voltage into a higher (hence, *boosted*) output voltage - $V_o > V_s$.

Synchronous Buck and Boost Topologies are shown in Figure 3.4, respectively. These include a PWM generator, switching transistors, output LC filter and load.

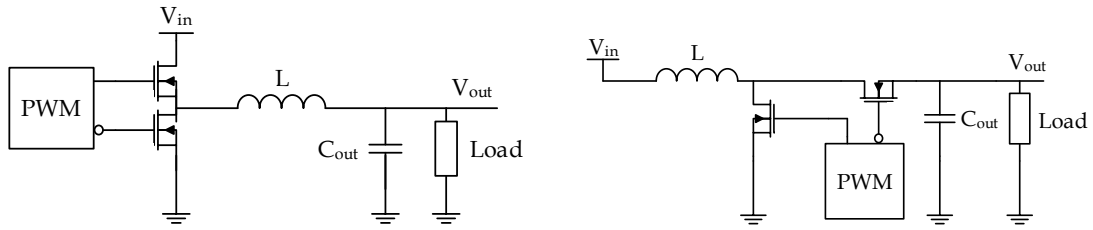

(a) Buck Driver

(b) Boost Driver

Figure 3.4: Simplified schematics of buck and boost topologies.

$$I_L = \frac{1}{L}\int V_L \Leftrightarrow \frac{dI}{dt} = \frac{V_L}{L} \tag{3.3}$$

Equation (3.3) exposes the voltage and current in the inductor L, whilst Table 3.1 breaks down the inductor current expressions for both Buck and Boost topologies (respectively), on both switching states [35, 36]. Rearranging these, considering steady-state operation where stored energy in inductor is constant over switching cycles [1], it can be demonstrated that the relationship between V_{in} and V_{out} is solely dependent on duty-cycle D, and not on switching frequency f_{sw}.

[1] $\frac{dI}{dt}t_{ON} + \frac{dI}{dt}t_{OFF} = 0$

Table 3.1: Inductor Current expressions during both operation states and duty-cycle D values for Buck and Boost topologies

	Buck	Boost
during t_{ON}	$\frac{dI}{dt} = \frac{V_{in} - V_{out}}{L}$	$\frac{dI}{dt} = \frac{V_{in}}{L}$
during t_{OFF}	$\frac{dI}{dt} = \frac{-V_{out}}{L}$	$\frac{dI}{dt} = \frac{V_{in} - V_{out}}{L}$
duty-cycle D	$\frac{V_{out}}{V_{in}}$	$1 - \frac{V_{in}}{V_{out}}$

This allows the switching regulators to operate at fixed switching frequencies which is desirable for EMI limit regulations [37]. LED Drivers have historically shifted from Constant-Voltage to Constant-Current power sources. [38]. Although the ultimate goal is to regulate both current and voltage, LEDs are in fact current devices, given their luminous output and current linearity as Figure 3.5a demonstrates. Additionally, Figure 3.5b supports the idea of a constant-voltage output, as small voltage variations result in large current fluctuations, and thus in large illuminance alterations.

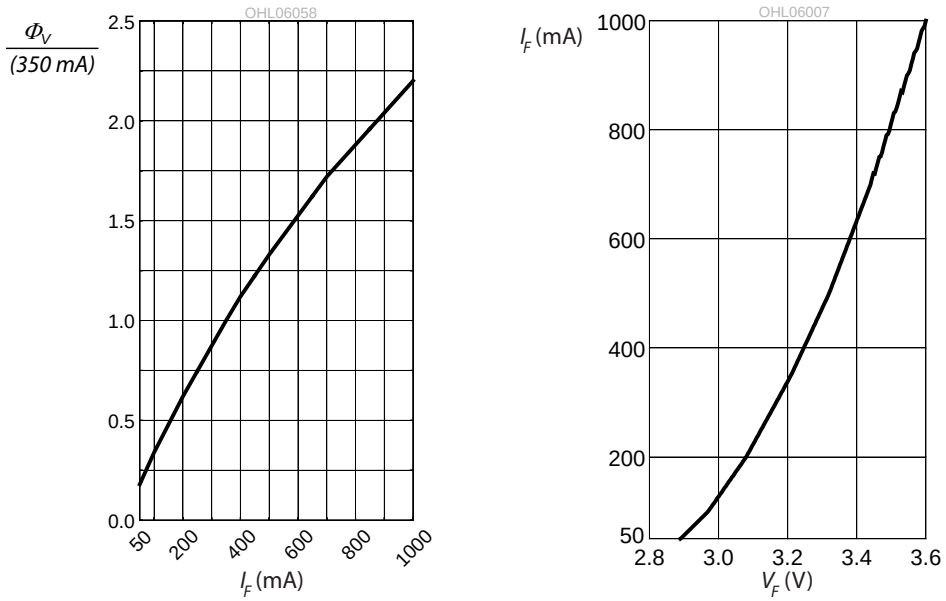

(a) $I_F / \frac{\Phi_v}{\Phi_{v(350mA)}}$ curve

(b) I_F / V_F curve

Figure 3.5: OSRAM LUW-W5AM Optical and Electrical characteristic curves (from [14]).

3.2.2 Feedback Loop

A very important aspect in any SMPS LED Driver design is feedback regulation. By designing the regulator with a negative feedback loop, it will allow for proper voltage and/or current control, guaranteeing good response to load variations and proper line disturbance rejection.

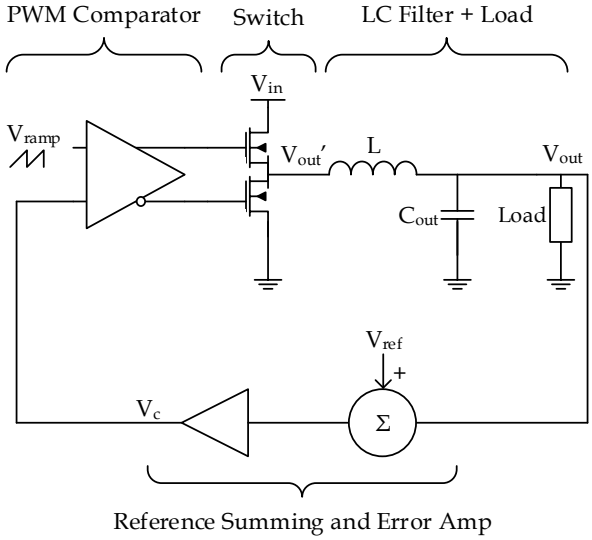

Figure 3.6: Buck Regulator with Voltage-Mode Control.

Figure 3.6 shows a Buck switching regulator with Voltage-Mode Control (VMC). In the core of this control loop is the *PWM Comparator*, which produces a pulse-train that drives the switching transistors. This pulse train is obtained by comparing a control voltage to a fixed voltage sawtooth signal. Since the control voltage is proportional to the output voltage, so is the pulse-train that drives the transistors. A voltage drop on the output will cause a lower control voltage, which will consequently generate a pulse signal with increased duty cycle - thus causing the output voltage to rise, and compensate the previous drop. Historically, this was the first control feedback method to appear for the switching regulators which gathered increasing interest in the mid-1970s, [37]. Another control method, denominated Current-Mode Control (CMC) built upon the VMC loop. One of the problems of VMC technique lies in the fact that it is permeable to power line disturbances. The PWM comparator does not detect a sudden change in V_{in} directly and consequently any changes to the control loop will occur with a certain lag, after some switching cycles, when the output error causes a shift in control voltage. Inherently, there is some *ringing* associated with this control method, as duty-cycle is repeatedly altered around a settling value.

Contrarily, the CMC loop has inherently good line rejection, which was one of the reasons for its popularity. The CMC employs a fast current control loop along with the slower voltage control loop. What this does is that it allows for the inductor current to be continuously sensed, which consequently permits instantaneous action on the output current, should it exceed a defined value, [35, 37, 39, 40, 41].

A good stability criterion applied to switching regulators is a phase-margin of at least 45º, up to a maximum of 75º. [42, 43, 44]. A more detailed analysis of both control methods for a Buck converter and compensator networks are present in the following sections.

3.2.2.1 Voltage-Mode Control

By analysing Figure 3.6, one can identify basic system blocks - the PWM Comparator, the Switch and the LC Filter form the Buck Regulator's installation - G(s) -, whereas the voltage divider, reference and error blocks form the feedback loop H(s). The G(s) is formed by two essential blocks - the PWM Comparator/Switch and the LC filter. The duty-cycle (D) of the pulsed signal that drives the switch equals the ratio of the control voltage V_c with the fixed amplitude of the sawtooth wave V_{ramp} - Figure 3.7 shows this. The PWM Comparator and Switch blocks' gain can be easily derived - it is the ratio of the change of $V_{out}{}'$ with respect to the change of V_c, as described in Equation (3.4), [35, 37, 41, 45].

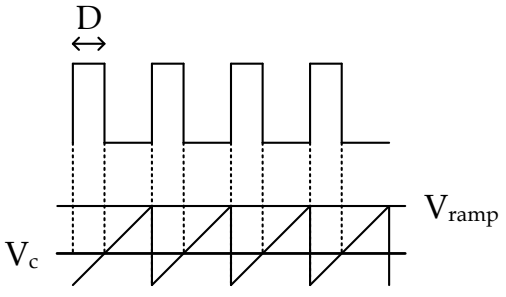

$$D = \frac{V_c}{V_{ramp}}$$
$$V_{out} = D \times V_{in} \tag{3.4}$$
$$Gain_{DC} = \frac{\delta V_{out}}{\delta V_c} = \frac{V_{in}}{V_{ramp}}$$

Figure 3.7: PWM Comparator.

The LC filter's frequency response is depicted in Equation (3.5) and the resulting G(s) transfer function is shown in Equation (3.6) and depicted in Figure 3.8, for $L = 100\ \mu H$, $C = 100\ \mu F$ and $R_{ESR} = 100\ m\Omega$.

$$F(s) = \frac{sCR_{ESR} + 1}{s^2LC + SCR_{ESR} + 1} \tag{3.5}$$

$$G(s) = Gain_{DC} \cdot F(s) = \frac{V_{in}}{V_{ramp}} \cdot \frac{sCR_{ESR} + 1}{s^2LC + SCR_{ESR} + 1} \tag{3.6}$$

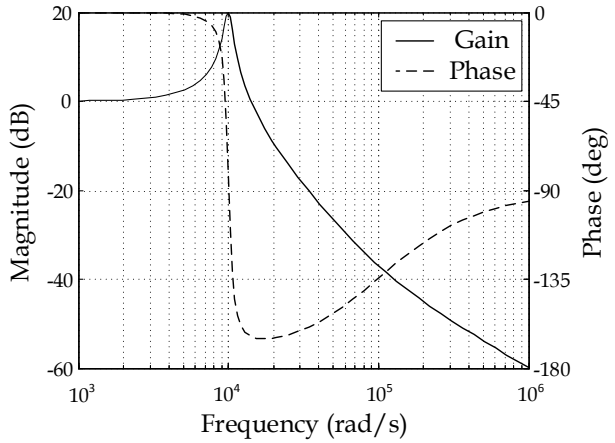

$$\omega_z = \frac{1}{R_{ESR}C}$$
$$\omega_{p_1} = \omega_{p_2} = \frac{1}{\sqrt{LC}} \tag{3.7}$$

Figure 3.8: VMC G(s) Bode Plot.

From the G(s) bode plot in Figure 3.8, it is possible to detect a LC double-pole ($\omega_{p_{1,2}}$ of Equation (3.7)), which causes severe gain peaking, as well as a sudden 180^o phase shift that can lead to instability. Additionally, a zero is produced by the capacitor's Equivalent Series Resistance (ESR), although it is easily compensated (ω_z of Equation (3.7)). A capacitor with low ESR value ensures this zero is shifted to a high enough frequency that it becomes irrelevant. The DC Gain varies with input voltage, as stated before, and thus loop response changes with V_{in}, causing the crossover frequency to equally shift, [37].

3.2.2.2 Current-Mode Control

In CMC, output current is sensed and its peak or average value is compared to a reference current level, which produces an error voltage that, in turn feeds into the PWM comparator. Effectively, a voltage-controlled current source has been created - a control voltage V_{c2} controls the switch current, and therefore the inductor current I_L (that, by being in series with the inductor produces no phase shift). What this does is that the system effectively becomes a first-order system, as opposed to VMC, because the inductor drops out of the equation, [46, 47, 48]. This will prove to be very useful, as seen below. From Figure 3.9, one can derive the G(s) and H(s) blocks. The PWM Comparator, Switch and ideal current source

(ie, the inductor), as well as parallel RC network form the G(s) installation, while the error amplifier and comparators form the H(s) feedback loop. Note the extra feedback loop, inexistent in VMC.

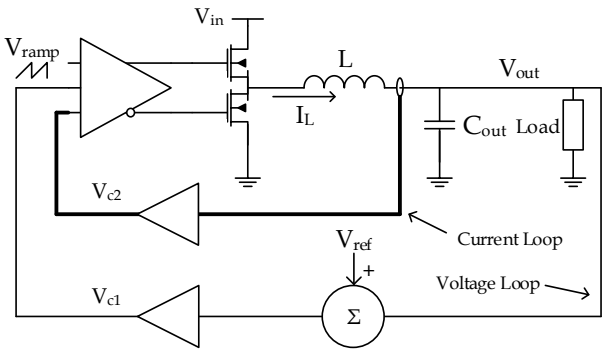

Figure 3.9: Buck Regulator with Current-Mode Control.

The G(s) transfer function is unequivocal once the voltage-controlled current source extrapolation is accomplished - one may decompose G(s) into two main blocks - the voltage-controlled current source, which has an inherent transconductance value (g_m) and the parallel output capacitor and load - these are depicted in Figure 3.10 and Equations (3.8), [37, 49, 50].

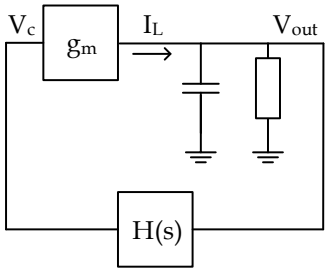

Figure 3.10: CMC's simplified block diagram.

$$\begin{aligned} \frac{V_o}{I_L} &= R_{LOAD} \cdot \frac{sCR_{ESR}+1}{sC(R_{ESR}+R_{LOAD})+1} \\ G(s) &= \frac{R_{LOAD}}{g_m} \cdot \frac{sCR_{ESR}+1}{sC(R_{ESR}+R_{LOAD})+1} \end{aligned} \tag{3.8}$$

The characteristic CMC G(s) Bode plot is shown in Figure 3.11, for $L = 100\ \mu H$, $C = 100\ \mu F$, $R_{ESR} = 100\ m\Omega$ and $R_{LOAD} = 1\ \Omega$. Contrarily to the VMC case, it is a first-order system. It features one single pole and one single zero. The zero is produced by the capacitor's ESR, and provided that it is low enough, it poses no inconvenience - this is the reason why, generally, CMC is exempt of phase compensation (although not exempt of any type of compensation). The single-pole is inversely proportional to the load's impedance and due to the fact that DC Gain is proportional to the load's impedance, crossover frequency f_c is unchanged, regardless of load. Additionally, due to the fact that DC Gain does not alter itself

respectively to input voltage V_{in}, CMC is quite impermeable to line disturbances, [37].

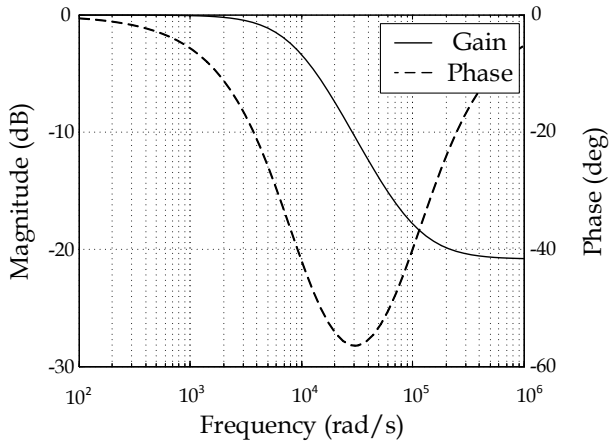

$$\omega_z = \frac{1}{R_{ESR}C} \qquad \omega_{p_1} = \frac{1}{(R_{LOAD} + R_{ESR})C} \tag{3.9}$$

Figure 3.11: CMC G(s) Bode Plot.

3.2.2.3 Compensation Networks

Compensation Networks must be used to ensure dynamic response while maintaining stability. They form the feedback loop H(s). Three main compensation types are normally used in VMC regulators. Type I uses an integrator - it has a single pole at the origin, thus providing a -1 gain slope and constant phase at 270º. Type II is a proportional and integrator amplifier, featuring two poles (one at the origin) and a zero. It provides a 90º phase boost between the zero and pole spread. Finally, Type III compensator circuits allow for a more prominent phase boost, by employing two double-zeros and double-poles, [42]. Figures A.1 to A.3 in Appendix A depict both circuitry and bode plots for each compensator.

For CMC switching regulators, there is little need, in general, for any kind of phase compensation, due to their first-order characteristics. However, a different kind of compensator must be considered for peak-current mode control regulators when using duty-cycles higher than 50%. Figure 3.12 depicts both stable I_L (solid line) and perturbed $I_L + \Delta$ (dashed line) inductor current waveforms over time. m_1 and m_2 correspond to the inductor slopes in the ON and OFF periods, as per Table 3.1. V_e is the peak current reference. In the ON period, inductor current increases with slope m_1 and as it intersects the V_e reference, switching stops and inductor decays with slope m_2. This is repeated over the following switching cycles (which are marked by t_{SW1}, t_{SW2}, etc). For a small ΔI_0 perturbation on the first switching instant, it is perceivable that this perturbation is multiplied concurrently with subsequent switching instants (ΔI_1 on t_{SW1} and ΔI_2 on t_{SW2}) for D>0.5 [46, 51, 52].

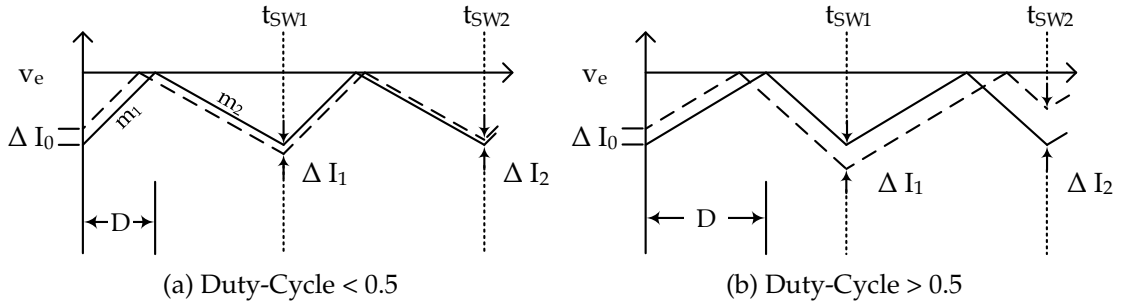

(a) Duty-Cycle < 0.5 (b) Duty-Cycle > 0.5

Figure 3.12: Inductor Current Perturbations in CMC for duty-cycle D lower and higher than 0.5 (adapted from [51]).

The perturbation causes a series of changes in inductor current in the form of a geometric progression whose common ratio is given by Equation (3.10):

$$r_p = \frac{\Delta I_n}{\Delta I_{n-1}} = \left(\frac{D}{D-1}\right)^n. \tag{3.10}$$

Figure 3.14 illustrates how this term diverges as switching periods $n \to \infty$ for $D > 0.5$. The use of duty factors higher than 50% will lead to a ringing response of the inductor current at half the switching frequency ($0.5 f_{sw}$)- this is commonly described as Subharmonic Ringing or Subharmonic Instability. In turn, this ringing response can lead the voltage feedback to break into $0.5 f_{sw}$ oscillation, due to its slower response, further aggravating the system's overall stability and response. To overcome this, an additional slope compensator must be added to CMC's feedback loop, as per Figure 3.13. This *reverse slope* adds to the control signal, and allows the transistors to turn off *earlier*, in cases of D>0.5, [46, 51].

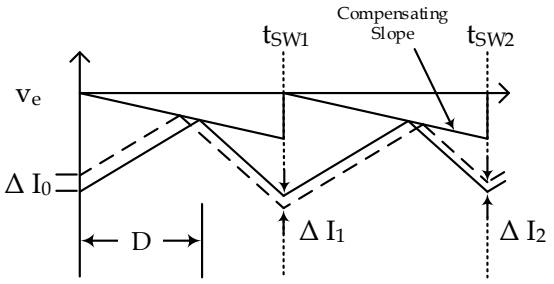

Figure 3.13: Addition of Slope Compensation to the Control Signal (from [51]).

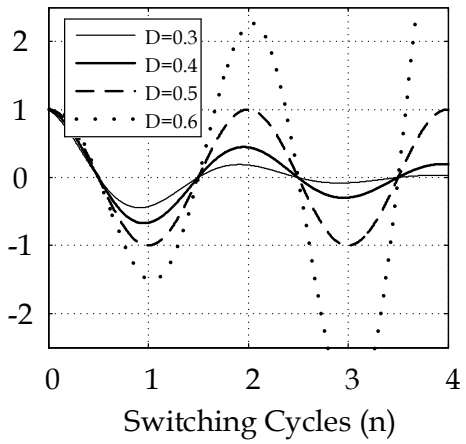

Figure 3.14: Evolution of Inductor Current Perturbation as $n \to \infty$.

3.2.3 PWM Dimming

Three different PWM dimming schemes can be identified in the literature. *Enable dimming* is commonly used in simpler SMPS circuits, which feature an Enable/Shutdown pin. By applying a PWM signal, the entire converter is switched on and off, thus turning its load on and off. However, this scheme is inherently slow, as the converter's delay and rise times compromise dimming frequency and promote significant LED colour shift, [53, 54]. On the other hand, *Series Dimming* is achieved by switching a transistor in series with the load. Output voltage remains constant due to the stored energy in the output capacitor. This switching scheme allows for the current load to be turned off immediately - however, depending on the the control feedback method, this extreme unloading may drive the error amplifier in the feedback loop into oscillation, given that the feedback loop is indeed disconnected. [53, 54] Finally, *Parallel (or Shunt) Dimming* [55] is achieved by switching a transistor in parallel with the load, *shunting* it. Output capacitor is minimized and load current equals inductor current. In fact, the use of this method turns an LED Driver into a current source. Ideally, its output impedance would be infinite, allowing for a very fast output voltage slew. Using a large inductance value results in low current ripple and thus low load ripple. This scheme permits the highest PWM frequencies, given that the converter is kept working, and therefore turn-on and delay times are non-existent. On the other hand, this method is less efficient, as inductor current is shunt to ground when the load is turned off. This method requires a very fast control loops, and hysteretic controllers are often better suited, [53, 54, 55, 56]. Figure 3.15 depicts all three methods.

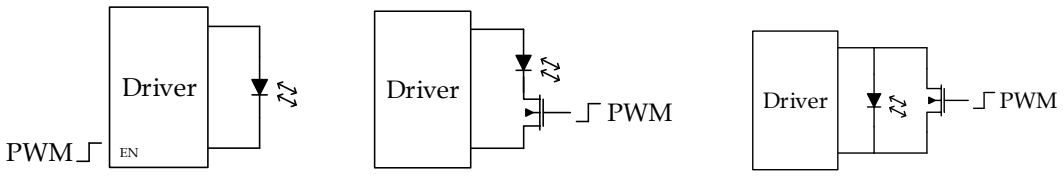

(a) Enable Dimming (b) Series Dimming (c) Parallel Dimming

Figure 3.15: Various Dimming Methods.

3.3 Constraints from LEDs and LED Drivers in VLC applications

The prime difference between an ordinary LED and a VLC-capable LED luminaire resides in the frequency at which the LEDs are modulated. LEDs bandwidth extend to hundreds of MHz, as typical rise times fall in the range of 1 to 50 ns [57]. Reported bandwidth of LEDs is 20 MHz in [6], although the phosphor coating on White LEDs limits it significantly. If VLC using White LEDs is intended, a blue filter can be used on the receiver's side, isolating the blue light component, which does not suffer from phosphor lag. Alternatively, RGB LEDs are good contenders for VLC applications - white light can still be achieved by colour mixing, and each of the LEDs represents a 20 MHz bandwidth channel, due to the lack of phosphor coating [6].

The concept of LED modulation frequency, regarding LED Drivers can correlate with internal switching frequency, although these are normally transversely different variables. The internal switching frequency sets the operating frequency for all internal circuitry, and it is the frequency at which the inductor is charged and discharged. LED modulation frequency, on the other hand, describes the frequency at which LEDs are turned on and off. On an ordinary LED driver, an external PWM signal drives the LED string and changing its duty-cycle alters the perceivable light output - hence, dimming. In fact, this PWM dimming frequency can be thought of as a load transient - the LED string is switched in and out, corresponding to a transient from zero to full load. Whereas in normal applications PWM frequencies are under 10 kHz, they can reach 50 times higher values for VLC. Recalling Table 2.2 in Chapter 2, optical clock rates for VLC can reach the 120 MHz, but an optical clock rate of 500 kHz should guarantee correct operation for lower data-rate layers (PHY I). While it is desirable that switching regulators respond quickly to load and line perturbations, higher load perturbations such as high-frequency dimming for VLC must be transparent to the switching regulator. In fact, a typical loop bandwidth is 10-30% of the internal switching frequency, which is very low compared to the high-frequency PWM dimming necessary for VLC. This means that any high-frequency voltage perturbations caused by high-frequency PWM dimming are ignored by the control loop. Contrarily to [6], and supporting Modepalli et al [56], the author suggests that high-frequency load disturbances (via series or parallel dimming) should be rejected by the control loop.

Although boost regulators are finding increasing use due to low-voltage, portable devices, or even due to the sheer increase in the number of LEDs for certain applications, buck regulators are often preferred due to their versatility and ease of design. These normally offer a myriad of control loop methods, whereas boost regulators are almost exclusively restricted to peak-current mode control. Besides, the boost converter has a discontinuous output current, and requires an output capacitor to keep output voltage, which by itself impedes the use of parallel dimming. On the other hand, regarding buck regulators, the inductor is always connected to the load. This gives buck converters an advantage over boost converters in both transient response and PWM dimming ratio, [54, 58].

CHAPTER 4

THE LED AS A LIGHT SENSOR

4.1 Light Sensors - Historic Background

The first electronic light sensors dates back to the 1940s with the *Phototube*, which was a light-sensitive vacuum tube, and the *Photomultiplier*, which used multiple electrodes - dynodes - at stepped potentials, to multiply the incoming electrons from the photocathode. The latter is still used today, mostly in scientific research. When it comes to solid-state components, the obvious choice relies on photodiodes and phototransistors, but the first mention of the use of LEDs as light sensors dates back to 1970's by Forrest W. Mims, [8, 9, 10]. Whilst working with photodiodes, Mims observed that certain photodiodes could emit near-infrared radiation, which could then be detected by similar photodiodes. Mims then explored this concept using LEDs, and by 1980 he demonstrated that LEDs could be used as two-way devices. Mims concluded that the spectral sensitivity of the LED was related to its emission spectrum, and more than demonstrating LEDs as light sensors, Mims demonstrated their use as *narrow band* light sensors, and employed them in Sun Photometer circuits [8, 9, 10]. While, theoretically, this concept is valid for all types of LEDs, phosphor coated LEDs - like the ones used to produce white light - do not make good light sensors, given, in fact, to said coating.

4.2 Principle of Operation

The principle of operation of an LED as a light sensor is very much the same as of a photodiode, and is based on the *Photoelectric effect*.

As photons reach a p-n junction, they generate free electron-hole pairs. Incident energy excites electrons to the conduction band, and due to the existing intrinsic electric field, these free pairs are swept by drift. Thus, electrons move towards the n-side (cathode), and holes move towards the p-side (anode). A current is created, and it is proportional to the incident light, or radiation power. To enhance this created current, an external reverse bias voltage can be applied. This adds to the existing voltage caused by the intrinsic electric field, and results in a wider depletion region, [30, 57, 59]. Since the depletion region is widened, so is the electric field therein, and thus the probability of the generated free carriers being transported increases. Figure 4.1 shows the energy bandgap diagram of a reverse-biased p-n junction, as well as electron excitation and carrier transport.

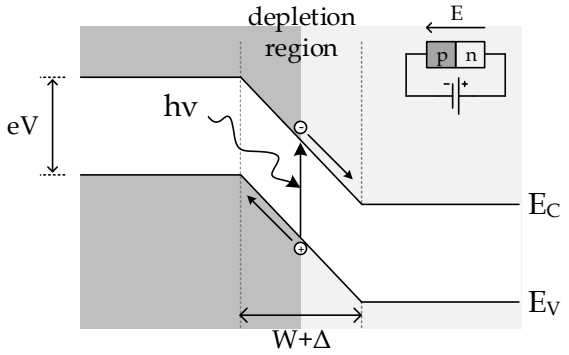

Figure 4.1: Photoelectric effect on a reverse-biased p-n junction.

Different reverse bias voltages result in different depletion region widths, which in turn result in different junction capacitances. Equations 4.1 and 4.2 describe the relationship between reverse bias V_{bias}, junction capacitance C_j and depletion region width W_d:

$$W_d = \sqrt{\frac{2\,\epsilon_{Si}\,\epsilon_0}{e}\left(V_{bias} + V_{diff}\right)\left(\frac{1}{N_A} + \frac{1}{N_D}\right)}\ , \tag{4.1}$$

$$C_j = \frac{\epsilon_{Si}\,\epsilon_0\,A}{W_d} \Leftrightarrow C_j = \frac{\epsilon_{Si}\,\epsilon_0\,A}{\sqrt{\frac{2\,\epsilon_{Si}\,\epsilon_0}{e}\left(V_{bias} + V_{diff}\right)\left(\frac{1}{N_A} + \frac{1}{N_D}\right)}}\ , \tag{4.2}$$

where $\epsilon_0 = 8.854 \times 10^{-14}$ F/cm is the permittivity of free space, ϵ_{Si} is the silicon dielectric constant, e is the elementary charge, N_A and N_D are carrier concentrations for acceptors and donors and V_{diff} is the inbuilt voltage. Figures 4.2 and 4.3 depict the equations - they show the relationship between reverse voltage V_{bias} and depletion region width W_d and between reverse bias V_{bias} and junction

capacitance C_j respectively, for $\epsilon_0 = 8.854 \times 10^{-14}$ F/cm, $N_A = 1 \times 10^{16} \cdot cm^{-3}$ and $N_D = 2 \times 10^{16} \cdot cm^{-3}$ and $e = 1.602 \times 10^{-19}$, [59]. It is safe to assume that applying a reverse bias voltage will increase the system speed. By applying a reverse voltage, the depletion region is widened which leads to a decrease in junction capacitance. Figure 4.3 shows the relationship between depletion region width and V_{bias} - the reverse bias voltage. As V_{bias} increases, so does the depletion width. Besides depending on technology values, such as the silicon dielectric constant ϵ_{Si} and silicon resistivity ρ, it also depends on LED/photodiode specifications, such as the Active Area A [12, 29]

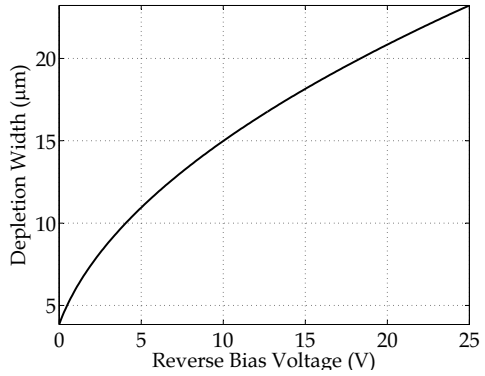

Figure 4.2: Depletion Width vs Reverse Voltage.

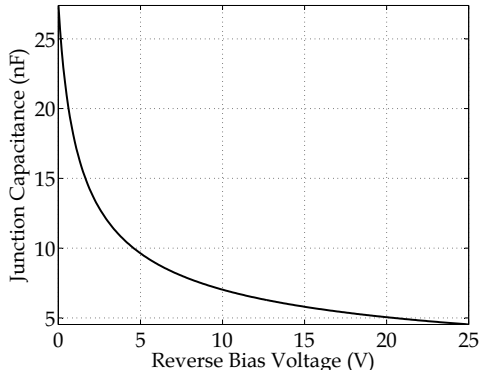

Figure 4.3: Typical Capacitance vs Reverse Voltage.

Figure 4.4 shows the equivalent circuit for a reverse-biased photodiode and a forward-biased diode. Depending on how the diode is biased, different capacitances are associated to the diode's equivalent circuit. While the junction capacitance C_j is dominant in reverse-biased junctions, the diffusion capacitance C_d is most prominent in forward-biased diodes.

Junction Capacitance occurs due to the widening of the depletion region - holes and electrons from both p and n sides are pulled away from the junction, as it is reverse-biased. The junction resembles, in fact, a parallel plate capacitor.

On the other hand, Diffusion Capacitance relates with charge changes, dependent of the applied voltage. When forward-biased, the minority carrier distribution outside the depletion region increases dramatically, as they are injected into the quasi-neutral regions ($\Rightarrow \Delta n_p > 0, \Delta p_n > 0$). In order to preserve quasi-neutrality, majority carrier density increases by the same amount. Minority carriers diffuse in the quasi-neutral regions, recombining with majority carriers - this leads to an additional capacitance called Diffusion Capacitance. This capacitance is calculated by computing the change in charge with voltage, i.e $C = \frac{\Delta Q}{\Delta V}$, [60, 61].

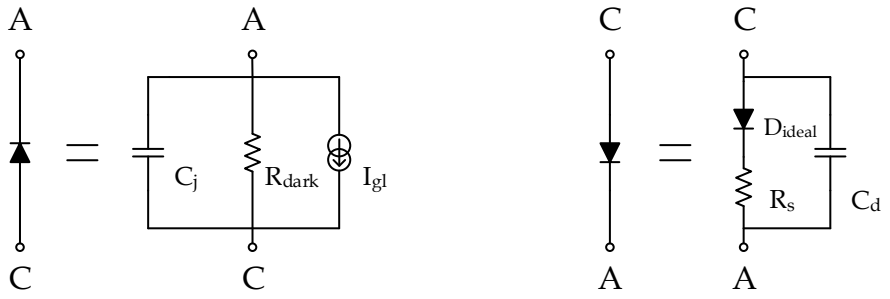

(a) Reserve-biased photodiode equivalent circuit

(b) Forward-biased diode equivalent circuit

Figure 4.4: Diode equivalent circuits.

4.3 Physical Constraints

4.3.1 Package colour

When referring to operating an LED as a sensor, it is important not to understate its package. Some coloured LEDs are packaged in a tinted package, of the same colour as their emitting wavelength. This has implications in the use of the LED as a bi-directional port. As an emitter, the coloured tinted package is desirable - it focuses the emission spectrum and broadens the emission angle for better visibility, even if the illuminance is somewhat reduced. A red epoxy case on a red LED means that it will reflect light one perceives as red (wavelength from 620 to 740 nm). As a sensor it is not desirable, exactly for the same reason - any red light shone into it will be reflected, and not absorbed. Photons are therefore impeded from reaching the p-n junction, or at least not as easily, were the lenses transparent. So theoretically, a red LED in a diffused package should not detect red light.

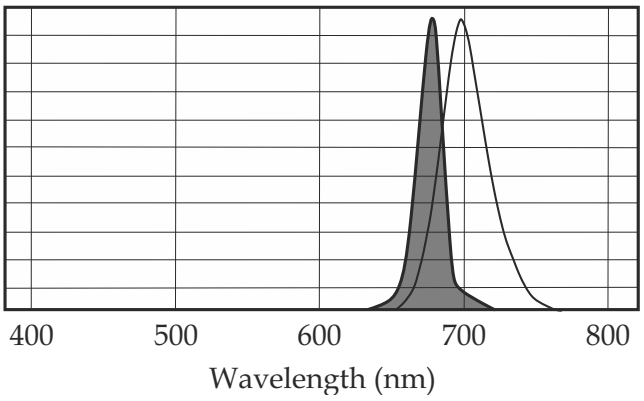

Figure 4.5: Red LED and package emission spectra.

One factor that should be taken into account is of course the superposition of

the chip's emission spectrum with the wavelength correspondent to the package's colour. Figure 4.5 illustrates this. The grey area represents the colour hue of the tinted lens, whereas the white area represents the emission spectrum of a red LED. From the standpoint of a reception device, all light shone into the device that falls into the grey area is reflected (and therefore does not reach the LED chip), whereas other colours such as dark red and orange may, because they are not reflected by the coloured package. It should be noted that light sensing is not limited to allowing said radiation to reach the LED chip. In other words, taking the above example, it should not be granted that a red LED with those characteristics should detect dark red and orange. Emission and Sensitivity Spectra are different concepts altogether. The idea that should be retained is that any coloured lens will affect the light sensitivity of an LED. The same happens with white LEDs, which contain a phosphor coating, that affects photon reach to the p-n junction. The LED package's type and colour assumes the same importance as the light input window shape and size of a photodiode, when using the LED as a light sensor.

4.3.2 LED Chip Area

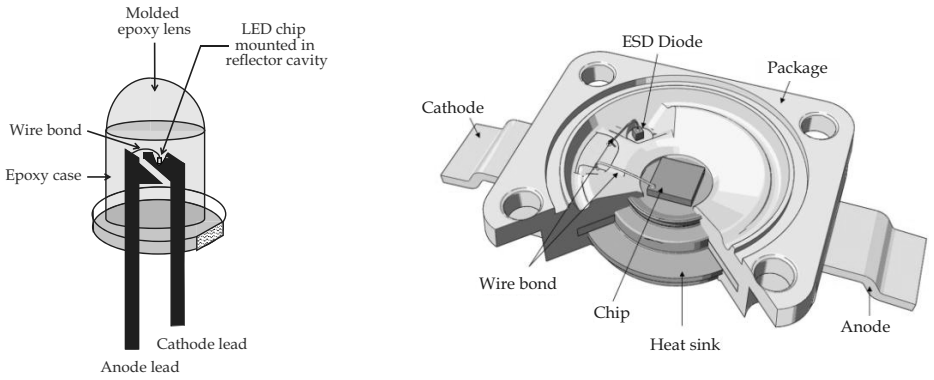

(a) Through-hole (b) SMD

Figure 4.6: Different LED Construction types (adapted from [12, 62]).

The photosensitive area is a key property for a photodiode. LEDs, though not specifically built to be responsive to light, also abide to the same rules - the larger the photosensitive area, the higher the generated photocurrent. More photons will reach the photosensitive area, and larger beams can be utilized. Due to LEDs typical morphologies, which are not designed to be used as light sensors, it is important to choose LEDs that have an as flat and as exposed junction as possible. In fact, it is safe to say that the most common 3 mm and 5 mm through-hole LEDs do not serve as good light sensors - one of the reasons for that is indeed their

construction and their chip area. Through hole LEDs have chip areas of around 0.1 mm^2, which can be underwhelming when compared to typical photodiodes. On the other hand, with the proliferation of LED displays and luminaries, flatter LEDs like the majority of Surface-mounted device (SMD) LEDs available today, feature much larger chip areas, ten times larger (1 mm^2) than those in through-hole LEDs. On the other hand, the larger the chip area (analogue for photosensitive area in photodiodes), the higher the junctions capacitance C_j. Therefore larger LEDs, while more sensitive, may prove to be slower. Figure 4.6 depicts both 5 mm and SMD LED constructions.

4.3.3 ESD Device

Construction-wise through-hole and SMD LEDs differ in many aspects, but a crucial one is the presence of an ESD protecting device in SMD LEDs, such as shown in Figure 4.6b.

There is lack of information on LED's datasheet regarding its ESD protective device, other than it is connected in parallel with the LED chip and that the ESD withstand voltage is 8kV.

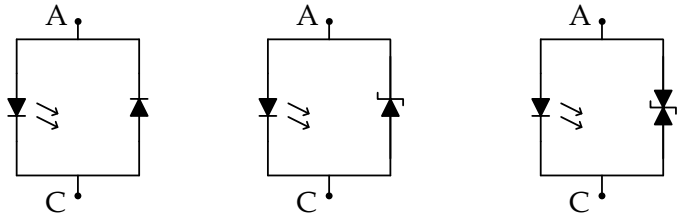

(a) Diode (b) Zener Diode (c) TVS Diode

Figure 4.7: Various types of ESD devices configurations, parallel with the LED.

Figure 4.7 shows some of the possible ESD configurations, in parallel with the LED - single, Zener and TVS (Transient Voltage Suppression) diodes in Figures 4.7a, 4.7b and 4.7c respectively.

When the LED is forward biased, the ESD devices are transparent - they do not alter the LEDs functionality, because they themselves are reverse biased. However, when the LED is used as a light sensor, the ESD devices are forward biased. Their implication in the use of LEDs as light sensors is further investigated below.

4.4 Circuit topologies for 'LED-as-sensor'

There are two main modes or topologies in which photodiodes and/or LEDs can be used. These are the photoconductive and photovoltaic modes. The main difference in these modes relies in the use or not use of a reverse bias voltage.

4.4.1 Photovoltaic Mode

In photovoltaic mode, the diode is operated in unbiased fashion ($V_{bias} = 0V$). The lack of an external reverse voltage will yield a shorter depletion region W_d, and thus a higher junction capacitance C_j. This results in a higher diode time constant, and therefore in a slower response.

Besides the system's response, two other factors differ between these two modes - dark current value (I_{dark}) and linearity. I_{dark} can be investigated using the simplistic equivalent circuit of a reverse-biased diode in Figure 4.4a.

C_j is function of V_{bias}, whereas I_{gl} is the photon-generated current. R_{dark} represents the shunt resistance of the diode. Ideally, this would be infinite, but real values are in the 10-1000 MΩ range. This represents the noise or dark current I_{dark} - current that flows even in dark environments. By applying a voltage on both diode terminals, a current is forced through the resistor, independently of the incident light (I_{gl}). If the diode is operated in photoconductive mode, I_{dark} is never null, consequent of the reverse bias voltage. On the other hand, by operating the diode in the photovoltaic mode I_{dark} is null.

The reverse bias voltage also defines the upper current saturation limit - i.e., the upper linearity limit. Observing Figure 4.8, one can see six different photodiode operating points, grouped in two states. While both share the same load impedance (same line slope), $\overline{abc}$ represents the photodiode's operation in photoconductive mode, and $\overline{def}$ represents the photovoltaic mode. Comparing operating point pairs, for the same illuminance levels - *ad*, *be* and *cf*, one can see larger differences between these two points, as illuminance increases. While the current increases linearly with illuminance in the photoconductive mode, in photovoltaic mode it does not - as illuminance increases, current appears to saturate. This is more visible in Figure 4.9. As V_{bias} is increased, the saturation current is 'pushed' upwards - one can say that linearity is higher with higher V_{bias}, as the linear operating zone is 'stretched'.

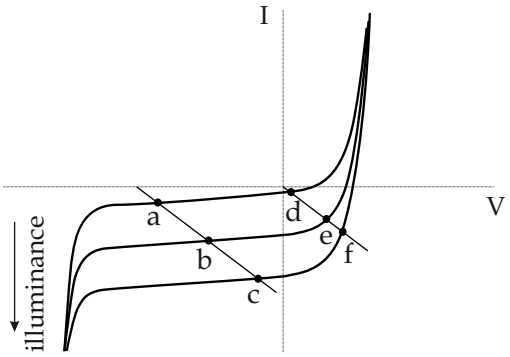

Figure 4.8: Photodiode IV curve (adapted from [63]).

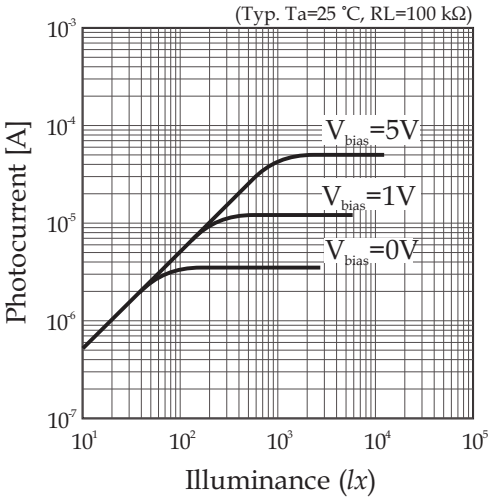

Figure 4.9: Photodiode Linearity (adapted from [63]).

4.4.2 Photoconductive Mode

In this mode, an external reverse voltage is applied to the diode. As confirmed by Figures 4.2 and 4.3, the depletion region W_d is widened, thus reducing the junction's capacitance C_j - the device's response speed is therefore increased. However, due to the device's enhanced sensitivity, by using a reverse voltage, the dark current is also increased.

4.4.3 Charge/Discharge Mode

An alternative mode was proposed in [11]. Dietz et al. proposed the use of the capacitive properties of the reverse biased p-n junction as a means to sense incident light. By reverse biasing the LED, the junction capacitance is charged - the time it takes to discharge depends on the current created by incident light. The higher the illuminance the faster C_j is discharged. The remaining voltage on the capacitor after a measuring period dictates how much light has been sensed. A low remaining voltage means that the capacitance was discharged completely or almost completely, whereas a higher remaining voltage indicates that not enough photocurrent has been generated to discharge the capacitance. This method gains special importance when using a modern μC, as it does not require extra circuitry - two existing I/O pins on a μC are sufficient.

This method can be divided into two stages:

- Charging stage (Figure 4.10a): one of the I/O pins is set to HIGH logic level, while the other one is set to a LOW logic level, 5V and 0V respectively. In this stage C_j is charged up.
- Discharging stage (Figure 4.10b): the HIGH pin is then set to an INPUT pin for an ADC. Incident light thus discharges C_j and the remaining voltage can be monitored by the microcontroller's input pin.

It should be noted that the I/O pin impedance is altered, as the pin is changed from an OUTPUT pin to an INPUT pin. Whereas the pins impedance is very low in OUTPUT mode, it is much higher in INPUT mode. Furthermore, the junction capacitance's value - C_j - is not constant. As it is discharged by effect of the incident light and as the voltage at its terminals decreases, C_j value increases, as seen in Figure 4.3. Thus, the junction capacitance should indeed be referred to as $C_j(t)$, as it is variable - however, for simplicity reasons it is referred to as simply C_j.

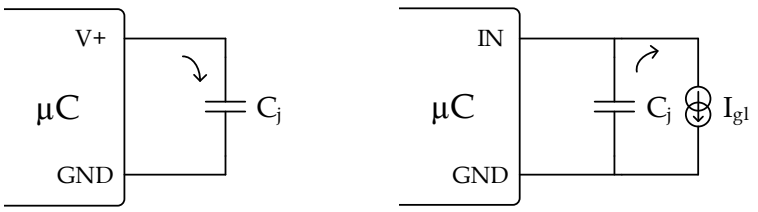

(a) Charging C_j Capacitance (b) Incident Light discharging C_j

Figure 4.10: Charge/Discharge Mode stages.

Dietz et al. ([11]) also improved on the idea of using the LED as a bidirectional interface. By using a time-slot scheme it is possible, provided that the frequency is high enough, to alternate between the receiving state and the emission state while keeping the LED apparent state as "on". Figure 4.11 illustrates this. In the state represented by Figure 4.11a the LED is used as an emitter. States represented by Figures 4.11b and 4.11c show the LED used as a sensor, in a Charge/Discharge Mode. Shifting between these states rapidly enough gives the impression that the LED is always on (i.e., emitting), while in fact, it is not. The speed at which the LED goes through the emitting and sensing states is closely related to humans maximum *flicker-fusion frequency*, as previously discussed.

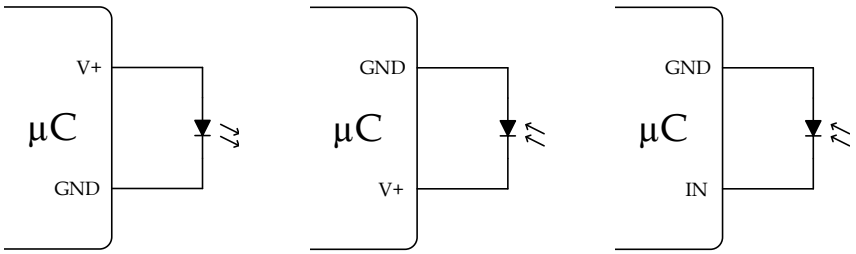

(a) (b) (c)

Figure 4.11: LED as a Bidirectional device.

4.5 'LED-as-sensor' experiment

Based on the work of Dietz et al. [11], colour LEDs were experimented as light sensors, using the 'Charge/Discharge' topology described above. This method takes advantage of not requiring any extra circuitry, such as transimpedance amplifiers for I/V conversion.

4.5.1 SPICE Simulation

SPICE tools can, in fact, be effectively used to simulate and prove both the capacitive nature of the reverse-biased LED, but also their sensitivity to external light, resorting to a model approximation. Although external, physical constraints, as those pointed out in Section 4.3, aren't modelled, the LEDs electrical behaviour can be studied. The LED model used for SPICE simulation referred to the Lumileds LXHL-BW02.

The capacitive character of a reverse-biased LED can be demonstrated with a direct comparison with a capacitor. Comparing an ordinary RC network (low-pass filter) with a reverse biased LED, in an AC analysis, one can find the equivalent capacitance value specific to that bias value. By using a DC voltage source with a comparatively small AC component it is possible to use the LED in the same operating point, keeping C_j's variation to a minimum. Figure 4.12 and 4.13 show the simulated circuit and simulation results. Through intensive simulations, it was found that a capacitance of 500 pF accurately models that of the reverse-biased LED, and allows for the superimposition of both frequency responses.

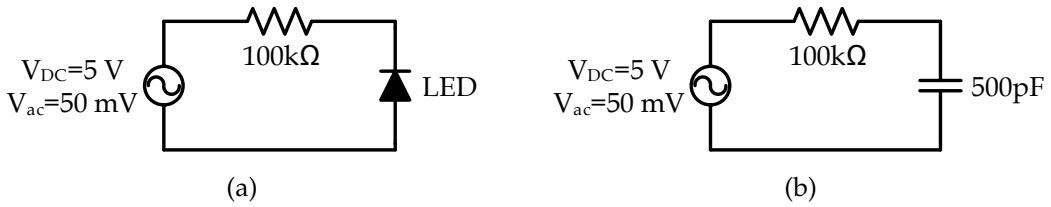

Figure 4.12: Simulated Circuits for Reverse Biased LED (a) and Capacitor (b) comparison.

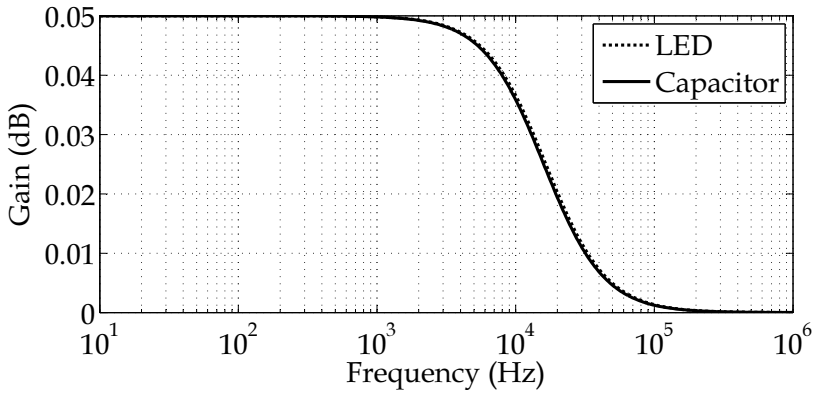

Figure 4.13: Simulation results for Reverse Biased LED and Capacitor Low Pass Filter.

An alternative, more exact method for the capacitance calculation of a reverse-biased diode can be performed, based on the purely imaginary current behaviour of capacitive loads. Referring to Figure 4.14, one can approximate the LED as a purely capacitive load.

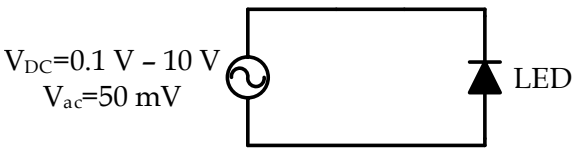

Figure 4.14: LEDs' ESD device when used as light sensor.

When examining a load under an AC stimulus, its impedance can be represented by a complex number - the real part represents the resistive character of the load (resistance), whereas the imaginary part (reactance) is frequency dependent and constitutes the reactive component of said load. A purely capacitive or inductive load (like a reverse-biased LED) has a purely imaginary impedance component (Equation (4.3)). A capacitor's reactance can be written as in Equation (4.4) - it depends on the capacitor's value and on the frequency of the AC stimulus, $\omega = 2 \times \pi \times f$. Equation (4.6) demonstrates that the imaginary part of the current

divided (Im(I)) by the voltage V times frequency ω equals the equivalent capacitance of the reverse-biased voltage. Setting frequency f as $f = 0.5/\pi$, permits the simplification $C = \text{Im}(I) \times \frac{1}{V}$, as also suggested in Equation (4.5)

$$Z = R + jX \overset{R \to 0}{=} jX \tag{4.3}$$

$$X = X_c = -\frac{1}{\omega C} \tag{4.4}$$

$$X_c = -\frac{1}{2 \times \pi \times f \times C} \overset{f \to 0.5\pi}{=} -\frac{1}{C} \tag{4.5}$$

$$\begin{gathered} Z = \frac{V}{I} \Leftrightarrow jX_c = \frac{V}{I} \Leftrightarrow -j\frac{1}{\omega C} = \frac{V}{I} \Leftrightarrow \frac{1}{j\omega C} = \frac{V}{I} \Leftrightarrow \\ j\omega C = I \times \frac{1}{V} \Leftrightarrow j\omega C = j\text{Im}(I) \times \frac{1}{V} \Leftrightarrow \\ C = \text{Im}(I) \times \frac{1}{\omega V} = \text{Im}(I) \times \frac{1}{V} \end{gathered} \tag{4.6}$$

By sweeping the DC component of the AC voltage source, it is possible to plot the V_{BIAS} against C_j, as per Figure 4.15. The matching capacitance value for a *n=1* LED string with $V_{BIAS} = 5$ V is $C_j = 481.7$ pF, which supports the approximated aforementioned value of 500 pF.

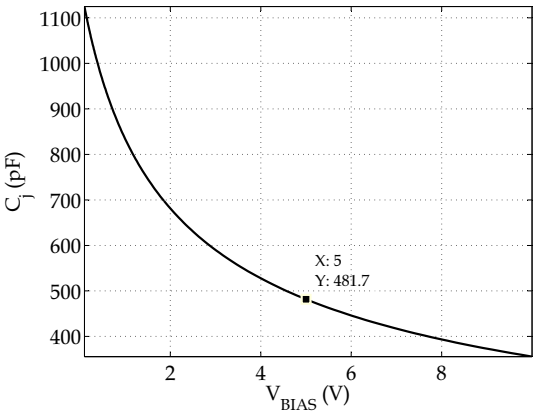

Figure 4.15: V_{BIAS} vs C_j plot obtained from SPICE simulation.

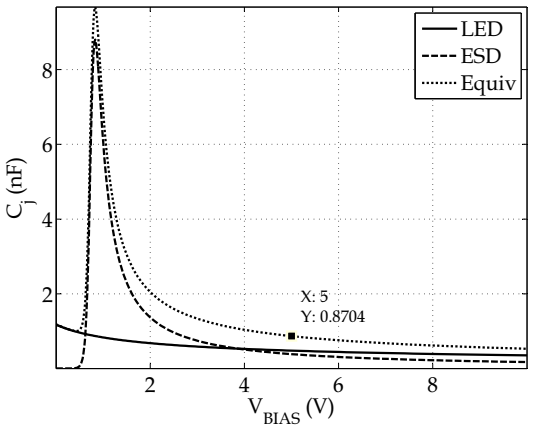

Figure 4.16: V_{BIAS} vs C_j plot obtained from SPICE simulation, for LED, ESD Device and Equivalent Capacitance.

Adding a parallel ESD device, it is possible to investigate its influence on the LED's operation as a light sensor (reverse-biased). Specifically, it is important to look into how its addition to the circuit affects the overall equivalent capacitive

load. Diffusion Capacitance C_d is associated to a forward-biased diode, which happens to be the ESD device itself. Performing the same analysis as above, one can measure C_d against a DC sweep. Given that the reverse-biased diode's C_j and the forward-biased diode's C_d are in fact in parallel, the equivalent capacitance results in the sum of these two capacitances, Figure 4.16. The equivalent capacitance of the LED package is higher, when compared to the single LED chip capacitance (C_j), due to the fact that it also includes the ESD diode capacitance (C_d). At $V_{BIAS} = 5$ V, the equivalent capacitance almost doubles the single LED chip capacitance. However, at lower voltages, a large capacitance peak can be detected, roughly centered at the diode's threshold voltage - thus $V_{BIAS} = V_{t(ESD)}$.

SPICE software can also serve as a means to simulate the 'LED-as-sensor' experiment altogether. In fact, it proves as an effective tool in investigating the influence of the parallel ESD diode, as well as the response of multiple LEDs in series and/or parallel, which may not be possible in the experiment setup. Figure 4.17 shows the simulated circuit for charge and discharge states with and without the parallel ESD device in 4.17a and 4.17b respectively. Note that the series resistor's value is set accordingly to the state, modelling the input and output impedances of the μC's pins. - in charge state, the output impedance is low (R$\rightarrow$1 Ω), whereas the input impedance in the discharge mode is very high (R$\rightarrow$1 MΩ).

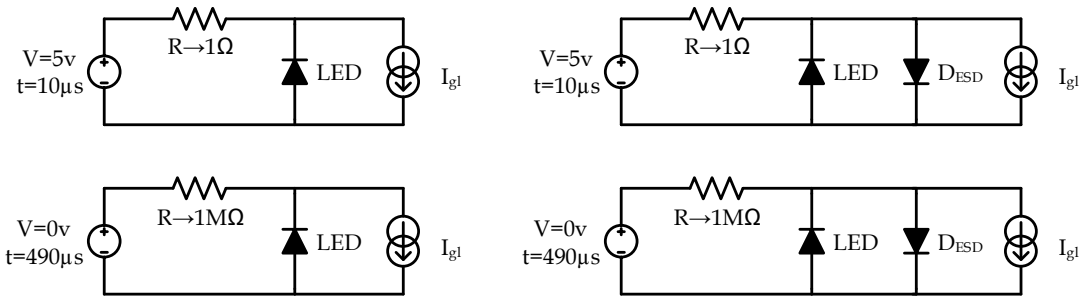

(a) Charge and Discharge states without ESD

(b) Charge and Discharge states with ESD

Figure 4.17: Schematic of the used circuits for SPICE simulation.

The incident light is modelled by the parallel current source I_{gl}, with a symbol period of $t = 500$ μs and duty-cycle of 50%. In both waveforms an increased discharge in the first and third periods is clearly visible. The dotted line - which represents the charge/discharge curve for the LED without ESD device - is very resemblant to the obtained waveform from the experiment, as is also the solid line. One can clearly distinguish both waveforms, either by their amplitude or by the

discharge curves. The dotted line is larger in amplitude and its discharge curve is very much alike the exponential curve one would obtain from an RC circuit.

The solid line, on the other hand, is smaller in amplitude, because of the limiting effect of the forward biased diode. The discharge curve is also very different. It is very steep as it begins to discharge, but not so much as time passes by. Even though the presence of an ESD device increases the equivalent capacitance of the LED (refer to Figure 4.16), it does not interfere with the discharge curve as much as one would think it should. This can be explained by the variable current source/sink characteristics of a diode (see Figure 4.26). At higher voltages, it sinks more current, draining the capacitors charge (i.e., discharging the LED's capacitance) - as the voltage drops this current sink effect is lessened.

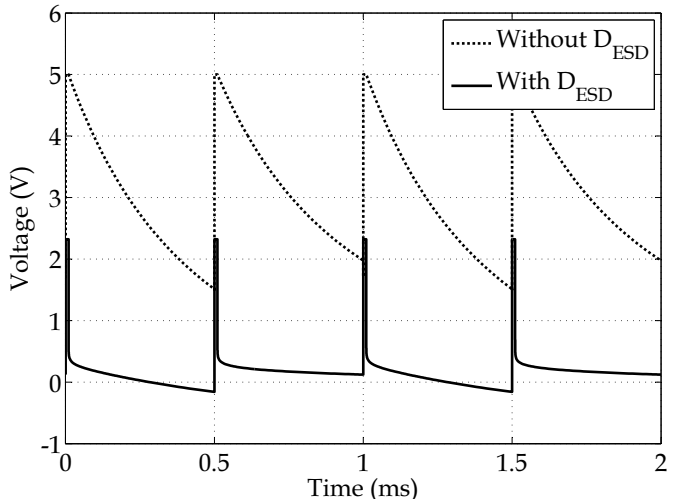

Figure 4.18: Waveforms obtained by SPICE simulation using setup in Figure 4.17.

4.5.2 Physical implementation

Two LEDs were used at the same time in each experiment. One served as the transmitter, the other one as the receiver - these will be referred to as Tx and Rx, respectively, henceforth. The chosen micro-controller was the Atmel ATMEGA328[1] - the built-in ADC was used. No current limiting resistor was used, as the I/O pins are current limited. Figure 4.19 illustrates the used setup for the experience.

Contrarily to [11], where Dietz et al. used exclusively digital I/O pins for both anode and cathode, a digital pin on the anode and an analog pin on the cathode were used in this setup. The method utilized by Dietz et al. relied on the time necessary for the LED's capacitance to discharge to the digital pin's input threshold

[1]Both Tx and Rx microcontrollers were synchronized using an external signal generator

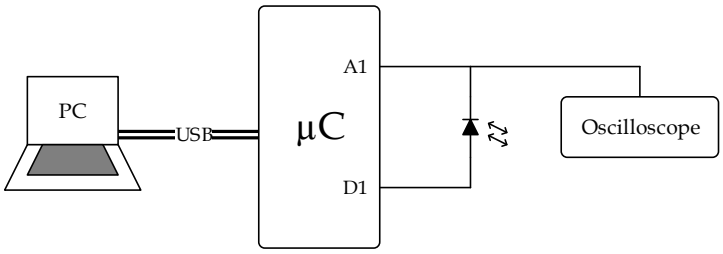

Figure 4.19: Experiment setup.

- the voltage threshold between the logic levels of 0 and 1. If it discharged quickly, that meant that light was sensed - if it did not discharge as quickly, no light was sensed. Obviously this method, though simple and definitely usable, ignored all other light conditions, between ON and OFF. By using and analog I/O pin on the cathode, one can use the μC's inboard ADC, and add flexibility to the system. A couple of different algorithms could be used. One could establish a certain threshold within the ADC's range and compare that value with the current value on the cathode. Changing the threshold value could change the interpretation of the light/no light distinction. Lower thresholds could be useful in the event that dim/no light distinction is needed. Because the discharge is exponential, and all discharge curves have the same initial voltage, two very similar discharge curves (such as in the case of no light/dim light) will become more distinct as more times passes by. This does, obviously, slow down the system. One disadvantage of the system's slow speed is the fact that it may become more sensitive to ambient light. Higher threshold levels are useful when comparing bright light/no light, as the exponential curves become distinct of each other much more quickly - the system is thus quicker. Another way of using this mode may be by having it be periodic. That is, by charging and discharging the LED periodically (at a fixed frequency). This method has some benefits compared to the earlier algorithm. Because it is periodic, it is also predictable. A single ADC measure can be performed just before it is charged back up again. Larger measured values mean lower light levels - incident light did not discharge the LED's capacitance. Lower values mean that the incident light is higher, and the LED's capacitance has been discharged. One is not limited to two states (light/no light) - in fact, one is only limited to the ADC's resolution. Theoretically, for a 10 bit ADC there should be 1024 detectable light levels.

Three LED types were used: 3 mm and 5 mm through hole and 1 mm^2 surface mount. Table 4.1 describes both the micro-controller and LED specifications. Both LEDs Rx and Tx were aligned with each other, mounted on two different sides

Table 4.1: Experiment system specifications.

Microcontroller		Atmel ATMEGA328P	
Microcontroller clock		16 MHz	
ADC Resolution		10 bit	
ADC Clock		1 MHz	
V_+		5 V	
3mm LED	Red	Vishay TLUR44K1L2	630 nm
	Green	Vishay TLHG44K1L2	567 nm
	Blue	Vishay TLHB44K2M1	466 nm
5mm LED	Red	–	–
	Green	–	–
	Blue	–	–
SMD LED	Red	OSRAM LH-W5AM	640 nm
	Green	OSRAM LT-W5AM	528 nm
	Blue	OSRAM LD-W5AM	455 nm

of an enclosed 9x9 cm square box. For LEDs of the same type, the two opposite sides were used (Figure 4.20a). The horizontal alignment error from one another was under $\pm$ 2º. All the LEDs were from the same manufacturer and from the same model, whenever possible, to keep features such as chip size, angle of half intensity and luminous intensity as similar as possible from LED to LED. The through hole 3mm LEDs feature a tinted package, coloured same as their emission. On the other hand, the 5mm and the SMD LEDs have a clear silicon package. Figure 4.20 depicts the experiment LED assembly.

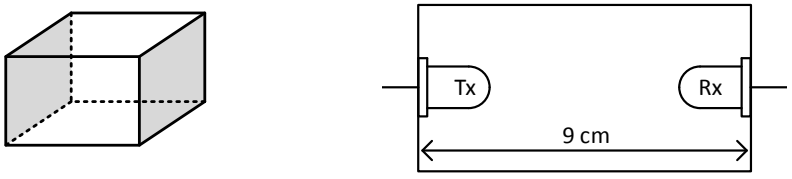

(a) Enclosed box setup for LED-to-LED experiment

(b) Cross-section of enclosed box setup

Figure 4.20: Physical Assembly of the LED-as-sensor experiment.

The Tx LED was pulsed with a square wave, at a frequency of 500 Hz with 50% duty-cycle. The Rx LED worked solely as a receiver using the Charge/Discharge mode, in a periodic fashion. Every 500 μs the LED was reverse biased (note that the LED was kept in reverse bias operation for 10 μs prior to discharge), then allowed

to discharge. This meant that, when synchronized, the Rx discharge curve would indicate "light-seen" for two consecutive measuring periods and "light-not-seen" for another two consecutive measuring periods.

4.5.3 Experiment Results

4.5.3.1 3 mm LEDs

Figure 4.21 shows Rx-Tx tests for Red-Red LEDs.

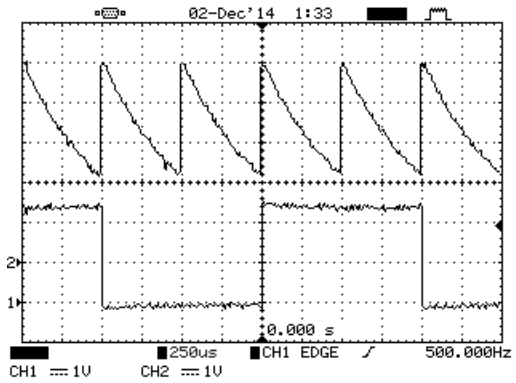

Figure 4.21: Rx (Top) and Tx (Bottom) 3 mm LED Red-to-Red Waveforms.

Rx \ Tx	R	G	B
R	–	–	–
G	–	–	–
B	–	–	–

Table 4.2: 3 mm Rx-Tx experiment results.

The Rx LED is depicted by the top waveform, whereas the bottom waveform represents the Tx LED. One can clearly see the discharge curve of the Rx LED. However, for these LEDs, it is clear that the incident light does not alter in any way the discharge curve, as there is no difference in the remaining voltage on the junction capacitor after a discharge period in both light and dark states. This is consistent for all the three coloured LEDs, both as emitters and sensors. Table 4.2 summarizes the obtained results for the 3mm LED experiment. There is no light detection in any of the 9 possible LED combinations.

4.5.3.2 5mm LEDs

The 5 mm LEDs, on the other hand, presented better results, particularly in the *Red-Red*, *Green-Blue* and *Blue-Blue* Rx-Tx pairs, which had clear distinction between light and dark states. Other combinations did not show relevant light detection. Figure 4.22 shows Rx-Tx results for Green-Blue, and table 4.3 summarizes the obtained results.

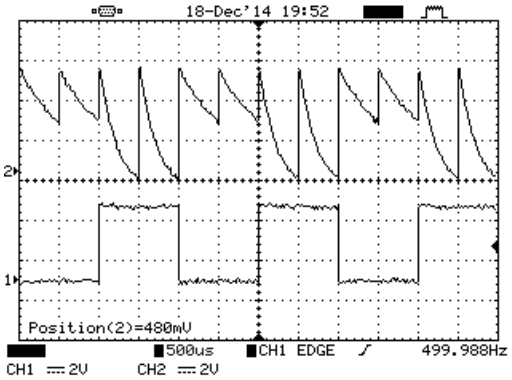

Figure 4.22: Rx (Top) and Tx (Bottom) 5 mm LED Green-to-Blue Waveforms.

Rx \ Tx	R	G	B
R	√	–	–
G	–	–	√
B	–	–	√

Table 4.3: 5 mm Rx-Tx experiment results.

4.5.3.3 SMD LEDs

The SMD LEDs, much like the 5mm LEDs proved to be better light detectors than the 3mm LEDs as well. Figure 4.23 shows Rx-Tx results for the Red-Green LED pair, and table 4.4 summarizes the obtained results.

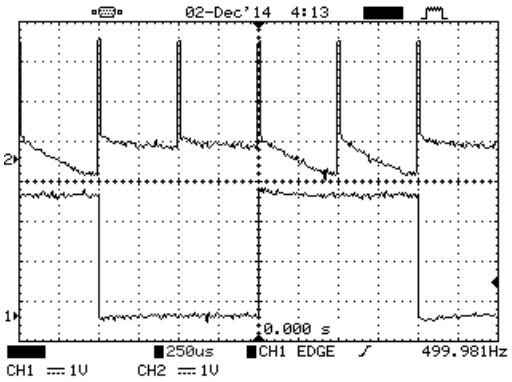

Figure 4.23: Rx (Top) and Tx (Bottom) SMD LED Red-to-Green Waveforms.

Rx \ Tx	R	G	B
R	√	√	–
G	–	–	√
B	–	–	–

Table 4.4: SMD Rx-Tx experiment results.

4.5.4 Results Interpretation

None of the experiment results show any light sensing by the 3mm LEDs. On the other hand, there is clear distinction of Rx waveforms when exposed to light in the Red-Red, Green-Blue and Blue-Blue 5mm Rx-Tx LED pairs. Likewise, for the Red-Red, Red-Green and Green-Blue SMD LED pairs. The package colour differences between the 3mm and 5mm LEDs is a major influence on their light sensitivity, given that both these share the same approximate chip size (0.1 mm^2). They have, however, different package sizes, and thus the exposed package area is not the same, which means that number of photons to reach the p-n junction on the 3mm can be lower than those on the 5mm. Note that the SMD LED's results show good light sensitivity, on a par with the 5mm LEDs. Again, package colour has great influence - both of these have a transparent silicon dome. Additionally, the exposed p-n area is much larger than the one found in both the 3mm and 5mm LEDs, which can explain the frankly good sensitivity.

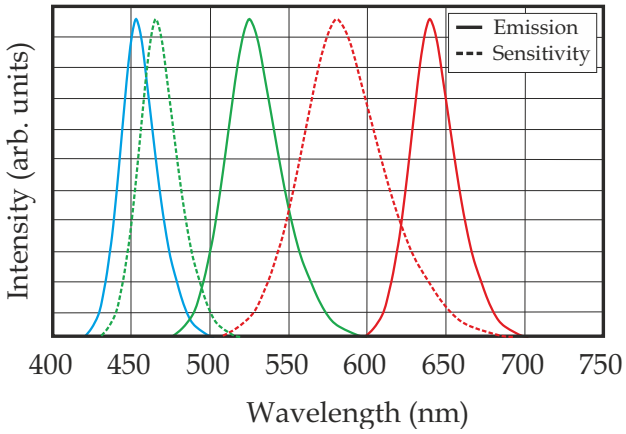

Figure 4.24: Approximated Emission and Sensitivity Spectra.

One aspect that can be collected from Tables 4.2 to 4.4 is the fact that the light sensitivity demonstrated by the Rx LEDs is more apparent when the Tx emission wavelength is equal or larger than that of the Rx pair. Take, for instance, the case in Table 4.4, referring to the SMD-SMD results. While the Red Rx LED is sensitive to both Red and Green light, the Green Rx LED is sensitive only to Blue light - the Rx LEDs are sensitive to light equal or lower in wavelength than their own emission. Referring to Section 3.1 and Figure 3.2, the energy of the emitted photons by the LED is related to the difference in energy levels that electrons transit from and to. The bandgap energy eV is inversely proportional to the emission light wavelength. Similarly, referring to Section 4.2 and Figure 4.1, the necessary photon energy to create a free electron-hole pair is given by eV, the p-n junction bandgap

energy. These two characteristics - emission and sensitivity spectra - seem not to coincide when, at first glance, they should. For sufficiently large wavelengths, the quantum efficiency of the photodetector - in this case, the reverse-biased LED - is small, because photon energy is insufficient to overcome the junction's bandgap. On the other hand, for sufficiently small wavelengths, light penetration depth is diminished. Given that recombination lifetime is quite short near surface, the carriers recombine before being swept, [57]. Given that an LED is not constructed to be used as a photodetector, its sensitivity spectra is very narrow, slightly below its emission spectra. The obtained experiment results are coherent with other experimental results in the literature [64, 65, 66]. Figure 4.24 depicts the emission and approximated sensitivity spectra for the SMD LEDs. Note that the sensitivity spectrum peak wavelengths are lower than that of the emission spectrum. Also, the sensitivity spectrum of the Red LED covers both Green and Red emission spectra.

Finally, the waveform differences between Figures 4.22 and 4.23 are explained by the presence of an ESD device in the latter case. The ESD device interferes with the LED in both charge and discharge states, as seen in Figure 4.25.

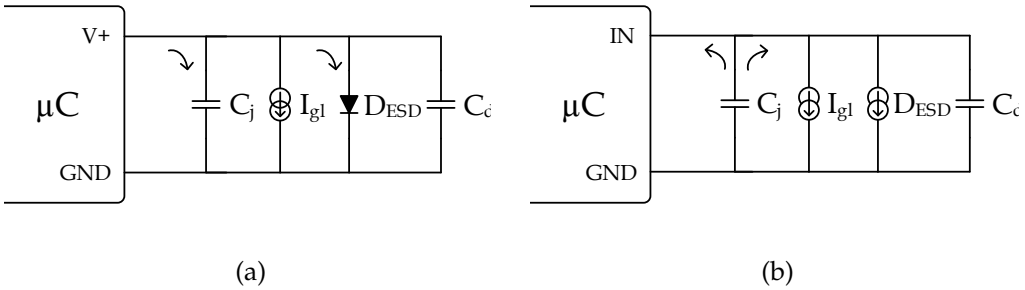

Figure 4.25: LEDs' ESD device when used as light sensor.

When in charge state (Figure 4.25a), the ESD diode works as a voltage limiter. Given that the current sunk by the μC is not very high, it is very unlikely that the ESD diode voltage stays at 5 V. Therefore, the voltage to which the junction capacitance C_j charges to is, in fact, limited. This explains the reduced amplitude in Figure's 4.23 waveforms. When in discharge state (Figure 4.25b), the ESD device works as a variable current sink, further discharging junction capacitance C_j. Additionally, the diffusion capacitance of the forward-biased must also be taken into account.

The microcontroller's ADC input impedance is very high, and its input current will therefore be very small. C_j's discharge in thus dependent on the two parallel current sinks: I_{gl}, the current generated by incident light and D_{ESD} a current sink dependent on terminals voltage. While on one hand, and for a given ambient illuminance, the current sunk by I_{gl} is constant, on the other hand the current sunk by D_{ESD} does not have a completely linear behaviour. This can exemplified by Figure 4.26. Point A represents the initial operating point as C_j begins to discharge - as it discharges, the node's voltage decreases, which brings D_{ESD} operating point down to B and ultimately C. In other words, the higher the stored energy the C_j the more quickly it is discharged. Passed point C, the current sunk by the ESD diode is depreciated, and C_j is solely discharged by I_{gl}.

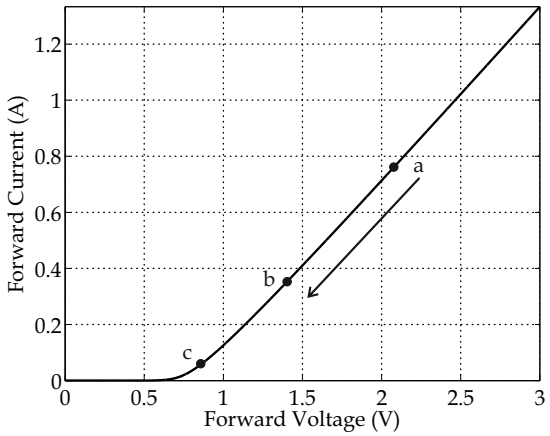

Figure 4.26: Diode's VI curve.

4.5.5 Bi-Directional Communication with LEDs

Considering the spectral selective characteristics of an LED as a photodetector, they can be used as both input and output ports, on a bi-directional communication system, in half-duplex fashion. Using LEDs with three distinct wavelengths - Red, Blue and Green - it is possible to create a two channel Wavelength-division Multiplexing (WDM) system. The system is demonstrated in Figure 4.27. Tx and Rx periods may represent a single bit of information, or even higher bit data packets.

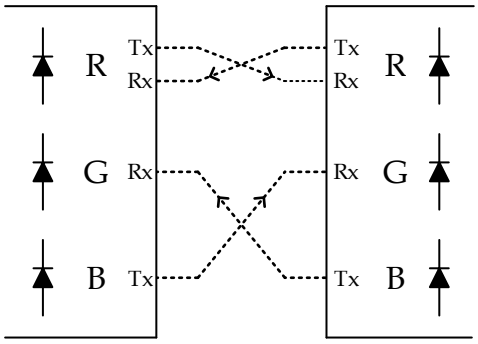

Figure 4.27: Fully-LED Bi-directional System.

The Red LED acts as a transceiver by itself. By using a *time-slot* scheme, it is possible to use it as both emitter as receiver, thus working as both Rx and Tx. On the other hand, the Blue and Green LEDs act as emitter and receiver, respectively. The Tx and Rx is merely a notation that describes the LEDs role in the communication system. Provided that there is enough wavelength separation between the Red sensitivity and the Green emission spectra, it is possible to obtain two fully independent communication channels, using purely WDM - any information multiplexing is hardware based. Additionally, in case of superposition between the Red sensitivity and the Green emission spectra - like what was interpreted from the collected data shown in Section 4.5.3 - the Red and Green states on a given system must be opposite of each other because Red LEDs may be sensitive to Green light. Figure 4.28 depicts this. This way, when the Green LED of system B is on (lit up), it will not be sensed by the Red LED of system A, because it itself is emitting. The Blue LED could be used for sunlight sensing, due to its sensitivity to ultraviolet wavelengths (which exist in sunlight). In case of using a RGBA (with an added Amber colour, which improves CRI), the Green colour could be used as Tx and the Amber could be used as Rx.

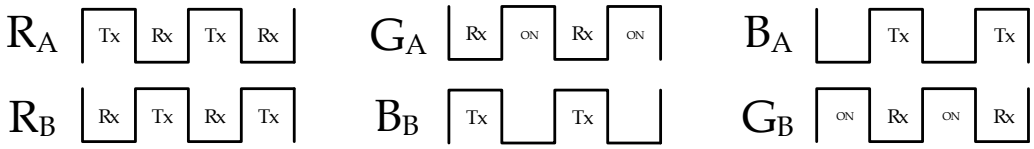

Figure 4.28: RGB LED states.

One aspect that may be important to assess is the achievable data-rate. Firstly, the capacitive nature of the LEDs must be considered. A too high clock rate will not allow the LED's capacitance to discharge properly, and thus light/no-light differentiation is hampered, as shown in Figure 4.29, which show the Rx LED waveform for an optical clock rate of 5 kHz and 10 kHz respectively. Clearly, light/no-light distinction is greater in the first case. As optical clock rates increase, there is need for a faster discharge curve - and thus, a lower capacitance. In the next subsections, alternative receiver setups are suggested for both increased speed and/or sensitivity. SPICE simulation can be used to simulate the behaviour of a string of n LEDs, as one would find in an LED luminaire, or even a segment, where similarly-sized LED strings are used in parallel.

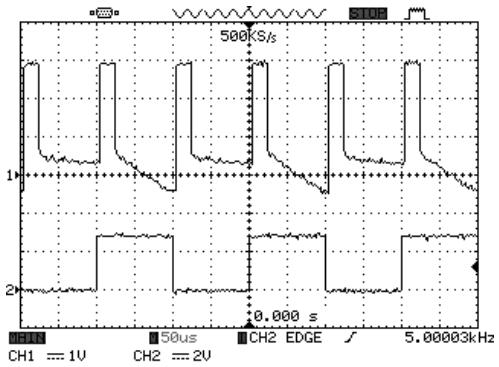

(a) Optical Clock = 5kHz

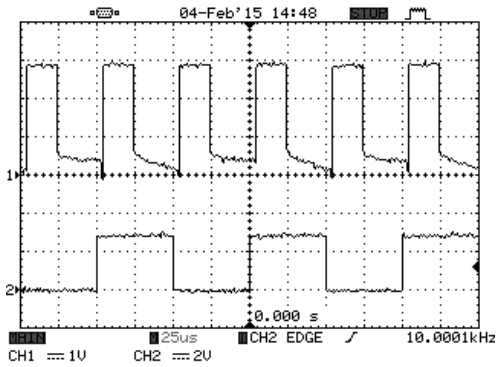

(b) Optical Clock = 10kHz

Figure 4.29: Influence of optical clock rate on a 'LED-as-sensor'.

4.5.5.1 LED Strings with n>1

At first glance, it is important to understand the LED string in terms of equivalent circuit, especially when reverse biased. Referring to Figure 4.4a and 4.13 is known that a reverse biased LED behaves very much like a capacitor. It is to be expected that a series of identical reverse biased LEDs would behave like a series of equally valued capacitors as seen in Equation (4.7)

$$C_{series} = \frac{1}{\frac{1}{C_{j1}} + \frac{1}{C_{j2}} + \frac{1}{C_{j3}} + \frac{1}{C_{j4}} + ... + \frac{1}{C_{jn}}} = \frac{1}{n * \frac{1}{C_j}} = \frac{C_j}{n} \,. \tag{4.7}$$

However, and as noted in Figure 4.15 and Figure 4.3, the junction capacitance C_j of a reverse biased p-n junction depends on the reverse bias voltage applied to the entire string. Thus, and referring to Figure 4.15 and Equation (4.7), it's possible to study the effect of string size in the overall junction capacitance value.

$$V_{bias} = 5V \Rightarrow C_j = 481.7pF \text{ and } V_{bias} = 0.5V \Rightarrow C_j = 963.4pF$$
$$C_{series} = \frac{963.4pF}{10} = 96.34\ pF \tag{4.8}$$

For a string of $n = 10$ LEDs the reverse voltage for each LED is $V = 0.5$V, which equates in a junction capacitance of $C_j = 963.4$ pF per LED, and total capacitance equal to 96.34 pF, as confirmed by the dotted curve in Figure 4.30 and Equation (4.8). Therefore, even though the each diode is biased in a lower voltage point, resulting in a higher junction capacitance, equivalent total capacitance is computed by this series of higher valued capacitors which makes the total value smaller than the junction capacitance for a single string LED. Figure 4.32 shows how C_{series} value depends on both string size n and Bias Voltage V_{BIAS}. One can derive that, for longer LED strings, the total series capacitance flattens out, compared to what happens in short or single LED strings, as can be seen in Figure 4.30, for $n = 10$. This fact can be confirmed by examining the junction capacitance C_j capacitance equation and how it morphs, as the string's LED number enlarges - series capacitance changes with n in a $\left(\sqrt{\frac{V_{BIAS}}{n}} \times n\right)^{-1}$ relationship. From Figure 4.30 it is evident that the increasing of series LEDs leads to an overall flattening of the C_j/V_{BIAS} curve.

Likewise, the depletion capacitance of the ESD device is also changed. In a $n = 10$ LED string, each ESD device operates on a lower (by tenfold) operating bias point, and thus the equivalent series depletion capacitance is computed as in Equation (4.7). From Figure 4.31 it is evident that the increasing of series ESD

devices leads to an overall flattening of the C_j/V_{BIAS} curve, but also a shift. The capacitance peak follows the overall threshold voltage of the ESD string (V_t is ten times higher with $n = 1$ than with $n = 10$), and its effect on operation is minimized as the series LED string size increases.

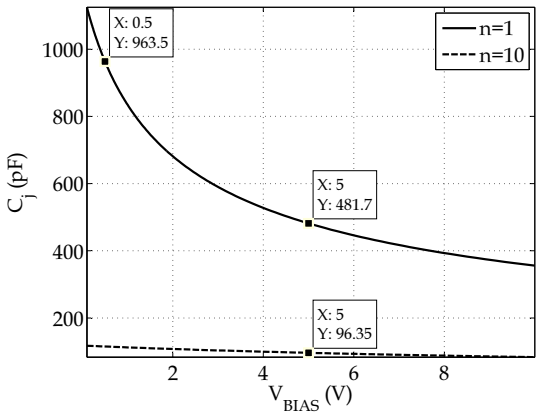

Figure 4.30: V_{BIAS} vs C_j plot obtained from SPICE simulation for n=1 and n=10 LED strings.

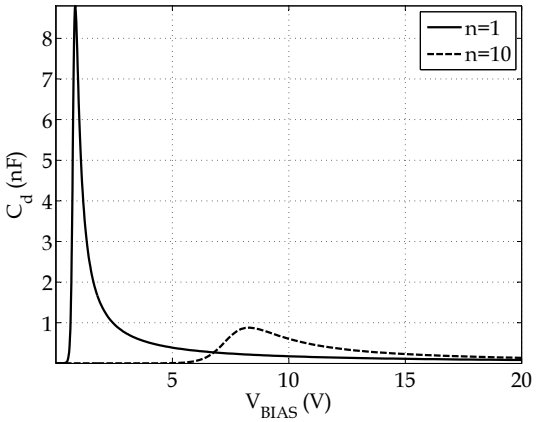

Figure 4.31: V_{BIAS} vs C_d plot obtained from SPICE simulation from ESD Device for n=1 and n=10 strings.

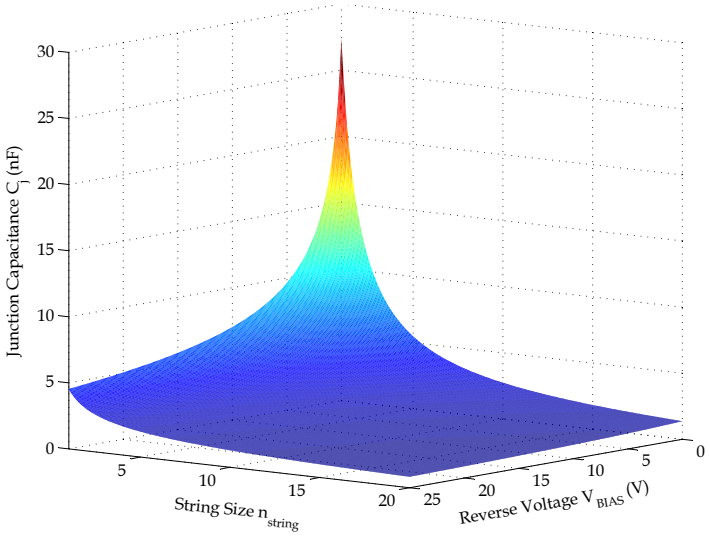

Figure 4.32: 3D plot of Series Capacitance of a Reverse Biased LED String with variable size and bias voltage.

SPICE simulation results for a string of 10 LEDs are shown in Figure 4.33. In opposition to the previous case of a single LED string, the voltage at the string's terminals is not limited by the ESD devices. Given that there are now 10 ESD diodes parallel to the LEDs, the reverse voltage is now distributed by all diodes,

allowing each diode to operate in a lower V_f / I_f bias point such that the overall operating point of the string allows the LED's voltage to match the input voltage. Likewise, comparing the solid curves (with D_{ESD}) of Figures 4.18 and 4.33, the latter's discharge curves are not as steep - the ESD diodes are operating at a lower bias point, and thus do not sink as much current. Recalling Figure 4.26, the each ESD diode is operating around point C, and thus the ESD diode string draws very little current from the moment the discharge commences. Furthermore, at this operating voltage, for a $n = 10$, the equivalent capacitance for LED strings with and without ESD devices are very similar, as predicted above. As the LED string size enlarges, effect of the ESD device is lessened.

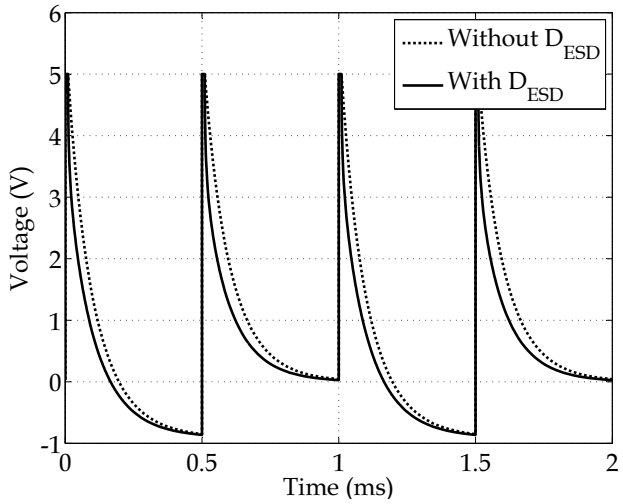

Figure 4.33: Waveforms obtained by SPICE simulation using setup in Figure 4.17 for a string of 10 LEDs.

Figure 4.34 shows how both waveforms change by varying the string size, while maintaining the reverse voltage bias at 5V. Figure 4.34a in particular confirms, in fact, the above statements regarding the total string C_j value, ie C_{string}. Keeping V_{BIAS} constant, longer LED strings originate a smaller equivalent capacitance, and consequently faster discharge curves. Regarding 4.34b, it shows that the ESD device has most impact on smaller strings.

Nonetheless, the reverse voltage applied to the LED string size should also be related to its size. For a reverse bias of 5V and a string of $n = 10$ LEDs, one can say that LEDs with or without ESD devices give the same results as shown by Figure 4.33). However, for a higher reverse bias voltage of e.g. 50V, will not show similar results - the LED string without ESD devices will, in fact, be reverse biased at 50V, whereas the reverse bias on the LED string with ESD devices will be limited (much like what occurs in Figure 4.18), consequence of the now higher operating point of the ESD diode. The fact that the LED string can be reverse biased at higher

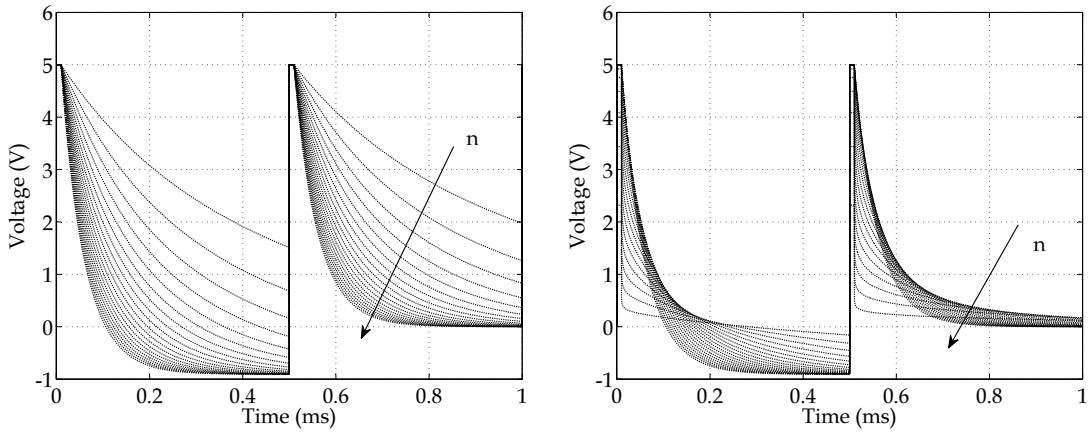

(a) without ESD (b) with ESD

Figure 4.34: Waveforms for LED string of variable size n (with and without ESD device).

voltages is of great importance, given that it allows for the use of the same AC-DC or DC-DC Converter one would use to forward bias an LED string on a common LED luminaire. The PWM signal used in these circuits could then be used not to merely turn on or off the LED string, but to decide when should the LED string be forward or reverse biased.

4.5.5.2 Parallel LED Strings

While adding identical capacitors in series means a reduction in total capacitance (described by Equation 4.7), the addition of equally valued capacitors in parallel has the exact opposite effect:

$$C_{parallel} = C_{j1} + C_{j2} + C_{j3} + C_{j4} + ... + C_{jm} = m \times C_j \tag{4.9}$$

Thus, and examining the LED string from a purely capacitive perspective, one can state that parallel LED strings (higher m number) will result in a higher equivalent capacitance. This capacitance change holds true for LEDs both with and without ESD device, as it is observed in Figure 4.35.

SPICE simulation results for n-sized LED strings, with m strings in parallel are presented in Figure 4.36. The striking deduction one can make from it is that, despite parallel strings having larger equivalent capacitances, its increase in value is of reduced effect. Firstly, because at V_{BIAS}, there is no much difference in equivalent capacitance, regardless of the strings being in parallel or not (refer to Figure 4.35). Secondly, the fact that by having m light-generated current sources, compensates any additional capacitance that may exist. Whereas having a string

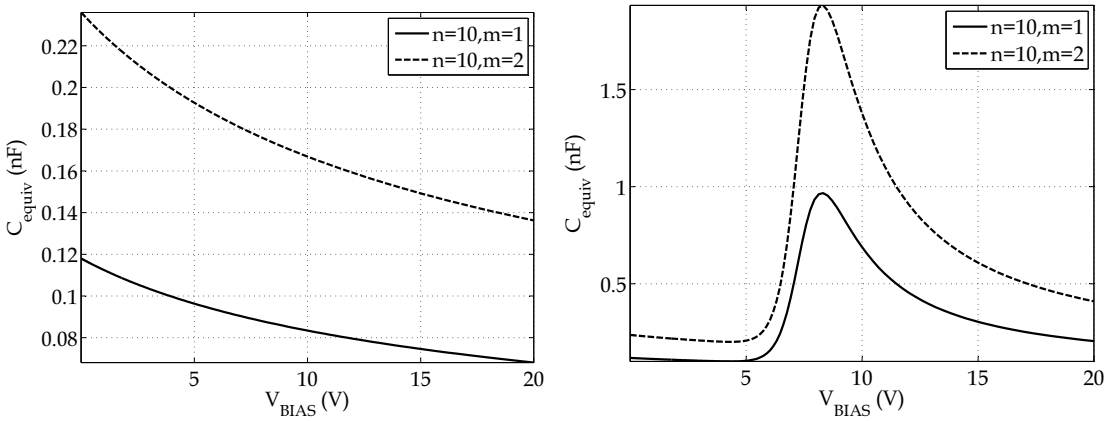

(a) without ESD (b) with ESD

Figure 4.35: V_{BIAS} vs $C_{equivalent}$ plot obtained from SPICE simulation for LED strings of variable size n and m (with and without ESD device).

of n LEDs results in a light-generated current source of value I_{gl}, having m parallel strings results in a light-generated current source of value $I_{gl} \times m$. Both the (small) increase in capacitance and in light-generated current can be confirmed by Figure 4.36 - in periods of light ($I_{gl} > 0$), the capacitance is discharged to a lower level, and in both periods of light and no light ($I_{gl} > 0$ and $I_{gl} = 0$) a slower discharge is always perceived.

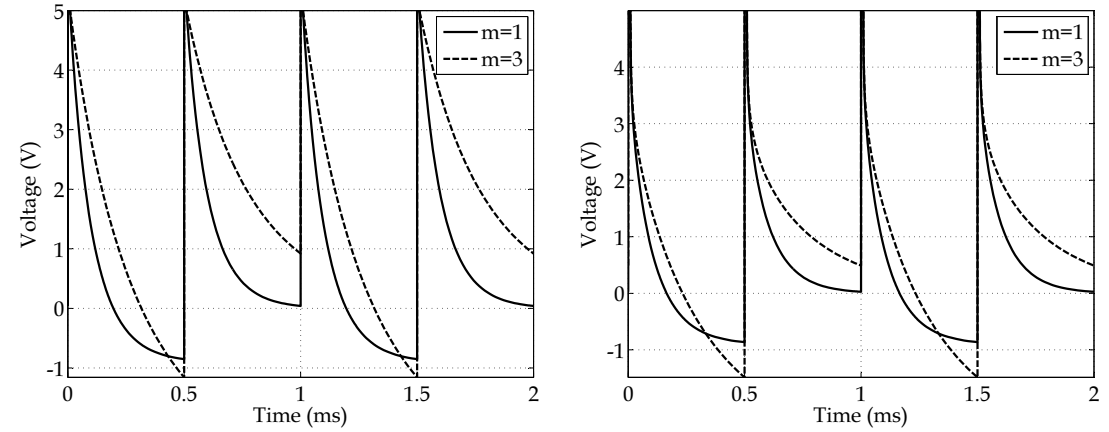

(a) without ESD (b) with ESD

Figure 4.36: Waveforms for LED string of variable size m (with and without ESD device).

Concluding, either series or parallel LED configurations add to the LEDs behaviour as a sensor. Using a string of n LEDs in series decreases overall capacitance, useful in a system where speed is chief. However, if the main goal is light sensitivity - measuring small variations in light, or having a broad light output range - an array of m LEDs in parallel is recommendable. Using m-by-n arrays of LEDs permits both benefits - increased sensitivity at higher speeds. Figure 4.37 depicts the difference between a single LED and a 10-by-10 LED matrix when used as sensors. Note that the LED matrix not only features significantly larger light distinction, it also has a faster decay curve, allowing for shorter periods. Charge time and symbol period were reduced to 1 μs and 10 μs respectively, substantially increasing the system's speed.

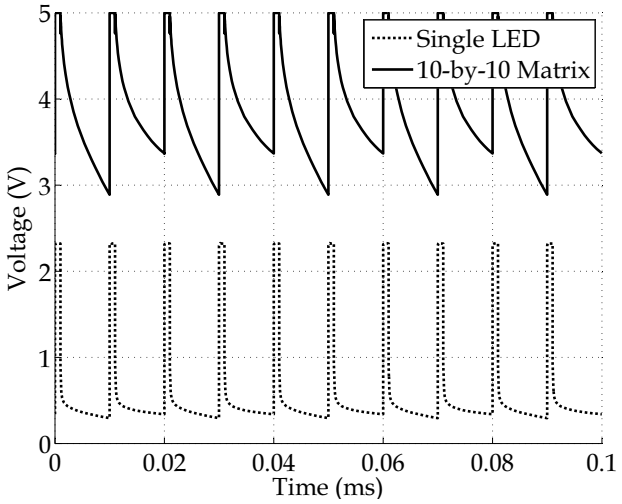

Figure 4.37: Single LED vs 10-by-10 matrix comparison.

This idea should not be limited to standard luminaries, which include dozens of LEDs, but to outdoor luminaries, billboards - which include hundreds to thousands of LEDs - or even displays - which may include up to hundreds of thousands of LEDs.

CHAPTER 5

PROPOSED SYSTEM DESIGN

5.1 System Architecture

Expanding on the concept of Smart Lighting, and given the recent advances in VLC, this work proposes a system that plays part in three distinct processes: illumination, ambient light feedback for dimming and optical communication via VLC. This system can be integrated with similar Smart Lighting systems (via e.g. DALI) and existing communication systems (e.g, a buildings' WiFi, Power Line Communication (PLC), Power over Ethernet (PoE), etc).

The proposed system architecture is shown in Figure 5.1. It comprises three mains building blocks: the LED Driver, the LED string and the μC. The μC unit controls dimming of the LED string, by direct modulation of the LED Driver's PWM input. Dimming and VLC Data information are both managed by the μC unit (although analog dimming of the LED string is still possible). In case of digital transmission, dimming is employed using the dimming methods described in Section 2.2. When not transmitting, the μC may output a lower dimming frequency, or idle, high-frequency patterns for flicker-free operation (also discussed in Section 2.2). Dimming information received by the μC may result of user interaction (via wall-dimmer, external communication, or integrated light level feedback). A simplified timing diagram is provided in Figure 5.2, where non-communication, Tx communication and mixed Tx and Rx communication periods can be observed.

AC-DC and DC-DC conversion blocks are also included. The AC-DC block aims AC-DC conversion from line 220 VAC level to 30-50 VDC for LED Driver

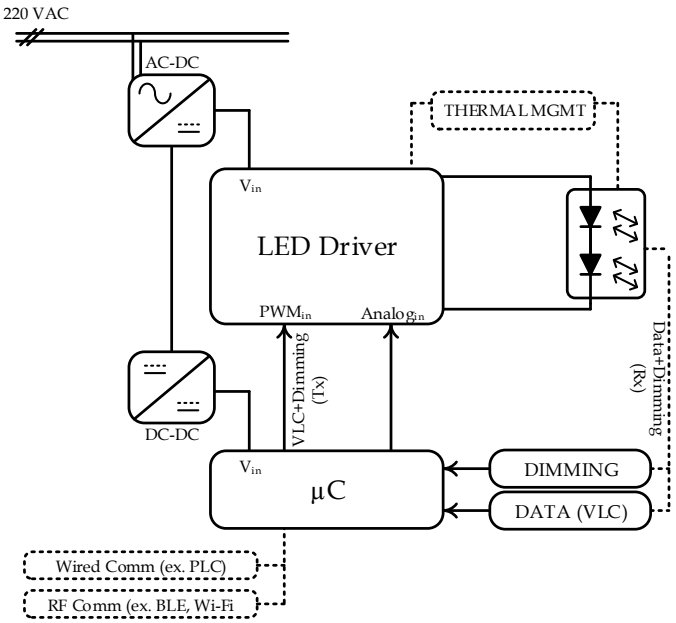

Figure 5.1: Proposed System's Top Level Architecture.

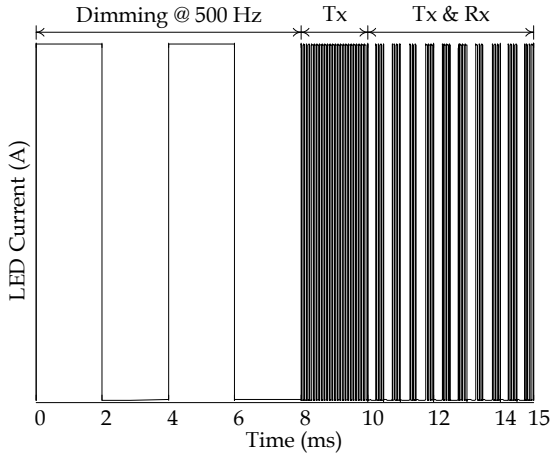

Figure 5.2: Time Diagram of Proposed Architecture.

powering. It comprises an optional isolation (or step-down) transformer, for galvanic isolation, a full-wave rectifier and a DC regulator [13]. Additionally, a Power Factor Correction (PFC) circuit, such as the Valley-Fill circuit may be employed. The DC-DC converter powers the μC. Finally, additional blocks are shown. A thermal management circuit, including a temperature sensor monitors the LED string temperature, and reports to either the μC unit or the LED Driver itself. Should the monitored temperature exceed a defined threshold, LED current is de-rated, or partial/full LED string shutdown is carried out. Extra communication blocks (BLE, PLC or Wi-Fi, PoE) [67, 68, 69] are integrated with local μC, supporting inter-system integration: applications for these extra blocks span from household

communications integration - such as Internet, phone line or TV - to basic user interaction (via portable devices). Lastly, a data path between LED String and the μC unit is provided. This may be for data reception - via a LED-as-sensor, or a photodiode - or simple luminous intensity feedback. Optical receiver is not specified. It can be accomplished via a e.g. photodiode, phototransistor, CMOS image sensor, or by the reverse biased LED string.

5.2 LED String

The LED String takes one of the main roles in the proposed system. Not only does it have the usual purpose of illumination, it also doubles as a light based data transmitter.

Firstly, it is important to define the desired load as early as possible in the design stage, for proper LED Driver design. As a load for the LED Driver, its maximum ratings settled on $V_{load} = 35$ V and $I_{load} = 1$ A. This allows the use of a series of 10 OSRAM *Golden Dragon Plus* LUW-W5AM LEDs [14] operating at $V_F = 3.5$ V and $I_F = 800$ mA each, with maximum output (electrical) power of 28 W. The LUW-W5AM is a small-size high-brightness ThinGan LED, housed in a white SMT package with a clear silicone package. It features Chip Level Conversion (CLC), as a phosphor layer is placed on top of the LED chip, as opposed to being diffused into the molding material, resulting in better colour homogeneity, high luminance and less colour variation over angle. The LUW-W5AM has a large viewing angle at 50% of 170º. The chosen version has a colour temperature of 6000 K (bright white) and its chromaticity coordinates [1] are Cx = 0.32,Cy = 0.33, with CRI values above 80. Also, the LED chip is mounted on an internal heatsink, guaranteeing good heat dissipation, with a maximum thermal resistance of 11 K/W. All 10 LEDs were connected in series, in 5x2 array fashion, fixed to flat heatsink. These LEDs' application range spans from reading lamps, to architectural and street lighting. Referring to Figure 5.3, and keeping in mind that $\Phi_v(350\,\text{mA}) = 124$ Lumen (lm), [14], the luminous flux calculation is shown in Equation (5.1). Total LED string luminous flux adds up to 2170 lm. Taking into account that power dissipation for each LED is given by $P_D = V_F \times I_F$, luminous efficacy is described in Equation (5.2).

$$\frac{\Phi_v(800\text{mA})}{\Phi_v(350\text{mA})} = 1.75 \Leftrightarrow \Phi_v(800\text{mA}) = 1.75 \times 124\,\text{lm} = 217\,\text{lm} \tag{5.1}$$

$$\text{Luminous Efficacy} = \frac{\Phi_v(800\text{mA})}{V_F \times I_F} = \frac{217\,\text{lm}}{3.5\,\text{V} \times 800\,\text{mA}} = 77.5\,\text{lm/W} \tag{5.2}$$

[1] according to CIE 1931 [12]

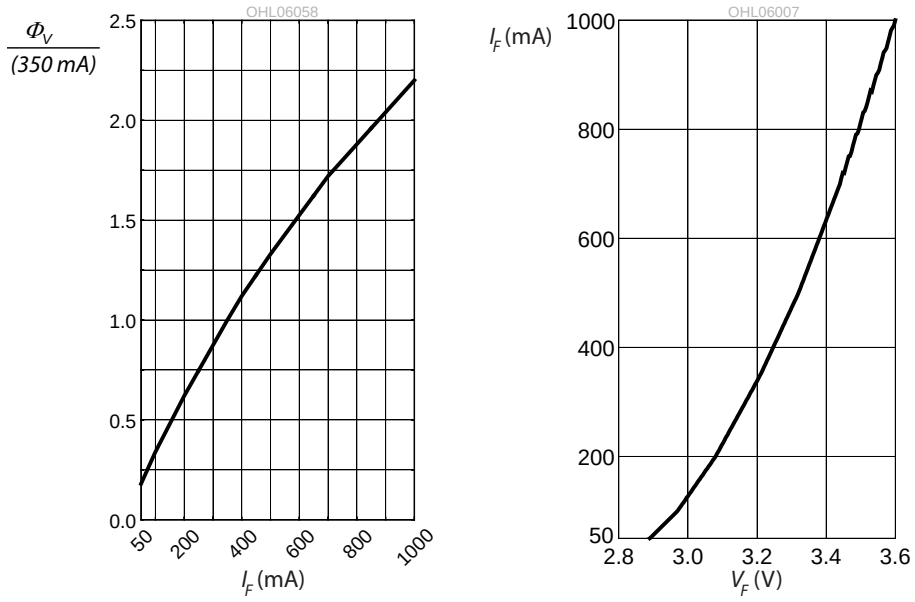

(a) $I_F / \frac{\Phi V}{\Phi V(350mA)}$ curve

(b) I_F / V_F curve

Figure 5.3: OSRAM LUW-W5AM $I_F / \frac{\Phi V}{\Phi V(350mA)}$ and I_F / V_F curves.

5.3 LED Driver

Having in mind the considerations from Section 3.3, the choice of an off-the-shelf LED driver has to meet certain criteria.

- The ability to use external PWM dimming, in addition to analog dimming - this way LED current can be easily controlled via a PWM signal.
- Fast LED current response has to be assured - LED dimming response must not only cover typical dimming frequencies used for light dimming (<20 kHz), it must also cover higher dimming frequencies, suited for VLC applications (>200 kHz).
- Power output range must be as wide as possible, without compromising efficiency. While most VLC implementations in the literature use single LED loads, with simplified drivers, the proposed system goals medium to high power applications, with high efficiency figures.

The proposed LED Driver was based on the LT3763 IC from Linear Technologies [70]. It achieves very fast dimming due to external, series PWM dimming, and efficiency figures are above 95% for a vast load current range. It spans a wide variety of applications, including High Power Architectural Lighting, Automotive

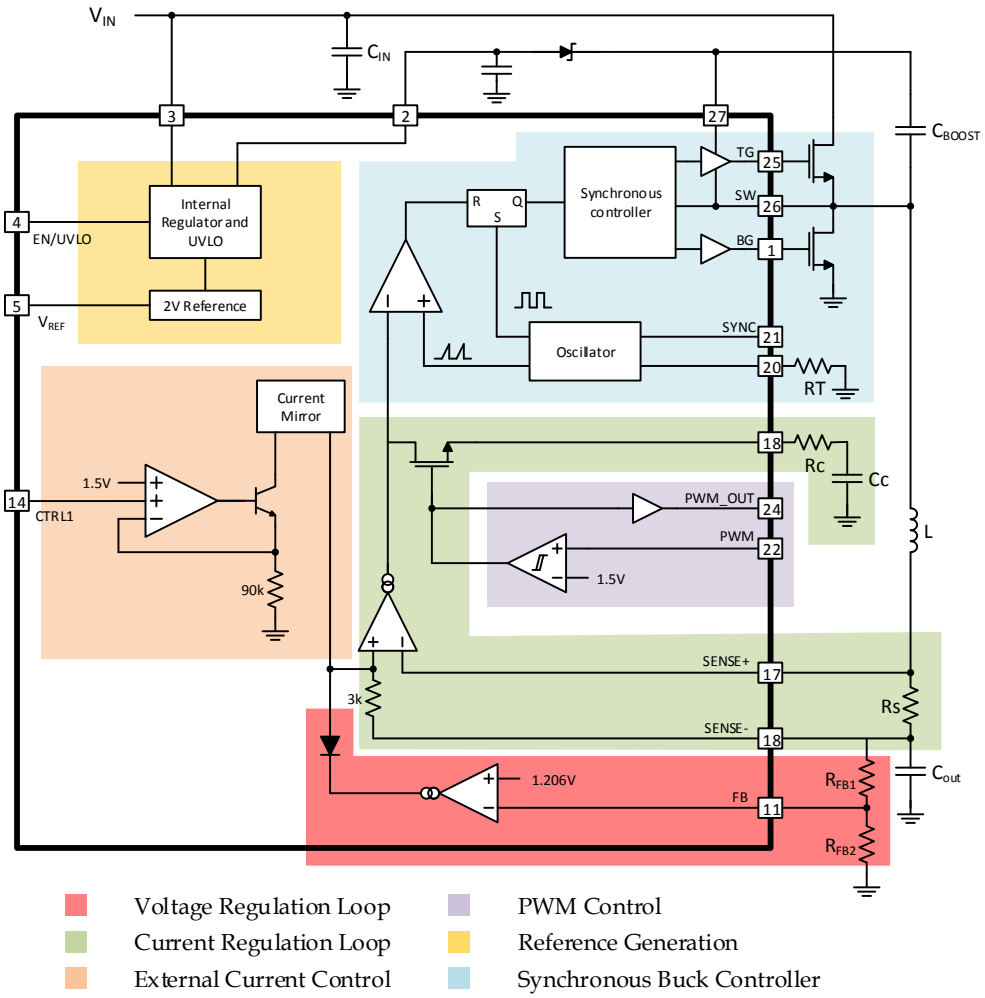

Figure 5.4: LT3763 Block Diagram.

Lighting, Strobe Light and Laser Diodes design. The LT3763 is a fixed frequency, synchronous buck DC-DC driver controller, and features output current regulation up to 20 A with $\pm 6\%$ accuracy, via average current-mode control over an output voltage range from 0 V to 55 V, regulated with $\pm 1.5\%$ accuracy. Internal frequency is programmable from 200 kHz to 1 MHz. It uses an average-current loop control for current regulation and an additional voltage loop control for voltage regulation [70]. PWM Dimming-wise, it uses a combination of both Enable Dimming (switching is terminated when PWM is LOW) and Series Dimming (via external transistor). From Figure 5.4 the synchronous controller and SR latch, the local oscillator, the external switching MOSFETs and current regulation loop transconductance amplifiers are easily identified. A more detailed analysis of its block diagram is available in Appendix D.

The operation of the LT3763 is supported by three major blocks - the PWM Comparator, the Buck Regulator and the Current Regulation Loop. The Buck Regulator comprises all switching MOSFETs and the LC output filter. The Current Regulation loop along with the PWM comparator form the negative feedback loop. Both output voltage and current, are sensed and a control voltage V_c is produced by the regulation loop. The PWM comparator, in its turn, produces a variable duty-cycle internal PWM signal, proportional to the control voltage V_c, which defines the on and off times of the external switching MOSFETs. While the aforementioned blocks are common to any Buck regulator, some details are intrinsic to the circuit itself, mainly the control loop which deserves specific attention, and is further dissected below.

5.3.1 Simulink Model

The operation of the LT3763 can be described and simulated by the developed Simulink[2] model in Figure 5.5. A detailed block diagram of the PWM Comparator is shown in Figure 5.6. This model permits an easy grasp of the internal circuit's operation, and speeds up otherwise exhausting parameter sweep simulations. Internal component parameter values are present in Table 5.1.

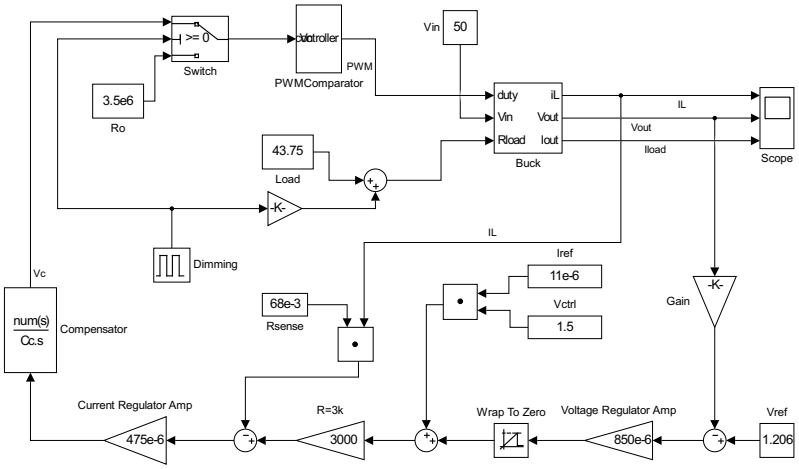

Figure 5.5: LT3763 Simulink Model.

Control Regulation Loop is modelled after the LT3763's Block Diagram in Figure 5.4, and signal flow is as follows (refer to Figure 5.4). Output voltage is attenuated and subtracted from an internal 1.2 V voltage reference. This difference is then converted into a current by a Voltage Regulator Amp (Figure 5.4), often

[2]Simulink is a MATLAB® extension, by MathWorks®

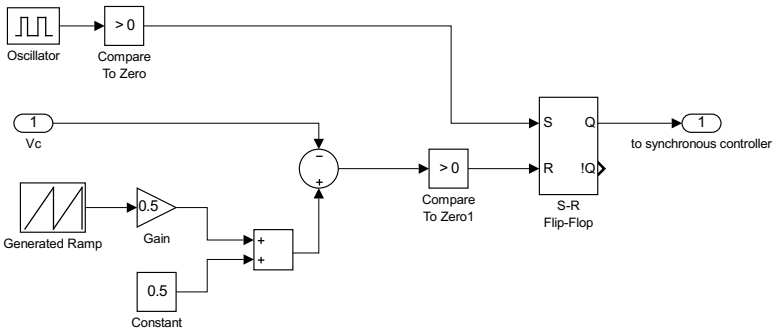

Figure 5.6: LT3763's PWM Comparator Simulink Model.

Table 5.1: Internal Component Parameters.

Voltage Regulator Amp Reference	$V_{ref} = 1.206$ V
Voltage Regulator Amp Transconductance	$g_m = 850\ \mu$A/V
Current Regulator Amp Transconductance	$g_m = 475\ \mu$A/V
Current Regulator Amp Output Impedance	$Z_{out} = 3.5\ M\Omega$
Current Mirror Reference Current	$I_{ref} = 11\ \mu$A
Max. CTRL1 value	$V_{ctrl} = 1.5$ V

described as Voltage Error amp in the literature. The Wrap To Zero block models the series diode, which only permits the amp to work as a current sink. The output of the Voltage Regulator amp subtracts to the internal current reference that, in its turn, feeds into the Current Regulation Amp. The Current Regulation Amp measures the voltage across R_{sense}, proportional to inductor current (whose average value is the output current), and its output current is converted to a voltage V_c by a pole-network, before feeding into the PWM comparator. The latter is comprised of a comparator, which compares the V_c value from the feedback loop with a fixed frequency voltage ramp. This comparator's output resets an internal SR latch that interrupts buck regulator switching. In essence, the current loop can be described by Equations in (5.3) and (5.4): a voltage proportional to output current ($I_L \times R_{sense}$) is summed with an internal voltage reference (V_{ref}) - which is limited by the output of the Voltage Regulator amp (g_{m_V})) - and is converted into a current (I_c) by a transconductance amp (g_{m_A}). Before being compared with the fixed voltage ramp, I_c is converted into a voltage V_c and compensated by a pole-zero network.

$$I_c = g_{m_A} \times \left((I_L \times R_{sense}) + V_{ref} \right) \tag{5.3}$$

$$V_{ref} = 3k\Omega \times (11\mu A/V \times V_{ctrl} - g_{m_V} (1.2 - K \times V_{out})) \tag{5.4}$$

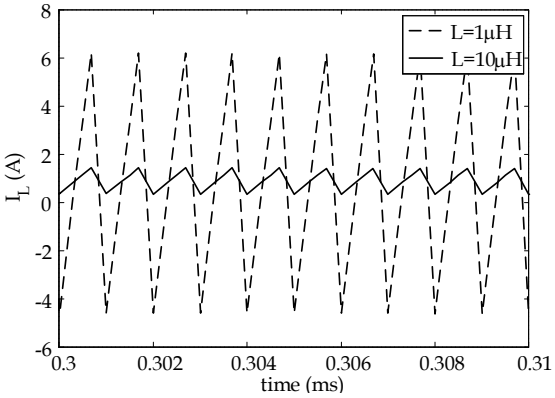

Figure 5.7: Inductor Current Ripple variation using developed Simulink model.

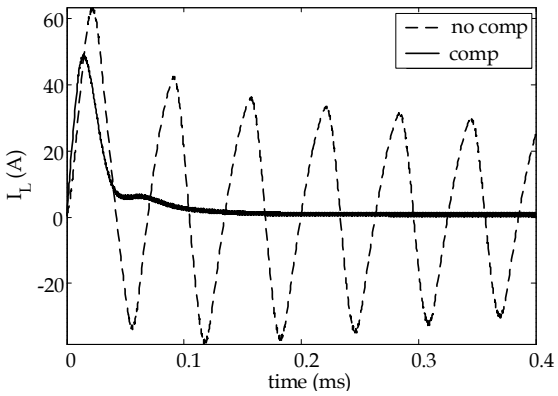

Figure 5.8: Effect of compensation in system's stability using developed Simulink model.

The Simulink model is helpful in the simulation of transient responses, for parameter sizing estimation. For instance, by sweeping inductor L and output capacitor C_{out} values one can observe how inductor or output current ripple is affected by changing either of these parameters. While this is very common in Buck Regulators, and therefore does not justify the use of such a complicated model (any Buck Regulator model would suffice for ripple analysis), an additional parameter, very specific to this circuit, can be investigated - its compensation network. As seen in Section 3.2.2, there are many feedback loop topologies and careful sizing of its compensation network is necessary, due to stability issues. Likewise, the developed model can be used to investigate how parameters such as the $CTRL_n$ voltage and R_{sense} affect the output current. Figure 5.7 illustrates how the inductance L of the inductor alters the inductor ripple. This value, along with the output capacitance value C_{out} form the Buck LC filter, and define the output voltage and current ripple. Figure 5.8 showcases the inductor current waveform for $L = 1\mu H$, with and without proper loop compensation. In accordance with what was previously discussed in Subsection 3.2.2.3, subharmonic instability can be observed.

While a smaller L value will require a higher output capacitance for a given application, increasing it will relax the output capacitance specification. Figure 5.9 depicts the output voltage and current of a stepped load, using $L = 1\ \mu H$. The stepped load emulates LED dimming response, at $f_{PWM} = 500$ kHz. Smaller output capacitances will charge and discharge as the load is turned on and off, whereas higher capacitances maintain steadier output voltage and current. Finally, Figure 5.10 depicts the influence of R_{sense} and V_{ctrl} value on the output current.

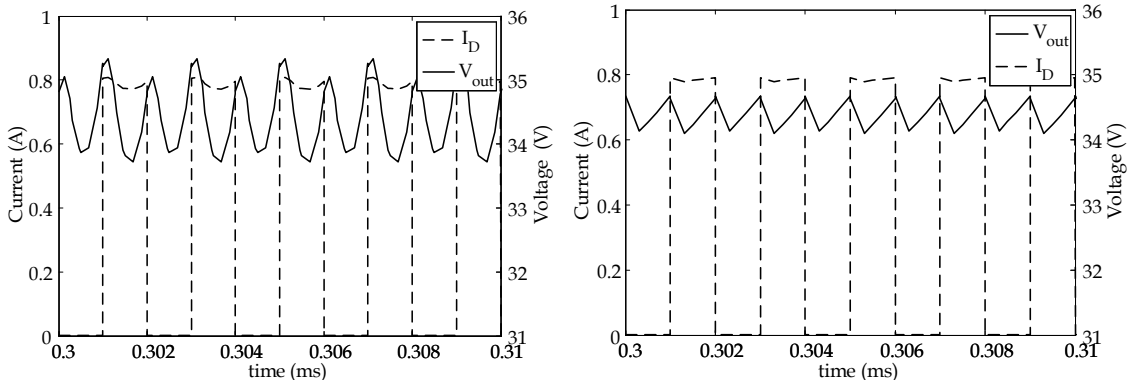

(a) $C_{out} = 1\ \mu F$ (b) $C_{out} = 22\mu F$

Figure 5.9: Effect of output capacitance in output voltage and current using developed Simulink model.

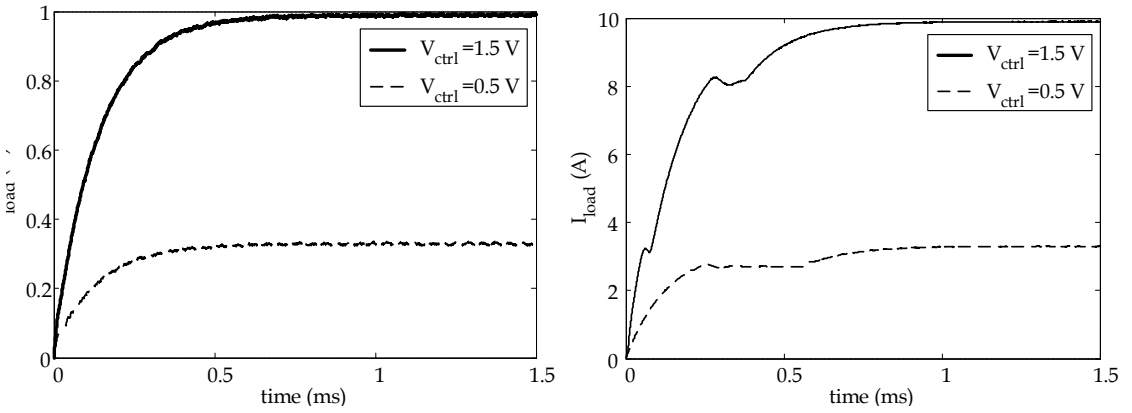

(a) $R_{sense} = 50m\Omega$ (b) $R_{sense} = 5m\Omega$

Figure 5.10: Effect of R_{sense} and V_{ctrl} on output current using developed Simulink model.

5.3.2 Component Sizing

Taking into account the above considerations regarding output capacitance, inductor value and compensation network, and with aid of the LT3763's datasheet [70], the driver was sized as to keep power losses to a minimum, with a maximum rated output of 35 V @ 1 A. Internal switching frequency was set at 1 MHz to enable the fastest current response. Despite the increased power consumption with higher switching frequencies, it is still low when compared to the delivered output power and consequently it has little influence in the driver's efficiency. Input voltage was set to $V_{in} = 50$ V.

Voltage Regulation and Overvoltage Protection

Given the load requirements for output voltage, it is necessary to program the voltage control loop for voltage regulation. This is achieved by sizing the resistor divider from the output to the FB pin, which is referenced at 1.206 V. When output level exceeds the regulated level and FB pin reaches 1.515V, the internal overvoltage flag is set and switching is stopped. In accordance to [70], V_{OUT} calculation is equated below, with Equations (5.5) and (5.6).

$$V_{OUT} = 1.206V \times \left(1 + \frac{R2}{R1}\right) , \tag{5.5}$$

$$\begin{matrix} V_{OUT} = 35V \\ R1 + R2 < 100k\Omega \end{matrix} \begin{cases} R1 = 3.24k\Omega \\ R2 = 90.9k\Omega \, . \end{cases} \tag{5.6}$$

Inductor Selection and Output Capacitor

The recommended inductor peak-to-peak ripple current is 30% of the output current, [70]. Given the input and output voltages, output current, switching frequency and ripple ratio, the inductor L value calculation is rather straightforward [71]. From Table 3.1, Equation (5.7) is rearranged. For a Buck Driver during ON time and establishing ripple ratio as $r = \Delta I / I_{OUT}$ comes Equation (5.8).

$$\text{while } t_{ON} \qquad \frac{dI}{dt} = \frac{V_{in} - V_{out}}{L} \tag{5.7}$$

$$\Delta I = t_{ON} \times \frac{V_{IN} - V_{OUT}}{L} = D \times t_{sw} \times \frac{V_{IN} - V_{OUT}}{L} = \frac{D}{f_{SW}} \times \frac{V_{IN} - V_{OUT}}{L}$$

$$r = \frac{\Delta I}{I_{OUT}} = \frac{(V_{IN} - V_{OUT}) \times D}{L \times f_{SW} \times I_{OUT}} \Leftrightarrow L = \frac{(V_{IN} - V_{OUT}) \times V_{OUT}}{f_{SW} \times I_{OUT} \times r \times V_{IN}} \tag{5.8}$$

For $r = 0.3$, $V_{IN} = 50$ V, $V_{OUT} = 35$ V, $I_{OUT} = 800$ mA and $f_{SW} = 1$ MHz, inductor value L computes $L = 43.75\mu$H. The output capacitor was decided on 2×22 μF, which exceeds the *"minimum of* 20 *µF/A of load current"* recommended in [70].

Average Current Control Loop and R_{Sense} Sizing

The two main inputs CTRL1 and CTRL2 control the current loop. CTRLn voltages are buffered and produce a reference current set by an internal 90 kΩ resistor -

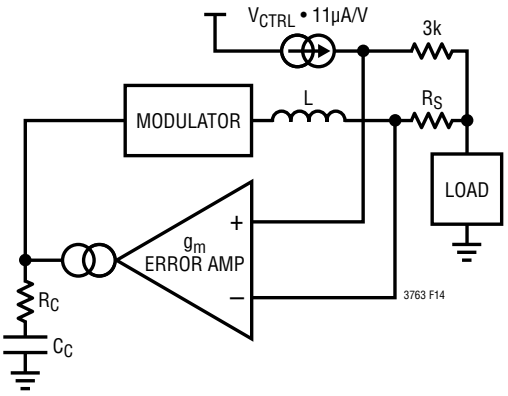

Figure 5.11: LT3763 Average Current Mode Control Scheme (from [70]).

which equates to a equivalent transconductance of 11 μA/V, which is shown in the Average Current Mode Control scheme in Figure 5.11.

The relationship between control voltage V_{CTRL}, R_S and inductor (output) current I_L can be demonstrated by Equation (5.9) and (5.10).

$$V_+ - V_- = (3k\Omega \cdot V_{CTRL} \cdot 11\mu A/V + Sense_-) - Sense_+ \tag{5.9}$$

Taking into account that $V_+ = V_-$ and $Sense_+ - Sense_- = I_L \cdot R_S$,

$$0 = 3k\Omega \cdot V_{CTRL} \cdot 11\mu A/V - I_L \cdot R_S \Leftrightarrow I_L = \frac{1}{30} \cdot \frac{V_{CTRL}}{R_S} \tag{5.10}$$

Given that V_{CTRL} is clamped to 1.5 V, for a maximum output current of $I_{OUT} =$ 1 A, sense resistor is computed as $R_{Sense} = 50\ m\Omega$.

The average-current control loop offers some advantages over peak-current control loop, mainly noise immunity and lack of slope compensation requirement [47, 72, 73]. There is, however, need to limit loop gain in order to avoid subharmonic oscillation. An external pole-zero compensation network converts the current output of the error transconductance amplifier to a voltage which then feeds into the PWM comparator, and serves as the overall loop compensator. Increasing R_c will increase loop gain, and decreasing C_c will shorten the bandwidth. Given it is an average current mode controller, it is required that the slope of the error voltage does not exceed the PWM ramp slope during the switch off time [47]. Hence Equation (5.11), which calculates the maximum down-slope at the current error amp's output. The slope at the amp's output is proportional to $I_L \cdot G_{CA}$ and must, at most, equal the oscillator ramp slope ($V_{ramp} \cdot f_{SW}$). Resistor R_c sets $G_{C_{EA}}$'s value and provides a zero, while capacitor C_c allows for maximum gain at DC caused by its pole. References [72, 73] suggest the use of an extra parallel

capacitor, by adding an extra pole one decade after the crossover frequency, higher frequencies such as switching noise are attenuated while maintaining a phase boost.

$$G_{C_{EA}} \cdot I_L \leq V_{OSC} * f_{SW} \Leftrightarrow G_{C_{EA}} \leq \frac{V_{ramp} \cdot f_{SW} \cdot L}{V_O \cdot R_{Sense}}$$
$$G_{C_{EA}} \leq \frac{1k\Omega \cdot 1\text{V} \cdot L}{V_O \cdot R_{Sense} \cdot t_{SW}} \tag{5.11}$$

After R_c calculation, C_c may be computed so that the zero causes a phase boost at crossover frequency. LT3763's datasheet suggests $C_c = 4.7nF$ as a good starting point, which is coherent with a phase boost around the 10 kHz crossover frequency.

Considering $L = 43.75\mu\text{H}$, $V_{OUT} = 35\text{V}$, $R_{Sense} = 50m\Omega$ and $t_{SW} = 1\mu\text{s}$, $R_c = 25k\Omega$ and $C_c = 2n\text{F}$ are determined.

Switching MOSFETs, Schottky Diode and PWM Driver Selection

The choice of Switching MOSFETs is crucial, as they may be responsible for substantial power losses and may result in significant efficiency degradation. Power losses on MOSFETs may occur on two different fronts: conduction losses and switching losses. Conduction losses result from internal voltage drops across both Top and Bottom MOSFETs.

$$P_{cond(TG)} = I_O^2 \times R_{DS(ON)} \times D \tag{5.12}$$
$$P_{cond\left(D_{flywheel}\right)} = I_O \times V_D \times (1 - D) \tag{5.13}$$

Equation (5.12) and (5.13) describe conduction losses on both the Top Gate MOSFET and the flywheel diode. For a 800 mA output current with a duty ratio of 0.7, $R_{DS(ON)} = 12\ m\Omega$ and $V_D = 0.7$ V, power losses for both MOSFET and diode result in 5.38 mW and 168 mW. The flywheel power losses are significant, and thus synchronous rectification ensues. By replacing the flywheel diode with a similarly low-$R_{DS(ON)}$ MOSFET, efficiency is substantially improved. Conduction power losses for this Bottom MOSFET, with $R_{DS(ON)} = 12\ m\Omega$ are described by Equation (5.14)

$$P_{cond(BG)} = I_O^2 \times R_{DS(ON)} \times (1 - D) \tag{5.14}$$

Using synchronous rectification, Bottom Gate conduction losses result in 2.88 mW.

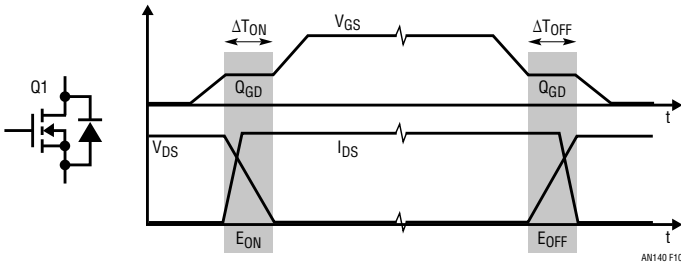

Figure 5.12: Switching Losses on MOSFETs (from [41]).

Switching losses add to the previously discussed conduction losses. These concern the current and voltage overlaps during the turn-on and turn-off transients. With regards to the Top MOSFET, most of its switching losses result from the charging and discharging of parasitic capacitance C_{GD} with Q_{GD}, [41]. Switching losses are the sum of the energy losses during turn-on and turn-off, proportional to switching frequency. Equation (5.15) and Figure 5.12 reflect this.

$$P_{SW} = (E_{ON} + E_{OFF}) \times f_{SW} \tag{5.15}$$

Comparatively, switching losses on the Bottom MOSFET are lower as it turns on after its body diode starts to conduct and turns off before it starts to conduct, [41]. Current and voltage overlap are thus reduced. Additionally, an external Schottky diode parallel to the Bottom Gate can further improve efficiency, provided it has a comparatively lower Reverse Recovery Charge Q_{rr}, [41, 74].

As shown in [70], the total power losses in Top MOSFET can be approximated by Equation (5.16)

$$\begin{aligned} \text{P}_{\text{LOSS}}\text{=ohmic loss + transition loss} \approx \left(\frac{V_O}{V_{IN}} \cdot I_O^2 R_{DS(ON)} \cdot \rho_T\right) + \\ \left(\frac{V_{IN} \cdot I_{OUT}}{5V} \cdot \Big((Q_{GD} + Q_{GS}) \cdot (2 \cdot R_G + R_{PU} + R_{PD}) \Big) \cdot f_{SW}\right) . \end{aligned} \tag{5.16}$$

Another power loss related to the switching MOSFETs selection is the power loss when driving the transistor gates. The total gate charge Q_G of both transistors must be charged and discharged each switching cycle, and is computed by Equation (5.17).

$$\text{P}_{\text{LOSS}} = V_{IN} \cdot \big(Q_{GLG} + Q_{QHG}\big) \cdot f_{SW} \tag{5.17}$$

A good approach is to select MOSFETs with the lowest $R_{DS(ON)}$ and Q_G (total charge gate) possible as to minimize conduction and switching power losses respectively. Considering these criteria, the choice for the switching MOSFETs for both Top and Bottom gates relied on NXP's BUK9Y15-60E which feature on-resistance and total gate charge values of $R_{ds} = 13\ m\Omega$ (@ $V_{GS} = 10$ V) and

$Q_G = 17.2n$ C (@ $V_{GS} = 5$ V) respectively. An external Schottky diode was used, parallel to the Bottom Gate. Also, an external diode was required for C_{BOOST} charging. This diode supplies a 5V reference that charges C_{BOOST} when the high side MOSFET is off. This 5V reference along with C_{BOOST} guarantees full saturation of the internal high side driver, and thus a sufficiently high enough voltage on the high side gate. The choice for both these Schottky diodes relied on the DFLS260 and DFLS160 (Diodes Incorporated) respectively. The chosen PWM Driver was a SSM3K339 (Toshiba).

5.3.3 SPICE Simulation Results

Given that the LT3763's SPICE model is given by Linear Technologies itself, and it is compatible with its proprietary SPICE Simulation software LTSPICE®, one should confidently expect accurate and reliable results.

Variable duty-cycle operation of the internal synchronous controller are evidenced in Figure 5.13. As output voltage increases, so does the duty-cycle. As discussed in the above Section 3.2, output voltage in buck regulators is given by $D = V_{out}/V_{in}$, and the results below show proof of this. The depicted waveform corresponds to the signal applied the Top MOSFET gate.

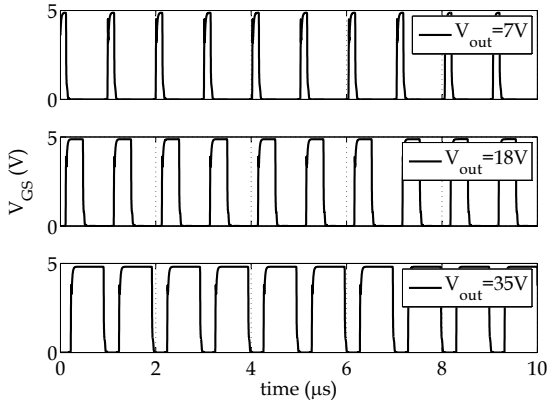

Figure 5.13: Top MOSFET gate signal duty-cycle variation for $V_{in} = 50$ V.

Although an SMPS in nature, the LT3763 is optimized for use with LED loads, and is is thus important to observe not only the duty-cycle ratio between input and output voltages, but also load current and inductor waveforms with and without LED dimming. Figure 5.14a shows the SPICE simulation results of the LT3763-based LED Driver, with the component sizing aforementioned, for inductor current I_L, load (LED) current I_D and output voltage. Specific SPICE models were used for switching transistors, Schottky diodes, PWM driver and LED. Current ripple is approximately 30%, which satisfies the datasheet's recommendation, and average

LED current and output voltage are very close to the desired values - 800 mA and 35 V respectively. On the other hand, Figure 5.14b results show that output current and voltage are approximately 200 mA and 29.7 V respectively. This is due to the effect of internal circuitry, that was not modelled in the Simulink model, such as the C/10 comparator and PWM-dependent switching shutdown. Two different, although related, phenomena occur. Firstly, when the PWM signal is LOW, a NMOS switch disconnects V_c from the current regulation amplifier's output, causing the SR latch to reset - thus, switching is stopped, until PWM signal is HIGH again. This is reminiscent of Enable Dimming, discussed in Subsection 3.2.3. This automatically relates PWM frequency and internal switching frequency - the driver is effectively working at a frequency of 500 kHz, and due to the inductor's value, its current ramp is not as steep as it is necessary for the driver to produce the desired output.

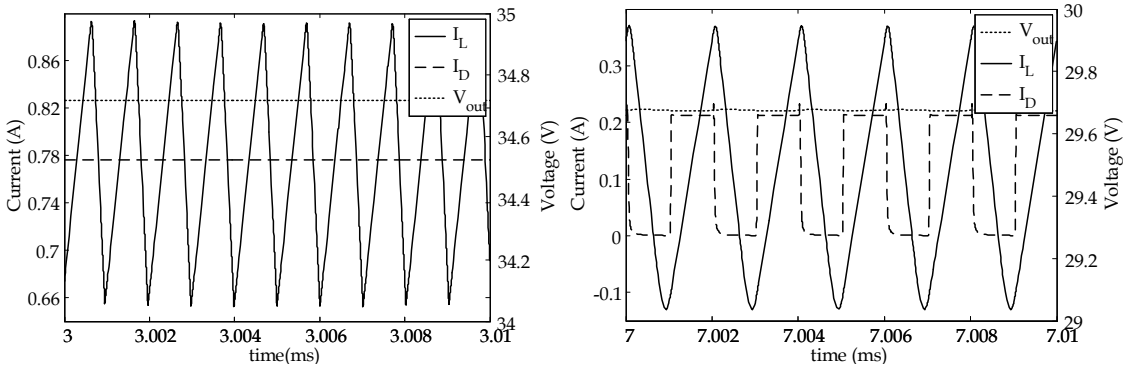

(a) No Dimming (b) 50% Dimming at $f_{PWM} = 500$ kHz

Figure 5.14: Proposed Driver's V_{out}, I_L and I_D waveforms.

A faster inductor current response is desired, and therefore a lower inductance value must be used. This will not allow, however, for the driver to operate at its set internal switching frequency, due to C/10 comparator's effect. This comparator causes the low side gate driver to shutdown when inductor current decreases to 10% of the maximum current, turning the regulator into non-synchronous, discontinuous conduction mode operation. Notwithstanding, the desired output is achieved, despite the higher than specified inductor current ripple. For a inductor value of $L = 4.7\ \mu$H, R_c must be recomputed to $R_c = 2.69\ k\Omega$. Figure 5.15 depicts this case where series 50% dimming is employed at $f_{PWM} = 500$ kHz.

Alternatively, different PWM dimming methods are possible. Firstly, by driving the PWM MOSFET directly with the PWM signal, while pulling the LT3763 PWM_{IN} high. This will prevent switching from terminating when PWM is LOW. Secondly, by using parallel dimming. By employing no output capacitance, the regulator

works as a current source - the inductor current drives the load directly when PWM is HIGH, and is shunt to ground when PWM is LOW. By using a higher inductance value (L=4.7 mH), inductor current ripple is minimized, thus lowering load current ripple when PWM is HIGH. This permits the highest switching frequencies. The latter method improves on the first one, and is preferred. Regarding the first method, as load current (and therefore inductor current) drops to zero when PWM is LOW, the internal C/10 comparator shuts down switching, which brings delay and rise time delays into the equation when PWM is turned back on. Although this is does not occur at high dimming frequencies, it is very noticeable at lower dimming frequencies. This method's response is shown in Figure 5.16, using series 50% dimming at $f_{PWM} = 500$ kHz.

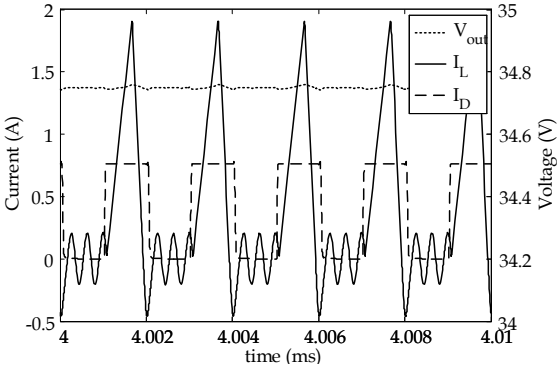

Figure 5.15: Resized Driver's waveforms (with Series Dimming).

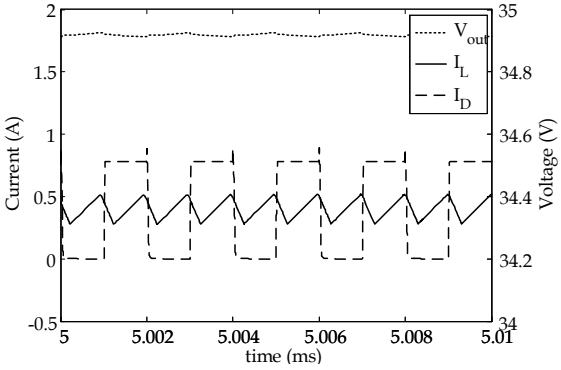

Figure 5.16: Resized Driver's waveforms (with alternate Series Dimming).

In the latter dimming method, as the inductor current is always constant (current either flows continuously through load or PWM Driver) it is constantly regulated, and the internal C/10 comparator is kept from shutting down the internal switching, improving the response times for lower frequencies. Due to a higher valued inductor, which allowed smaller ripple, internal switching frequency was relaxed to 200 kHz - reducing internal power consumption - and loop compensation was adequately recomputed to $R_c = 413\ k\Omega$ and $C_c = 38\ pF$. Using parallel PWM dimming and enable constant operation of internal switching requires special attention to both control loops. Due to lack of output capacitance, the voltage loop has a secondary importance, as output voltage is anything but continuous. Voltage divider resistors at its input should be sized as to not limit the V_f / I_f operating point of the LED string, and R_{sense} should be sized to limit output current. This method's results are pictured in Figure 5.17, with parallel 50% dimming at f_{PWM}=2 MHz. All three methods present good results, as pictured in the Figures 5.15 to 5.17, which show output voltage and inductor and LED current

waveforms. Series and parallel dimming allow for a maximum of 500 kHz and 1 MHz PWM dimming frequencies, respectively.

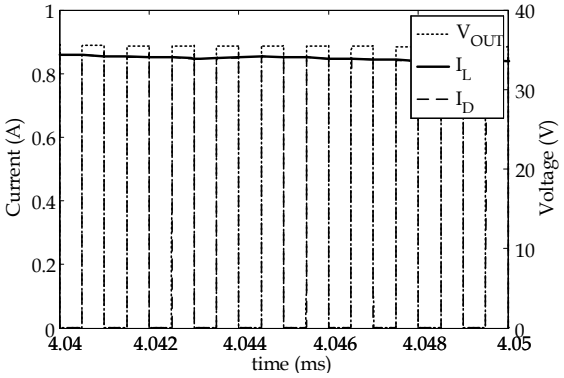

Figure 5.17: Resized Driver's waveforms (with Parallel Dimming).

Regarding efficiency both dimming methods provide favourable results. Figure 5.18, shows efficiency results[3] for variable PWM Dimming Duty Cycle, using the aforementioned PWM frequencies of $f_{PWM} = 500$ kHz and $f_{PWM} = 2$ MHz, respectively. Maximum efficiency is 94.6% using parallel dimming (duty-cycle of 1) and 91.6% using series dimming (duty-cycle of 0.5). At 50% dimming, using the parallel dimming method yields 88.9% efficiency. Due to the fact that the series dimming method uses the internal PWM driver, internal switching is terminated when PWM is low, and therefore result in higher efficiency throughout the dimming range (ie. duty cycle variation), [70]. Provided that the inductor value is low enough, fast LED current response to PWM signals is assured, [75]. It should be noted however, that for the aforementioned inductor and output capacitance sizing ($L = 4.7$ μH and $C_{out} = 44$ μF), output voltage drops to 34.5 V and 32.1 V in dimming levels of 25% and 10% respectively. On the other hand, using the parallel dimming method only allows >90% efficiency figures for dimming levels higher than 50%. Since the PWM signal actuates on the PWM MOSFET itself, bypassing the internal PWM driver, switching is kept from terminating. While this allows fast response throughout the dimming range, it results in lower efficiencies for lower dimming levels, as the generated power - which is constant, due to constant internal operation - is shunt to ground via the PWM driver.

For higher dimming levels, efficiency using the parallel dimming method does, in fact, surpass that of the series dimming method, as seen in Figure 5.18. This occurs due to extra internal power losses that result from turning on and off of internal switching in the series dimming method, keeping in mind that the internal frequency is 5x higher when using the series dimming method -

[3]Efficiency is obtained by computing the ratio between output and input power, $\rho = \frac{P_{OUT}}{P_{IN}}$

$f_{SW} = 1$ MHz, as opposed to $f_{SW} = 200$ kHz if using parallel dimming. Figure 5.19 depicts power losses distribution for both series and parallel dimming, with duty-cycle of 0.9 - output power is 25.2 W in both cases. Referring to Figure 5.19a, 78% of the total power losses P_{loss} using series dimming result from internal power dissipation. When using parallel dimming, major power losses result from internal and PWM MOSFET power dissipation, as seen in Figure 5.19b. The increase in PWM MOSFET power dissipation can be explained by the increased switching frequency ($f_{PWM} = 2$ MHz as opposed to $f_{PWM} = 500$ kHz if using series dimming). Additionally, the increased series resistance from the higher value inductor also degrades the system's efficiency, representing 40% of total power losses.

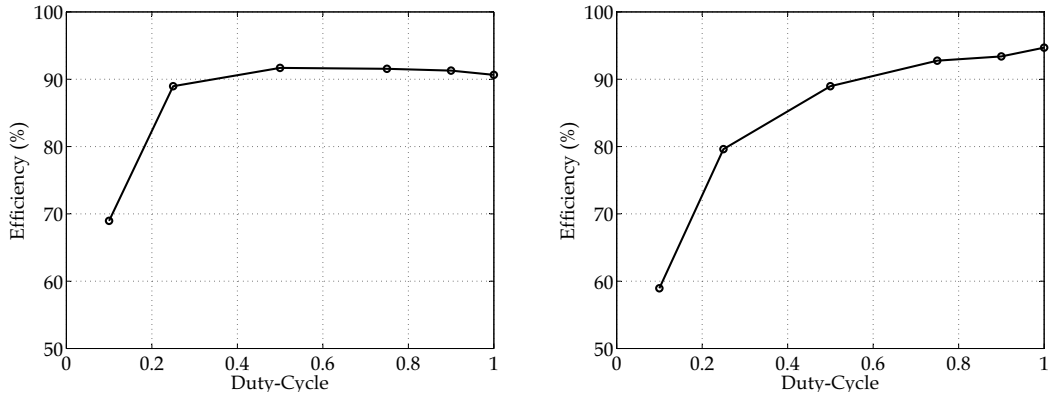

(a) Series Dimming (b) Parallel Dimming

Figure 5.18: Proposed Driver Efficiency with both Series and Parallel Dimming.

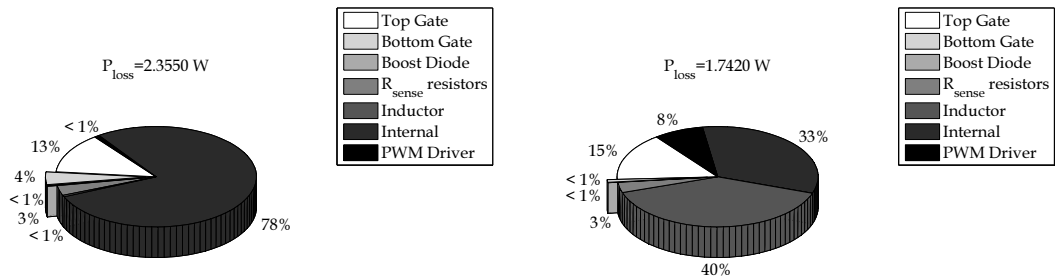

(a) Series Dimming (b) Parallel Dimming

Figure 5.19: Distribution of Proposed Driver Power Losses with both Series and Parallel Dimming.

5.4 Remaining Blocks and Further Expansion

5.4.1 AC-DC and DC-DC conversion blocks

The remaining blocks comprise the AC-DC and DC-DC conversion from line to both LED Driver μC unit. A general discussion of these conversion blocks is given below, as the scope of this topic is beyond this thesis. Powering of the LED Driver is often accomplish via rectification of line AC voltage, subsequent filtering, and DC-DC conversion via a linear regulator, or a switching regulator. The use of a PFC circuit is required, for both power factor correction and harmonic reduction. The IEC EN 61000-3-2 standard specifies maximum permissible harmonic content up to a n=39 >25W Class C equipment (lighting equipment), [76, 77]. Harmonic content and power factor can be improved by correct input current filtering, [76, 77]. Figure 5.20 shows the common signal flow in AC-DC conversion.

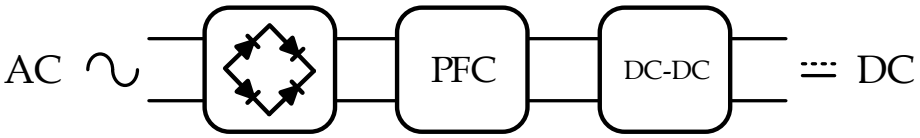

Figure 5.20: AC-DC Conversion Signal Flow.

However, the $V_{in} = 50$V input of the proposed system anticipates its integration in a LVDC power grid (or DC Microgrid), or even a PoE grid [78].

The majority of household appliances use internal AC-DC conversion, converting the line's AC into a lower DC voltage: TVs, Hi-Fi sets, Computers, Internet Modems and Routers all operate on DC power, and being DC native loads, it makes sense to power them directly with a DC source, rather than having a dedicated AC-DC for each of them. Moreover, with the advent of battery powered devices (which require charging), such as smartphones, tablets and even electric cars, and also solar panels for power generation and SSL lighting, an all-DC power grid is a perfectly feasible idea. Granted, AC loads are still present in the household, but many of those employ variable-speed motor drivers, which already require a DC voltage for variable AC frequency generation - it would be straightforward to power those loads from a DC source, [79, 80, 81, 82]. In fact, both PoE and LVDC lines resemble the -48V lines used in the telecom industry. The IEEE 802.3af and 802.3at versions describe the standardization of PoE networks, and foresees loads up to 57 VDC at 60 W, [83, 84]. On the other hand, the first standards for LVDC grids are starting to emerge at 24 VDC and 380 VDC, by E-Merge Alliance [4],

[4]E-Merge Alliance is an open industry association of nearly 80 members leading the rapid

although similar 12 VDC and 48 VDC may surface in the future. There are already 4 running LVDC installations in the USA (including Intel and IBM), over 20 in Europe (including France Telecom and European Telecom), and more than 1000 in China alone.

Having this in mind, it should be noted that the proposed driver permits vast input range without significant efficiency degradation, and is compatible with both AC and LVDC/PoE power grids as exemplified in Figure 5.21. Finally, an extra DC-DC converter is required for μC powering. Due to the low power requirements of most μC units, a simple buck switching regulator should supply adequate power to said load, with high efficiency.

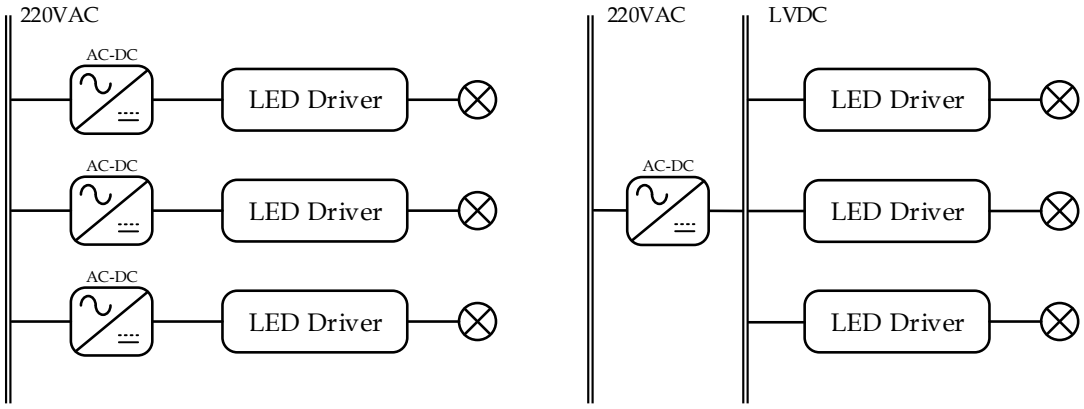

(a) Conventional AC Power Grid

(b) LVDC Power Grid

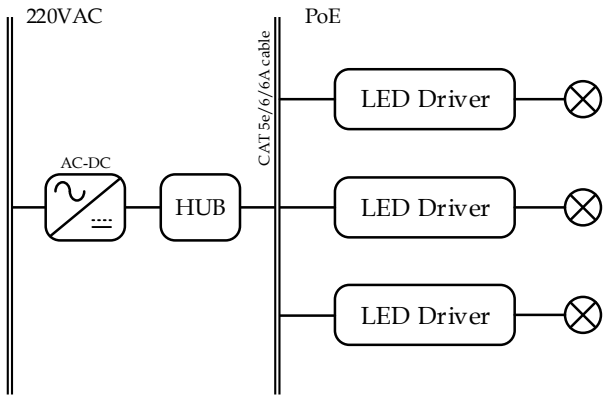

(c) PoE Power Grid

Figure 5.21: AC, LVDC and PoE Power Grids for LED Lighting Systems.

adoption of safe DC power distribution. E-Merge members include GE Energy, Intel Corporation, among others

5.4.2 System Expansion

The Proposed System foresees WDM and CSK modulation, and thus supports further expansion into a RGB luminary. By using three differently coloured LEDs, data-rate is increased as three distinct communication channels are formed, provided that the receiver employs wavelength selective photodetectors, such as LED-as-sensors (as per Chapter 4). LED Driver implementation may occur in two distinct ways, depicted in Figure 5.22. Each LED has its own Driver, which receives unique PWM signal, which may contain both VLC and Dimming data (Fig. 5.22a); alternatively, the system is comprised of a single, three-channel LED Driver, which receives VLC and Dimming data for all three RGB channels (Fig. 5.22b). While the latter method will allow for simpler and a higher density system, it may lack in both speed and power handling. Nevertheless, a three-channel LED driver may be suitable for RGB VLC communication, provided that high data-rates are not intended.

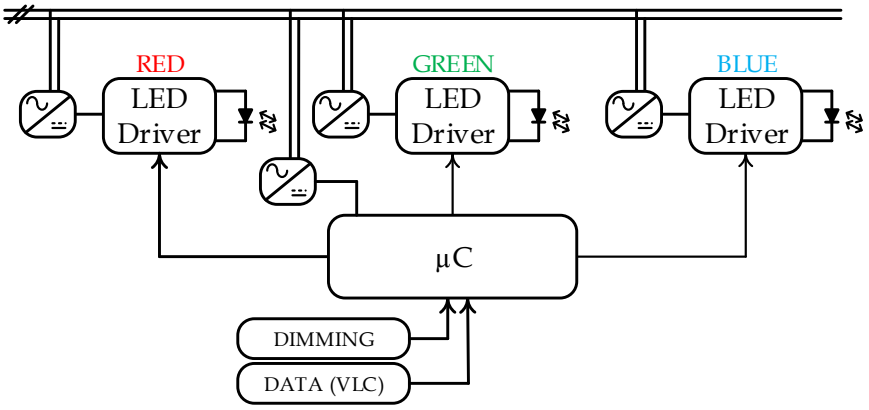

(a) Three Single-Channel Drivers

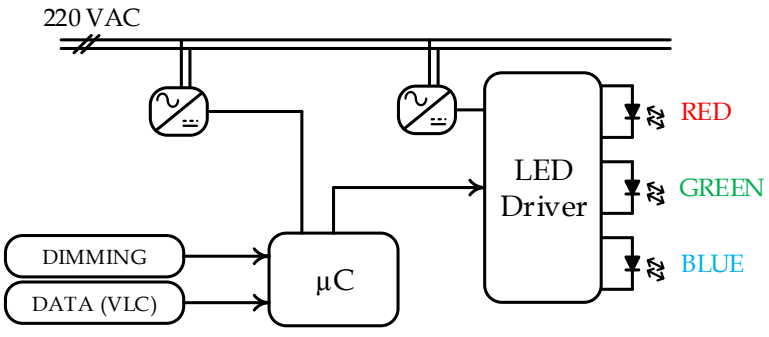

(b) Single Three-Channel Driver

Figure 5.22: Proposed system expansion with RGB Implementation.

The LT3597 by Linear Technology is a 60 V Triple Step-Down LED Driver, capable a maximum of 100 mA output current per channel. It is housed in a

QFN 0.4 cm^2, and due to lack of external switching it allows for very dense implementation, with reduced number of external components. This driver is a very good candidate for medium data-rate RGB VLC communication. Figure 5.23 depicts current waveforms for all three channels, with dimming levels of 50%, 60% and 80% for the Red, Green and Blue channels respectively. Maximum optical clock is 200kHz for each channel, which using OOK and Manchester Coding could translate into a total data-rate of 600 kb/s. Dimming methods for VLC PHY III communication are restricted to the analog domain, via forward current adjustment, as changing symbol duty-cycle will result in resultant colour shifts. Therefore, even though each channel is pictured with different dimming levels in Figure 5.23, it is merely for illustrative and curve distinction.

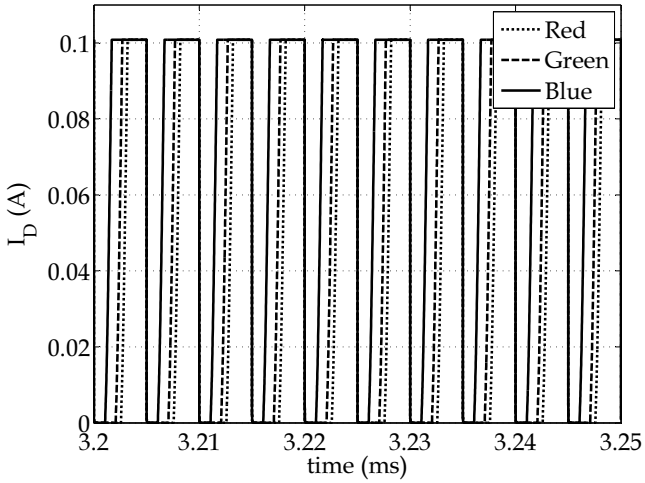

Figure 5.23: LT3597's I_D waveforms from three RGB channels, obtained from SPICE simulation.

CHAPTER 6

SYSTEM IMPLEMENTATION AND EXPERIMENT EVALUATION

6.1 Circuit Board Design

6.1.1 Special Considerations

The final step of the LT3763-based LED Driver implementation focuses on its circuit board design. A good layout design is essential in all circuits, but it is especially important in switching regulators - it optimizes supply efficiency, alleviates thermal stress, and minimizes inter-mesh noise. Two different current types can be identified in any switching regulator - *AC* and *DC* current. The main difference between these is the presence and lack, respectively, of hard transients, [85, 86]. Figure 6.1 distinguishes both continuous and pulsed currents.

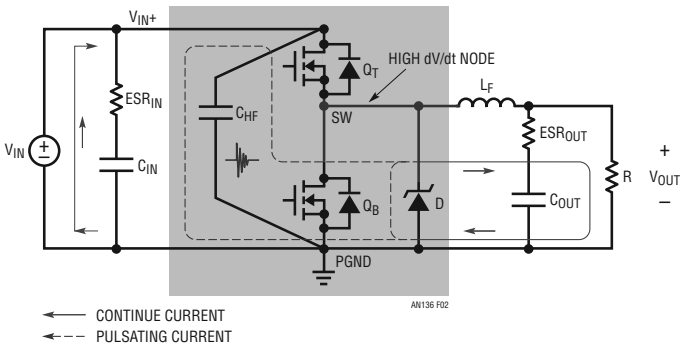

Figure 6.1: DC and AC current paths of a Synchronous Buck Regulator (from [85]).

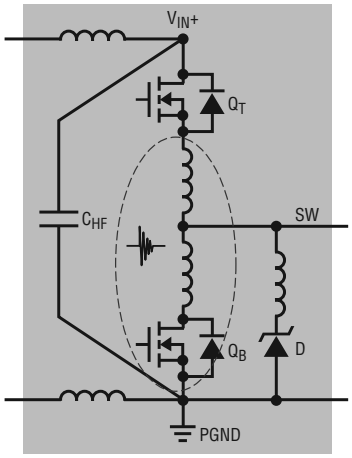

Figure 6.2: Parasitic Inductance in high dI/dt loop area (from [85]).

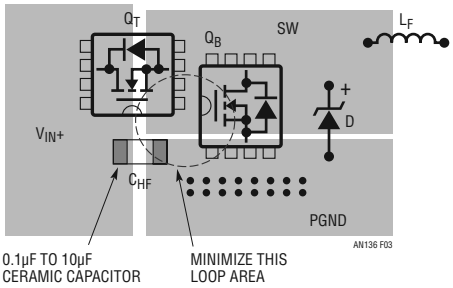

Figure 6.3: dI/dt loop layout example (from [85]).

The solid line represents the continuous current paths (where the harmonic content is lower) which includes the input capacitor as well as the output capacitor and load - which, by being in series with the inductor, *resist* current changes. On the other hand, the dashed represents the dI/dt current paths, which carry the heavy switched, hard transient currents. These encompass the top and bottom gate MOSFETs, the input decoupling capacitor and the parallel flywheel diode, [85, 86]. The reason behind why special importance must be given to this dI/dt node lies on the parasitic inductive properties of PCB traces (Figure 6.2). A current flow dI/dt through an inductor L forms a voltage V that equals $V = L \times dI/dt$. For continuous current paths, where dI/dt is low, the induced voltage is irrelevant whereas in AC current paths, with high dI/dt, it can be problematic. In fact, taking in consideration the thumb-rule described in [86], a 1 A, 30 ns current transient in a one-inch copper trace produces an induced voltage of 700 mV, while a 3 A transient in a two-inch trace induces a voltage of 4 V. Granted, component and trace layout are critical. To minimize trace inductance, the dI/dt loop must be laid out so that it has minimum diameter, with short, wide traces, as Figure 6.3 suggests.

As the use of external heat sinks is sometimes impossible, it is necessary to lay out sufficient copper to act as one. Additionally, inter-layer vias further reduce thermal stress and should be used in sufficient number as to minimize via impedance, [85, 86]. However, unnecessary large copper plane areas should be avoided, as to minimize trace inductance and noise radiation. Furthermore, sensitive, high impedance nodes, such as the current sensing nodes and voltage feedback nodes

should be traced as far away from noisy traces as possible, preferably in distinct layers. If sensing is accomplished differentially, both wires should be routed together, as close as possible. Finally, correct corner wiring should be accomplished. Right corner wiring can cause current waveform reflection and distortion, due to impedance changes - the larger the corner diameter, the smaller the impedance change will be (Figure 6.4), [87].

Figure 6.4: PCB Corner Wiring (from [87]).

6.1.2 Final Circuit

The final circuit is presented in Figure 6.5. Table 6.1 specifies the component differences between the two implemented boards - one uses series dimming, while the other uses parallel dimming. The board supports both dimming methods, by adjustment of a 6-pin header jumper, which alters the external PWM signal routing. The remaining component values and full schematic are detailed in Appendix B.1.

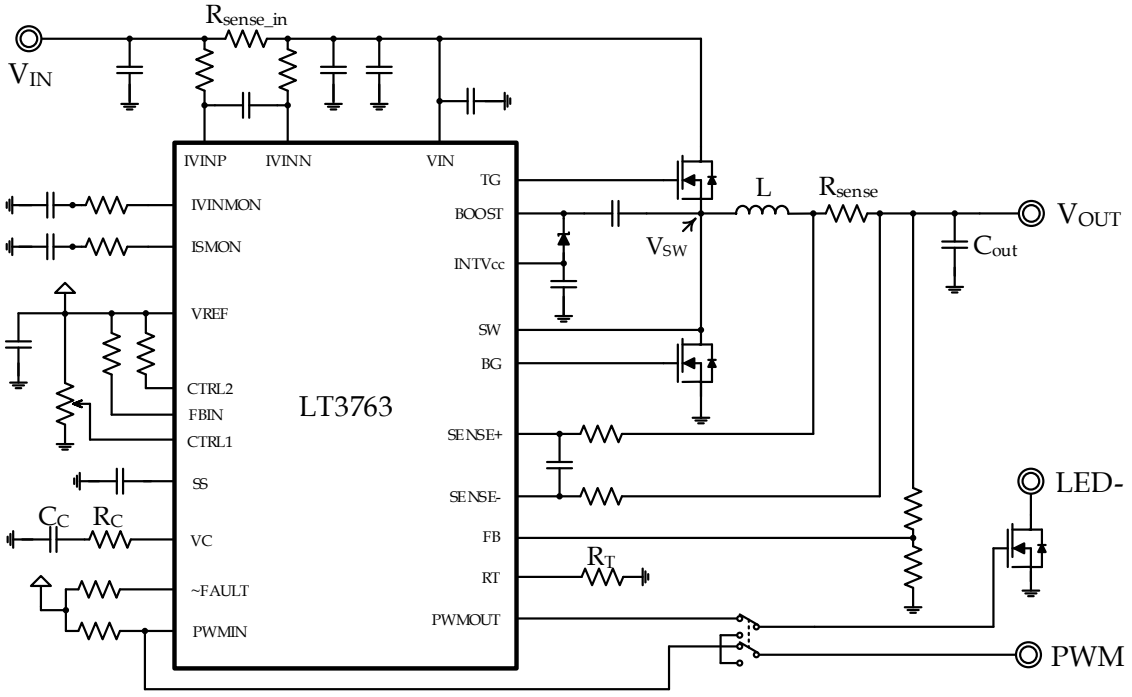

Figure 6.5: Final Proposed LED Driver schematic.

	Board A (series dimming)	Board B (parallel dimming)
R_{sense}	68 mΩ	68 mΩ
R_{sense_in}	68 mΩ	68 mΩ
L	4.7 μH	4.7 mH
C_{out}	44 μF	–
R_C	2.7 kΩ	413 kΩ
C_C	2 nF	38 pF
R_T	40.2 kΩ	220k Ω

Table 6.1: Component Specifications for each board.

6.1.3 Proposed Driver Board Layout

Figures 6.6 and 6.7 show the designed circuit boards for the proposed driver, and the difference between the two exemplifies the above remarks. Firstly, the first version's layout had a very large dI/dt loop. It can be easily identified - the SW node is common to the inductor, Top Gate source and Bottom Gate drain terminals, and the loop occupies nearly 1/5 of the total board area. The parasitic inductance resultant from unnecessary copper length in this high dI/dt is charged by the fast current pulses, which, in its turn, charges parasitic capacitances that lead to high transient, spike voltages. On the second version's layout, the dI/dt loop is significantly reduced - Top and Bottom gate MOSFETs are laid out very close to each other, and SW node area is minimized. Secondly, input filter capacitors are laid very close to Top Gate MOSFET, with wide land patterns, reducing noise and thermal stress. Multiple inter-layer vias are used throughout the board to further reduce thermal stress and inter-layer node impedance. Finally, the high-impedance nodes' (such as the current sense and voltage feedback nodes) layout was improved. There is sufficient distance between the voltage feedback node and noisy dI/dt nodes, and input and output current sense differential nodes were laid out as close as possible. Right corner wiring was minimized. Further enhancements on the second version's layout include:

- better input/output connections, for ease of use.
- 6-pin jumper header, to switch between internal or external PWM driving (allowing the board to work with both series and parallel dimming)
- inductor load current test points

Figure 6.8 showcases the populated implemented boards (figures are not at scale). Additionally, a board layout for the proposed RGB LED Driver in Chapter 5 was designed. Both schematic and board layout are shown in Appendix B.2.

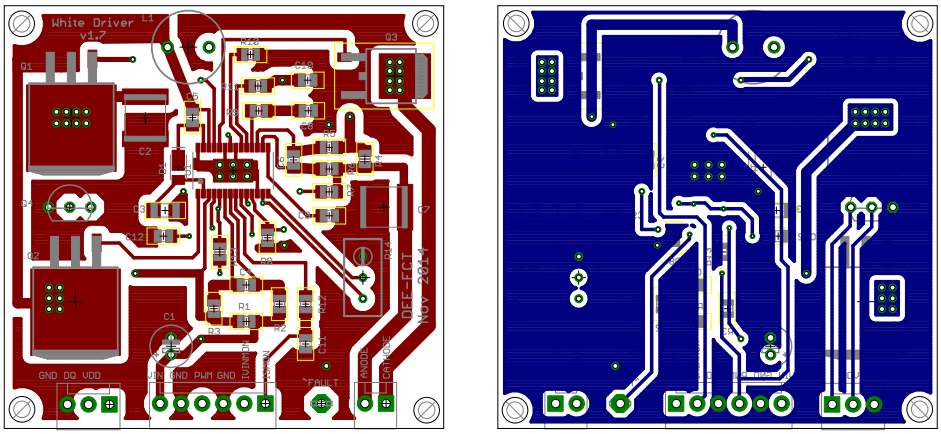

(a) Top Layer (b) Bottom Layer

Figure 6.6: Circuit Board (v1) for Proposed Driver.

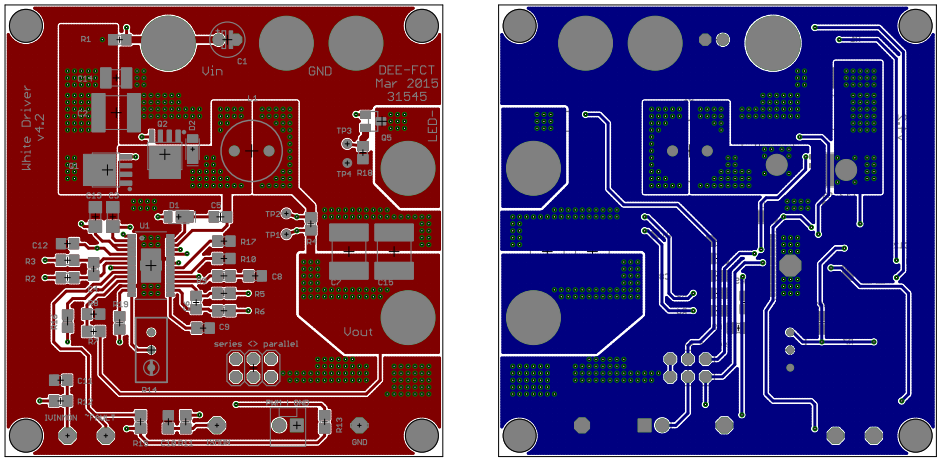

(a) Top Layer (b) Bottom Layer

Figure 6.7: Circuit Board (v2) for Proposed Driver.

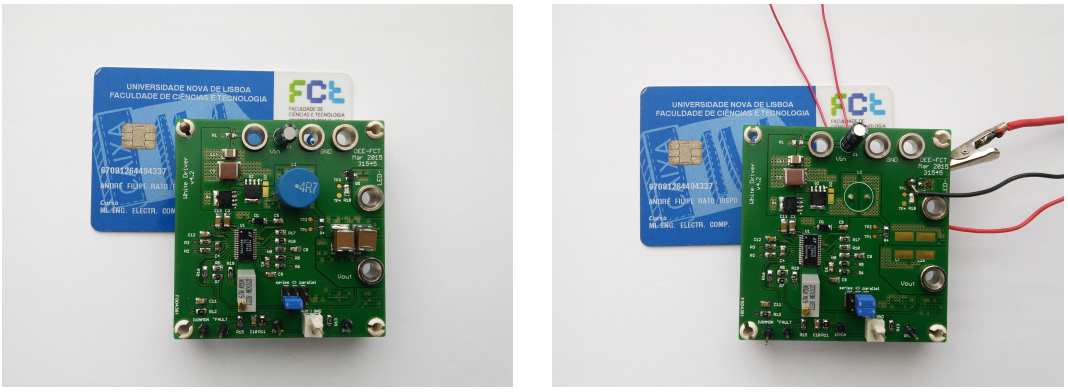

(a) Implemented board, using a series dimming scheme (b) Implemented board, using a parallel dimming scheme

Figure 6.8: Photos of the two implemented boards (card shown for scale).

6.2 Experimental Evaluation

6.2.1 Test Setup

Experimental evaluation was carried out for the LED Driver design validation. For different waveform validation, different measurement setups were used. For simple voltage measurements, a single oscilloscope channel was used; however, both channels were used for current measuring, by differential voltage monitoring, as shown by Figure 6.9.

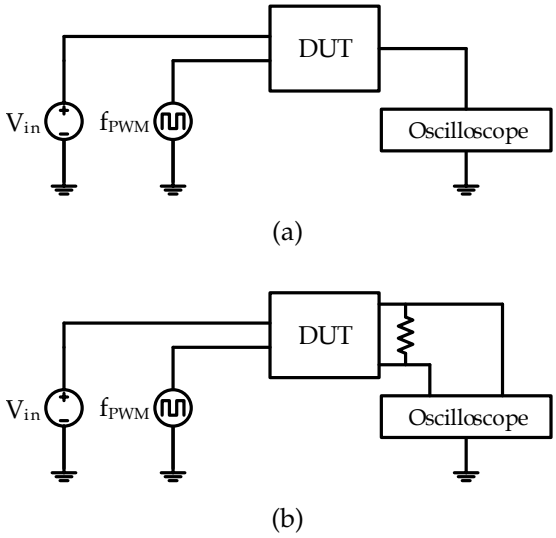

Figure 6.9: Testbench setup.

The Device Under Test (DUT) comprised both LED Driver and LED String. An external DC Power supply was used for LED Driver powering (V_{in}=50 V) and an external signal generator was used as a VLC+Dimming Data simulator, connected directly to the driver's PWM_{in} pin. The used equipment list is below.

- Multimetrix XA3033 Triple Output Adjustable DC Power Supply
- Iso-Tech IDS8062 60MHz, 2 Channel Digital Oscilloscope
- BK Precision 4017B 10MHz DDS Sweep/Function Generator

6.2.2 Preliminary Results

6.2.2.1 Series Dimming Board

Basic output voltage, output current and inductor current waveforms were registered. Output current was measured by means of the voltage drop in series resistor with with LED string ($R_{meas} = 0.68\ \Omega$). Inductor current was registered by means of the voltage probing using AC coupling on the R_{sense} node. Measured output voltage was 32.4 V. The discrepancy between this value and the expected value of 35 V is explained by the difference between the modelled and real LED strings, specifically, their V/I curve.

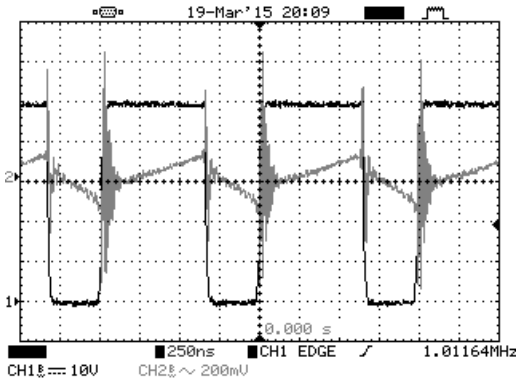

Figure 6.10: Inductor Current (grey) and V_{SW} (black) waveforms.

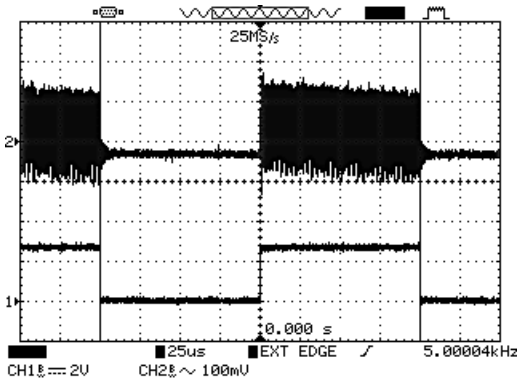

Figure 6.11: Inductor Current (top) and PWM Dimming (bottom) @ $f_{PWM} = 5$ kHz.

Figure 6.10 shows both the inductor current ripple and the V_{SW} voltage waveform. The duty-cycle of the switching waveform is approximately 0.65, which is coherent with both input and output voltages ($D = V_{out}/V_{in} = 32.4/50 = 0.648$). Switching and inductor current frequencies are coherent with the sized internal frequency of $f_{SW} = 1$ MHz (set by $R_T = 40.2\ k\Omega$).

Given that series dimming is employed, internal switching is stopped whenever the PWM dimming signal goes LOW - this is shown in Figure 6.11. For a dimming frequency of $f_{PWM} = 5$ kHz, the internal switching shutdown can be observed by the inductor current waveform (top).

LED current waveforms were registered for cases of no dimming and dimming at 500 Hz, 5kHz, 50 kHz and 500 kHz. This is depicted in Figure 6.12, by the black waveforms. Notice that the current's amplitude is always at the same level, throughout the dimming range. The voltage drop on R_{meas} when LEDs are conducting is 500 mV (plot scale is 500 mV/div), which computes to a current of $I = V/R_{meas} = 0.5/0.68 = 0.735$ A, coherent with the maximum current value,

set by $R_{sense} = 68\ m\Omega$. Figure 6.12e shows some slight ringing, which was not expected.

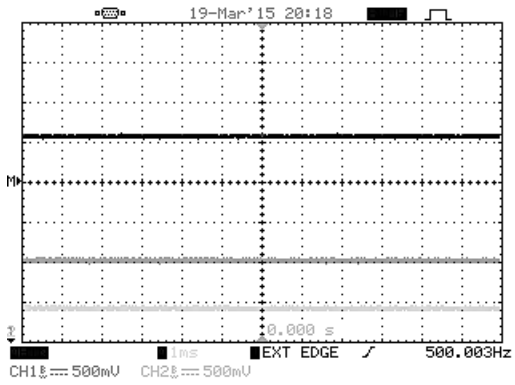

(a) No dimming

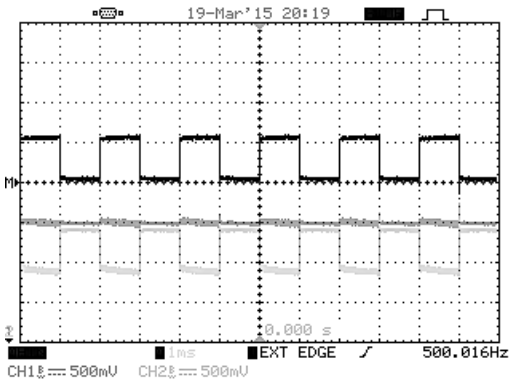

(b) Dimming with $f_{PWM} = 500$ Hz

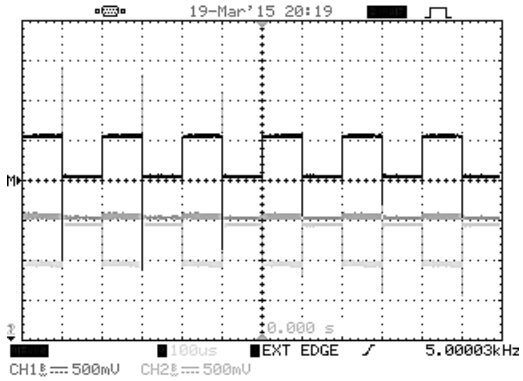

(c) Dimming with $f_{PWM} = 5$ kHz

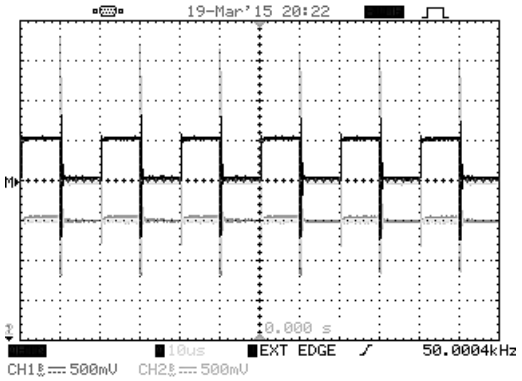

(d) Dimming with $f_{PWM} = 50$ kHz

(e) Dimming with $f_{PWM} = 500$ kHz

Figure 6.12: LED Current waveforms for various dimming frequencies.

Input and output power were calculated by means of average current measurement. The proposed driver included input and output current monitoring (IVINMON and ISMON, respectively), via current sensing on both R_{sense_in} and R_{sense}. The output voltage on both IVINMON and ISMON pins, which spans from

0 to 1 V, is proportional to the maximum set current. Thus, a 1 V reading on ISMON will indicate output current is the maximum set current which, for the used value of $R_{sense} = 68\ m\Omega$, equals $I_{max} = 0.735A$. Likewise, a reading of 0.55 V will correspond to a average current of 0.404 A. Input and output voltage and current, as well as input and output power are detailed in Tables 6.2 and 6.3. Figure 6.13 depicts efficiency for both $f_{PWM} = 1$ kHz and $f_{PWM} = 500$ kHz. Efficiency results for $f_{PWM} = 500$ kHz are very similar to those depicted in Figure 5.18a from SPICE simulation, as Figure 6.13b demonstrates.

Table 6.2: LED Driver's efficiency results, for $f_{PWM} = 1$ kHz, using series dimming.

Duty Cycle	V_{IN} (V)	IVINMON (V)	I_{IN} (A)	P_{IN} (W)	V_{OUT} (V)	ISMON (V)	I_{OUT} (A)	P_{OUT} (W)	Efficiency η
0.1	50.400	0.080	0.059	2.964	33.400	0.100	0.074	2.455	0.828
0.25	50.400	0.190	0.140	7.038	33.200	0.274	0.201	6.686	0.950
0.5	50.300	0.350	0.257	12.940	32.900	0.520	0.382	12.574	0.972
0.75	50.200	0.520	0.382	19.186	32.600	0.780	0.573	18.690	0.974
0.9	50.000	0.620	0.456	22.785	32.500	0.936	0.688	22.359	0.981
1	50.000	0.671	0.493	24.659	32.400	1.000	0.735	23.814	0.966

Table 6.3: LED Driver's efficiency results, for $f_{PWM} = 500$ kHz, using series dimming.

Duty Cycle	V_{IN} (V)	IVINMON (V)	I_{IN} (A)	P_{IN} (W)	V_{OUT} (V)	ISMON (V)	I_{OUT} (A)	P_{OUT} (W)	Efficiency η
0.1	50.100	0.100	0.074	3.682	35.000	0.084	0.0061	2.148	0.583
0.25	50.000	0.240	0.176	8.820	35.100	0.311	0.229	8.023	0.910
0.5	50.000	0.375	0.276	13.781	33.500	0.530	0.390	13.050	0.947
0.75	49.900	0.750	0.551	27.507	34.200	1.000	0.735	25.137	0.914
0.9	49.900	0.682	0.501	25.013	33.100	1.000	0.735	24.329	0.973
1	49.900	0.674	0.495	24.720	32.500	1.000	0.735	23.888	0.966

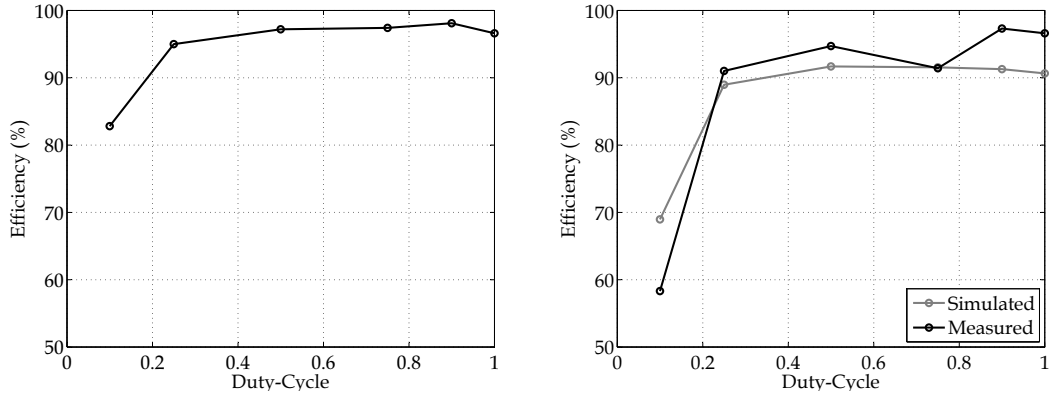

(a) $f_{PWM} = 1$ kHz (b) $f_{PWM} = 500$ kHz

Figure 6.13: Driver Efficiency using Series Dimming.

6.2.2.2 Parallel Dimming Board

Similar results are presented below for the Parallel Dimming Board. Contrarily to the previous circuit, which had an internal frequency of 1 MHz, this one works at $f_{SW} = 200$ kHz - besides, it uses no output capacitance, and thus inductor and LED currents are the same. Figure 6.14 shows the voltage waveform on the V_{SW} node. Note the lower frequency f_{SW} at 200 kHz. Figure 6.15 shows the output voltage with no dimming - i.e., parallel dimming MOSFET is off. Average voltage is 26 V, with a 2 V ripple. Given that there is no output capacitance, the voltage waveform follows that of the inductor current, hence the 200 kHz ripple.

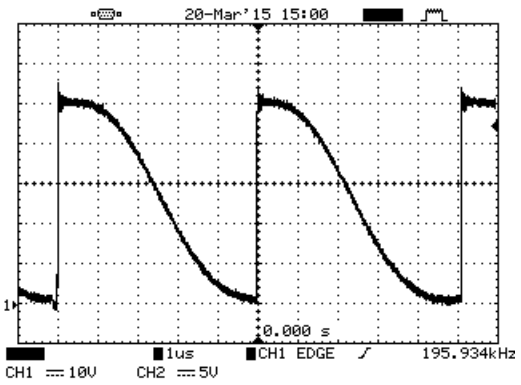

Figure 6.14: V_{SW} waveform.

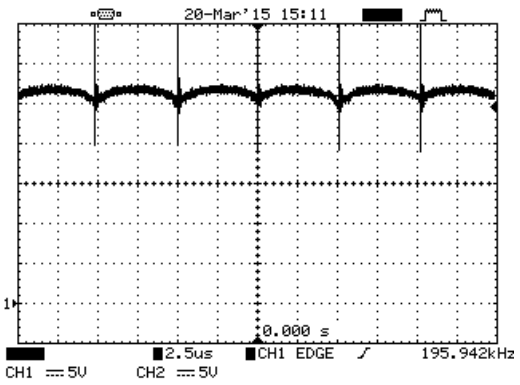

Figure 6.15: V_{out} waveform.

Dimming at various frequencies is illustrated in Figure 6.16. Given the lack of output capacitance, output voltage follows LED current. It should be noted that output voltage is not constant throughout the dimming range, contrarily to expected. Furthermore, when using a dimming frequency of $f_{PWM} = 500$ kHz, the waveform clearly shows prominent rise and fall times, which can be explained by the choice of PWM Driver. Contrarily to the sizing described in Chapter 5, the PWM Driver was substituted by the Renesas RFS16N05LS, whose maximum power specification easily supported the transient power peaks resultant from parallel dimming switching. The previously chosen SSM3K339R was undersized in that regard. However, the RFS16N05LS has a much larger charge gate Q_G, which contributes to its slower response.

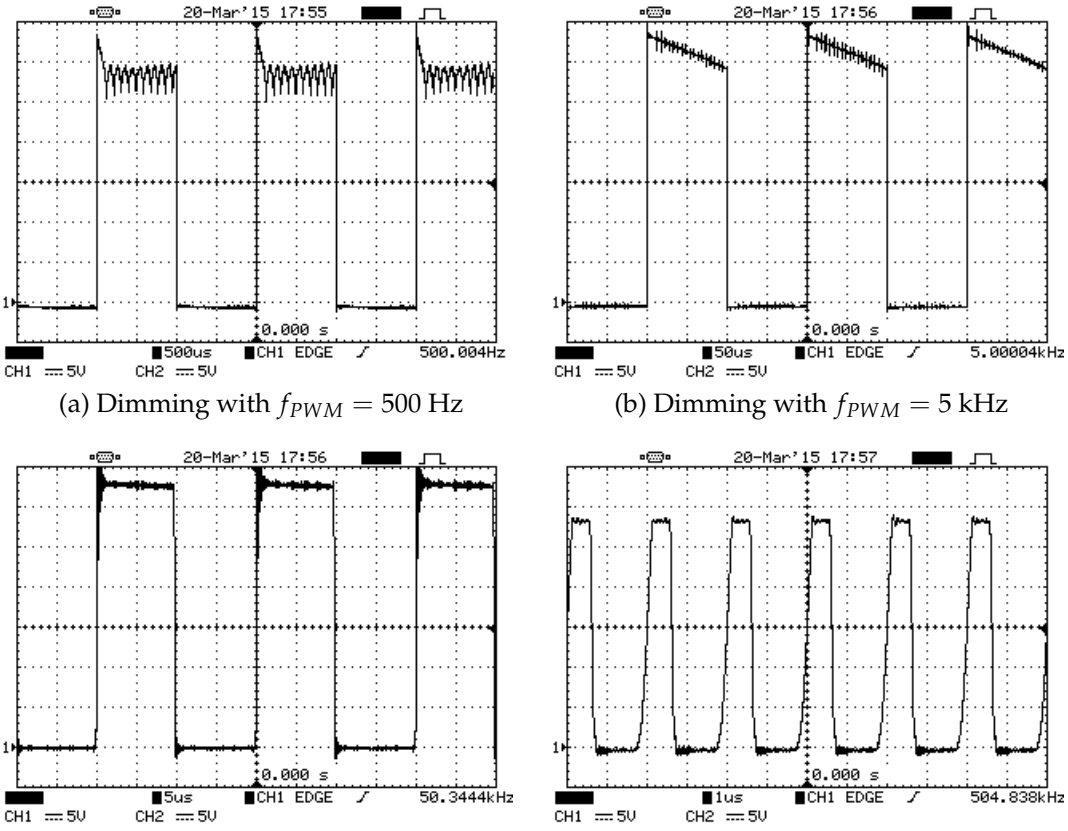

(a) Dimming with $f_{PWM} = 500$ Hz

(b) Dimming with $f_{PWM} = 5$ kHz

(c) Dimming with $f_{PWM} = 50$ kHz

(d) Dimming with $f_{PWM} = 500$ kHz

Figure 6.16: LED Voltage waveforms for various dimming frequencies.

Overall, the parallel dimming board presented rather erratic results, and needs further investigation. Output current and voltage values are very far off of those simulated. As mentioned by Modepalli et al [56], output capacitance in buck regulators aid in providing a charge path to the boost capacitor C_{boost}. However, using a parallel dimming scheme, the lack of output capacitance prevents C_{boost} from charging up. This aspect was not foreseen during the board's development, as all SPICE simulation results showed promising results. As stated above, additional circuitry may be required, as well as further investigation.

6.2.3 Low Data-Rate LED-to-LED Communication

As reported in Subsection 4.5.5, LEDs can act as transceivers in a bi-directional communication system. The LED's capacitive nature when reverse-biased can reveal itself useful, as its discharge curve alters when exposed to light. Further, more in-depth information can be found in Chapter 4. This section describes the implementation of a a simple LED-to-LED communication channel. Implemented code is available in Appendix C.

The Rx LED preference for use as a sensor resided on an ESD-protected SMD LED, with a peak emission wavelength of 640 nm (red coloured). The SMD preference is due to the fact that it features increased chip area, which combined with its high emission peak wavelength (and thus, smaller bandgap energy) makes it a very responsive LED, not only to red but also lower wavelengths. The Rx LED was operated by an Atmel ATmega328P microcontroller. On the Tx side, an Atmel ATmega2560 microcontroller generated the pulse train that connected to the LED Driver via the PWM input pin. Additionally, a BLE module interfaced with the Tx μC. This allowed for dimming adjustment, as well as for the transmission data alteration. The BLE module was based on a Texas Instruments CC2540, and connects to the Tx μC via hardware serial ports, hence the need for the ATmega2560 rather than a more simple ATmega328P. Both microcontrollers were synchronized with an external clock.

A simplified block diagram is present in Figure 6.17. The Tx LED string is driven by the developed LT3763 LED Driver.

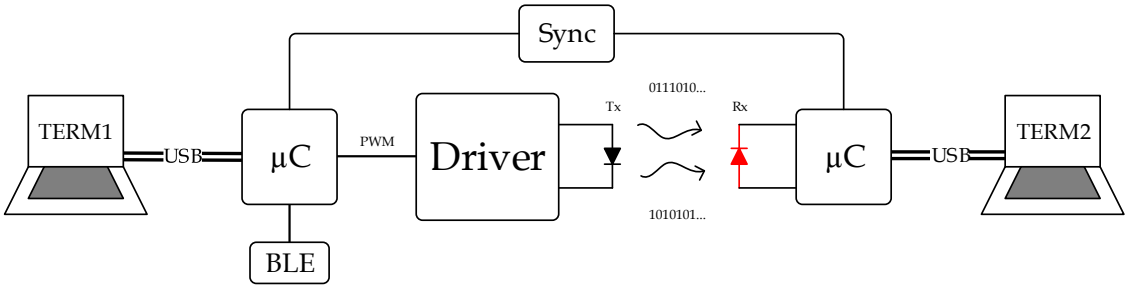

Figure 6.17: LED-to-LED block diagram.

The results shown in the subsections below depict the transmission (Tx) pulses and reception (Rx) patterns, using a white LED string and the aforementioned red LED, respectively. Light intensity of the transmitter string was 400 lm. Results were taken in a room with existing artificial lighting, but no direct sunlight was permitted.

6.2.3.1 Modulation and Bit Structure

The setup used a time-slot scheme, in which both LEDs altered their state to either receiving (Rx) or transmitting (Tx). Both states comprised the reception - and consequent decoding - and transmission - with preceding coding - of a 9 bit packet. OOK Modulation and Manchester coding (as per G.E. Thomas' convention) for DC balance, were employed. For simplicity sake, error protection encoding was not implemented. Figure 6.18 shows the transmitter and receiver block diagrams.

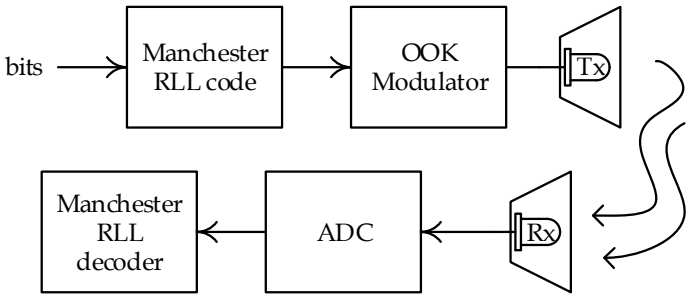

Figure 6.18: Transmitter and Receiver Block Diagrams.

The first bit served as a header bit which signalled data transfer. The remaining 8 bits were used for ASCII byte transfer. Figure 6.19 shows the data packet bit structure.

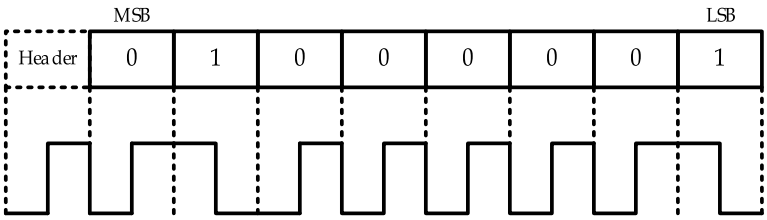

Figure 6.19: Data packet bit structure.

Figure 6.20 shows the Tx pulse train for a transmitted ASCII 'A' character. The first bit signals the presence ('0' (zero) bit) or absence ('1' (one) bit) of a character. Using Manchester encoding a zero bit is coded into a SPACE-MARK figure, whereas a one bit is coded into a MARK-SPACE figure. Having that in mind, the pulse train in Figure 6.20 is easily decoded. First bit has a SPACE-MARK figure which, by Manchester code, decodes into a zero bit - signalling the presence of a ASCII character bit. The next eight figures decode into the ASCII byte representative of the 'A' character - 01000001. Given that each byte contains two symbols (either a MARK or a SPACE), each byte corresponds to the measurement of two consecutive symbols. Thus, for the correct reception of a 9-bit data packet,

18 measurements must be done. Figure 6.21 shows the Rx pattern in the absence of incident light.

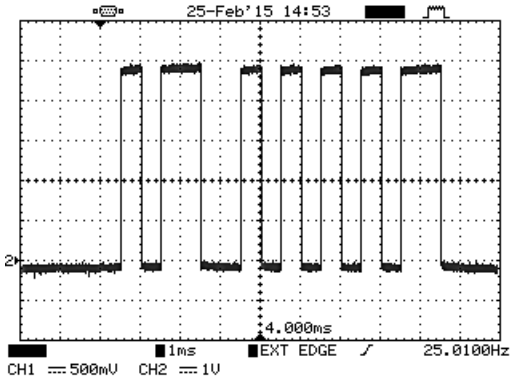

Figure 6.20: 'A' transmission pulse train.

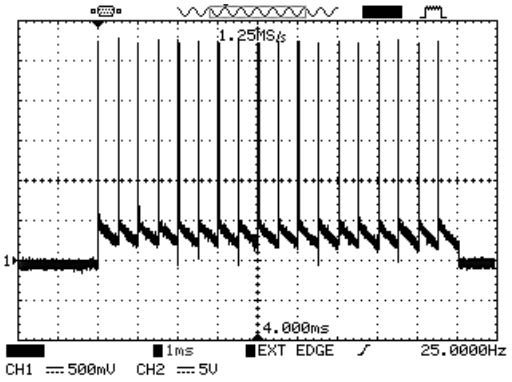

Figure 6.21: Rx idle pattern.

6.2.3.2 Symbol Width and Channel Length

Symbol width is particularly important in the receiving (Rx) state, when using this LED-to-LED low data-rate communication system. At low frequencies, rise and fall times are negligible when forward-biasing LEDs [88, 89] and do not affect operation in Tx state. On the other hand, LED's response time when reverse-biased may be somewhat limited. However, and as stated in Subsection 4.5.1, different techniques can be employed to improve both speed response and sensitivity for reverse-biased LEDs when used as sensors.

The use of OOK modulation poses some challenges. Firstly, it limits dimming. When using an alternative modulation technique, such as VPPM, dimming is already embedded in the symbol itself - by altering the symbol's duty-cycle, average light intensity is changed. However, when using OOK, symbol width and duty-cycle is fixed (at 50%), and therefore dimming must be achieved by the addition of *energy* periods - periods in which there is no data transmission, and LEDs output energy (i.e. light) for the sake of illumination. Due to the inclusion of this period, *data* periods (periods in which LEDs could be sending or receiving information) are less frequent. However, OOK modulation greatly simplifies the reception process, which is why it is preferred in this system. Consequently, in order to increase data-rate and throughput, symbol width must be decreased to a minimum. Symbol width is, however, limited by the optical channel itself. Intensity of light I falls at a distance d as $I \propto 1/d^2$. Thus, as channel length d

doubles, the light intensity is reduced to a quarter. This has major influence on the receiving end of the system, as shown later below.

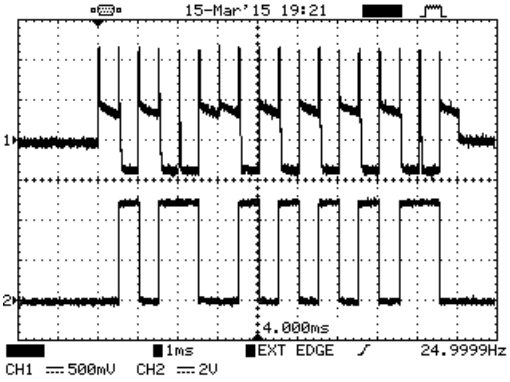

(a) Symbol Width of 500μs

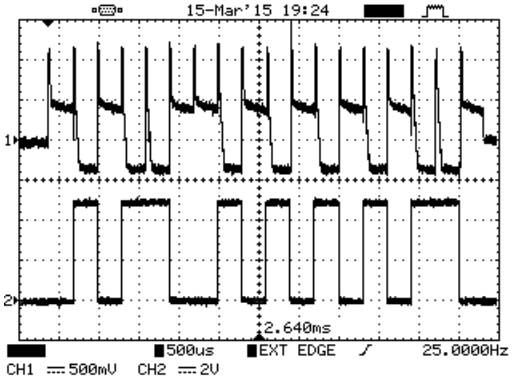

(b) Symbol Width of 300μs

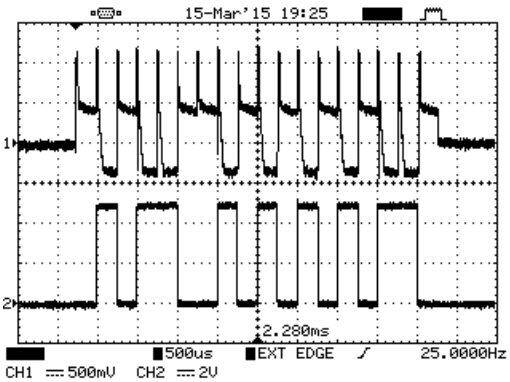

(c) Symbol Width of 250μs

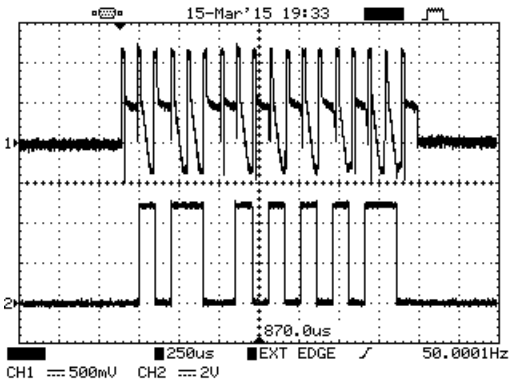

(d) Symbol Width of 100μs

Figure 6.22: Rx (top) and Tx (bottom) waveforms at $d = 15$ cm.

Figure 6.22 shows both Rx (top) and Tx (bottom) waveforms for an ASCII 'A' character transfer (binary 01000001) using 500μs, 300μs, 250μs and 150μ symbol widths respectively. Minimum realizable symbol width for this particular system is 100μs, which translates into a symbol rate of 10 kHz and a raw bit-rate of 5 kb/s. Distance d between transmitter and receiver was $d = 15$ cm. Light incidence is clearly visible in the Rx waveforms - the LED's junction capacitance is significantly discharged below zero volts, and light and no-light periods are easily distinguished. However, discharge curves in the Rx state differ significantly as symbol width decreases. Additionally, Figures 6.23 and 6.24 show similar results, for channel lengths of $d = 30$ cm and $d = 60$ cm respectively. As channel length doubles, light intensity at the receiver is reduced to a quarter, resulting in a clear increase of discharge times which, combined with the small symbol width, causes a depreciation in light/no-light distinction.

What should be retained is not whether the incident light will fully discharge

the LED or not. Provided that the symbol width is long enough it will always discharge completely (up to *charge depletion*). Although full discharge is favourable, as it greatly simplifies the ADC conversion process, smaller symbol widths are preferable, as they yield higher data-rates. Furthermore, longer channel lengths d reduce discharge time, which compromises symbol width. The goal is to obtain a compromise between as short discharge times and as long channel lengths as possible. As noted in Section 4.5, adding LEDs in series or parallel can alter the overall discharge curves - by having series of LEDs the overall capacitance is lowered; by having parallel LED rows, capacitance is increased, but light sensitivity is increased.

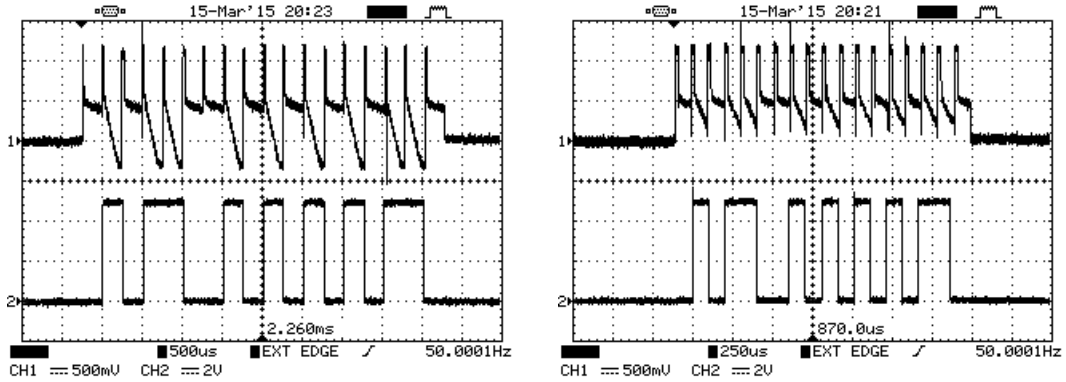

(a) Symbol Width of 250μs (b) Symbol Width of 100μs

Figure 6.23: Rx (top) and Tx (bottom) waveforms at $d = 30$ cm.

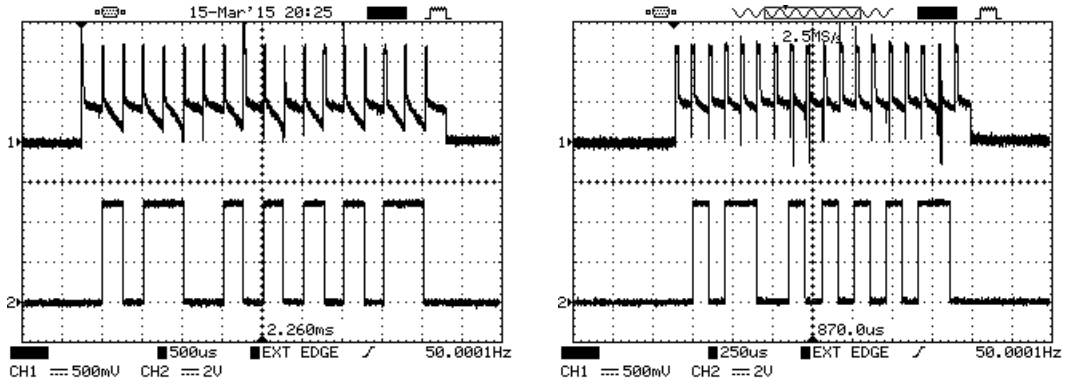

(a) Symbol Width of 250μs (b) Symbol Width of 100μs

Figure 6.24: Rx (top) and Tx (bottom) waveforms at $d = 60$ cm.

Series and Parallel Configuration

Figures 6.25 and 6.26 show the Rx and Tx waveforms using a series of three LEDs, and an array of three parallel LEDs.

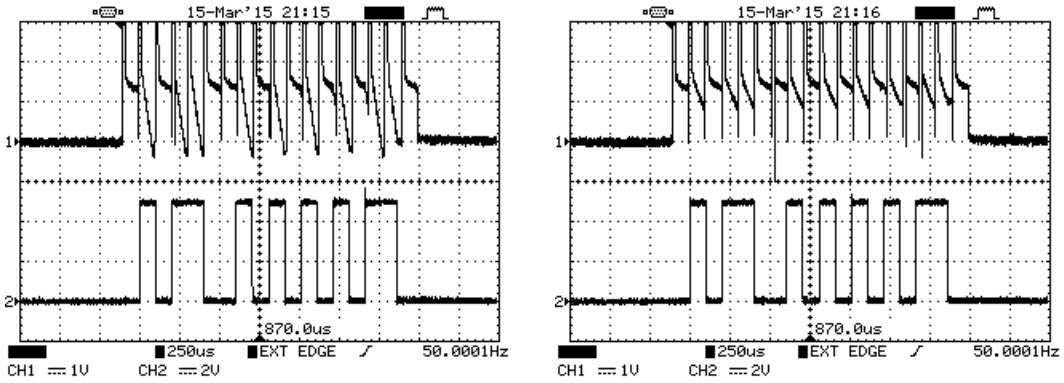

(a) $d = 15$ cm (b) $d = 30$ cm

Figure 6.25: Rx (top) and Tx (bottom) waveforms with 3 LEDs in series and symbol width of 100 μs.

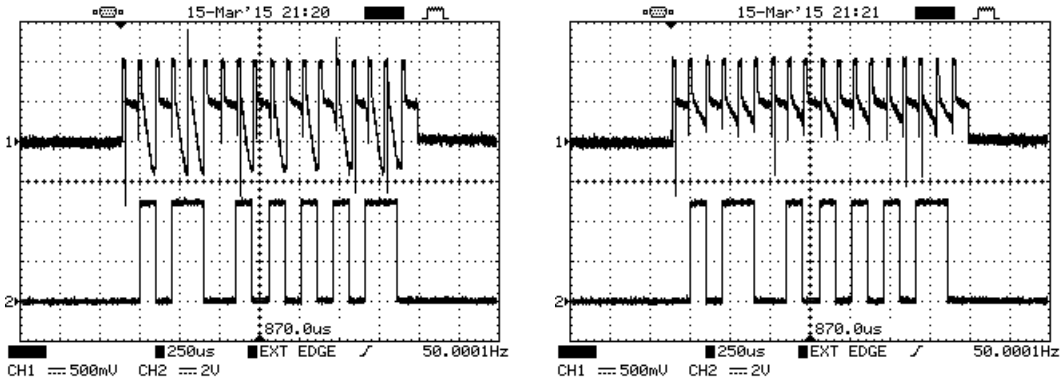

(a) $d = 15$ cm (b) $d = 30$ cm

Figure 6.26: Rx (top) and Tx (bottom) waveforms with 3 LEDs in parallel and symbol width of 100 μs.

While the use of parallel LEDs does not produce much of a difference, when compared to the single Rx LED, the use of a series of three LEDs as receivers almost doubles the voltage at the ADC's input [1]. This occurs for both $d = 15$ cm and $d = 30$ cm.

[1] This can be easily confirmed by observing the vertical Volt division of channel 1 CH1 (1V/div, as opposed to 500mV/div in the single LED approach)

6.2.3.3 ADC Measurement and Symbol Decoding

Proper analog-to-digital conversion on Rx state is crucial as it limits maximum symbol rate and system throughput, especially using the stock ADC. It is a 10-bit SAR ADC, whose clock runs at 125 kHz. Given that each ADC measurement takes 13 ADC clock cycles, this translates into a 9.6 kHz sample frequency - a successful ADC conversion every 104 μs [90]. However, by altering the ADC Clock's prescaler value from 128 to 16, a higher clock frequency can be obtained, without resolution loss [91]. Given that the Atmel's internal clock is 16 MHz, using a prescaler value of 16 results in a ADC clock frequency of 1 MHz, which in turn translates in a 77 kHz sample frequency (a successful conversion every 13 μs). However, experimental results show the conversion lasts approximately 20 μs as shown below in Figure 6.27.

For symbol decoding, the average value from the total of 18 measurements was computed. Given that MARK symbols correspond to light and SPACE symbols correspond to absence of light, the measured values on the ADC are lower for the former and higher for the latter symbols. After analog-to-digital conversion, each symbol's value was compared to the average and decoded accordingly - values higher than the average correspond to SPACE symbols whereas values lower than the average correspond to MARK symbols. Average light computation is done for each 9-bit packet - thus, the system is compatible with moderate changes in ambient light. The measuring periods, average value over one data-packet, as well as symbol decoding are depicted in Figure 6.27.

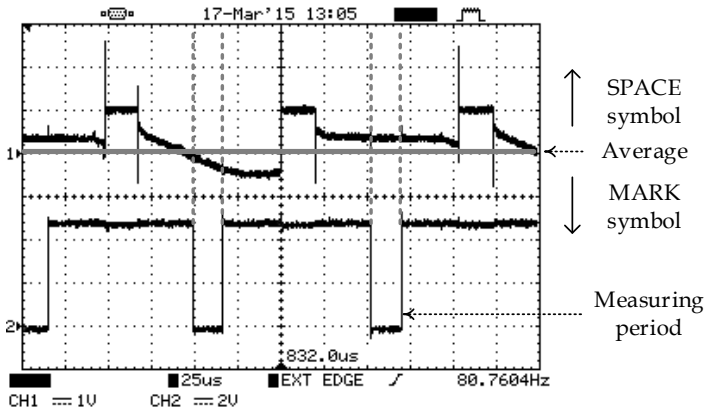

Figure 6.27: Symbol decoding and average value computation.

Figure 6.28 shows the voltage difference ΔV between MARK/SPACE symbols and the average value. It thus represents the system's ability to decode a symbol. A

higher value translates in more effective symbol decoding, whereas a smaller value means different symbols are very similar to each other, making their differentiation more prone to failure.

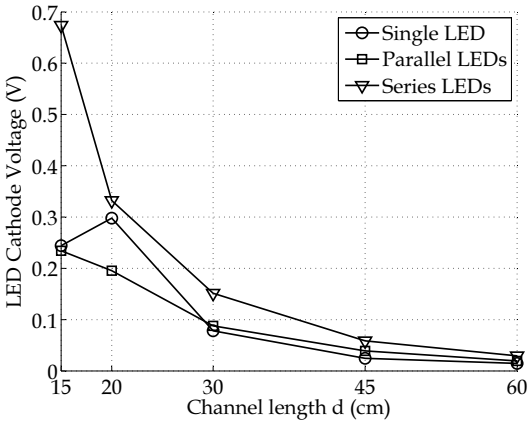

Figure 6.28: Measured voltage at LED's cathode when used as a sensor.

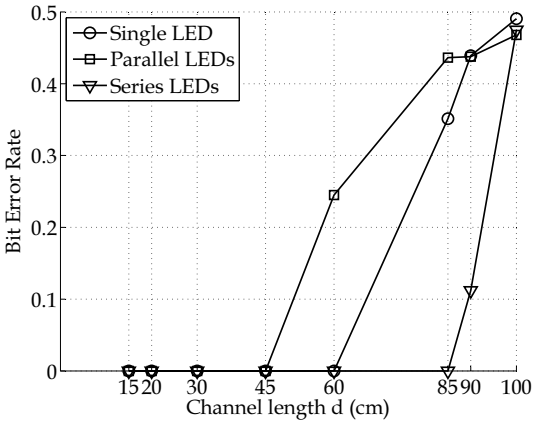

Figure 6.29: Bit Error Rate over channel length.

Parallel and single LED results are very similar over the 15-60 cm range. This could be explained by the fact that the parallel array was comprised of a low number of LEDs (m=3), and thus the $I_{gl} \times m$ (Section 4.5) effect is not noticeable. There is however, one difference to be pointed out, in the 15-20 cm range. For this channel length range, the incident light causes the single LED (small equivalent capacitance) to discharge very fast. Given that the LED's capacitance discharges over 0 V into negative values, and that the ADC's input range is limited to 0-5 V, the value for a MARK symbol saturates at 0 V. Thus, the measured ΔV is small. As channel length d increases to 20 cm, the measured value for a MARK symbol and average value are both positive, resulting in a larger ΔV value. On the other hand, when using a parallel array, given its higher equivalent capacitance, the discharge time is higher and therefore the MARK symbol measured level always exceeds 0 V - the ADC's input is never saturated. Consequently, even though the single LED and parallel array have disparate values for a channel length $d = 20$ cm, these should be attributed to the internal ADC rather than the LED itself. The results corresponding to the series LED string show that symbol differentiation is greatly enlarged, practically doubling the single/parallel results for the entire d range. Furthermore, the response over channel length obtained from the use of a series of LEDs greatly approximates the $1/d^2$ dependence, as pointed out in [6].

Additionally, Figure 6.29 shows how communication is affected with channel length d, for different LED configurations. The Bit error rate (BER) describes

how the received bits match the sent bits. The use of a series of LEDs enables communication up to 90 cm without failure. However, communication range is limited to 45 cm when using an array of parallel LEDs and 60 cm when using a single LED.

Although communication is limited to a maximum of 90 cm, it should be noted that the incident light was white, and not red. LEDs when used as sensors have a spectral selective sensitivity, slightly below its emission spectrum, as seen in Chapter 4. Even though the incident light was *white*, it has two emission peaks, blue and yellow. For an emission wavelength closer to the LED's spectral sensitivity (e.g. using Red LEDs for Tx), a larger communication range should be expected. Likewise, using a Tx source with a higher luminous output should yield larger ranges.

Distance/Cost Analysis

Distance and Cost relationship in this system is mostly dependant on the size of the emitter vs. the size of the receiver. The 90 cm figure obtained above is due to the light intensity of the emitter (400 lm) and the use of 3 LEDs in series, as receivers.

Increasing the light intensity at the emitter, i.e. by either using more LEDs or by increasing the LEDs forward current will permit the increase of the channel length. Many LED Drivers/lamps allow for the analog dimming of the LEDs, and thus will permit longer channel lengths at no expense, although some colour shifting is expected. Increasing the number of LEDs will linearly increase the emitters light intensity (provided they are operated at the same I/V point). Using either of these measures to increase channel length means, however, that light intensity at the emitter has to increase.

On the receiver side, a larger use of LEDs (either in series or parallel) will lead to increased sensitivity, as seen above, and as analysed in Subsection 4.5.5. However, a linear increase in the number of receiving LEDs will not correspond to a linear increase in channel length. This is the only measure, however, that does not require the overall light intensity to increase.

6.2.3.4 Dimming Support

As noted in Section 2.2, dimming support depends on the modulation type. For VPPM Modulation, dimming is achieved by changing each symbol's duty cycle. On the other hand, for OOK Modulation, dimming is achieved by adding compensation periods.

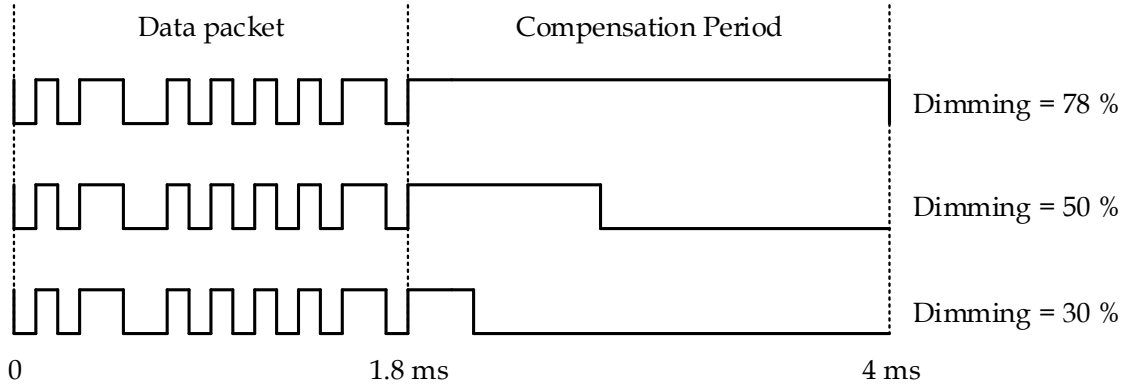

Figure 6.30: Tx Emission Period, comprising both data packet and compensation period.

Figure 6.30 shows the addition of a compensation period after the data packet, comprising the emission period. Due to the use of OOK modulation of the data packet, light time equals non-light time. Thus, for a symbol width of 100 μs, the data packet corresponds to 0.9 ms of light emission. Given that the emission period has a period of 4 ms (both Tx and Rx are externally synchonized by $f_{sync} = 250$ Hz), the data packet alone represents an effective dimming ratio of 22.5 %. If the compensation period is fully on, a maximum dimming ratio of 77.5 % is achieved. Higher maximum dimming ratios are possible if the emission period is increased - however, this will lead to a reduction of the effective data-rate. Thus, dimming range with data communication using $f_{sync} = 250$ kHz is limited to 22.5% - 77.5%.

6.2.3.5 Bi-directional Communication

The above scheme can be extended into a fully bi-directional system, as suggested by Figure 6.31.

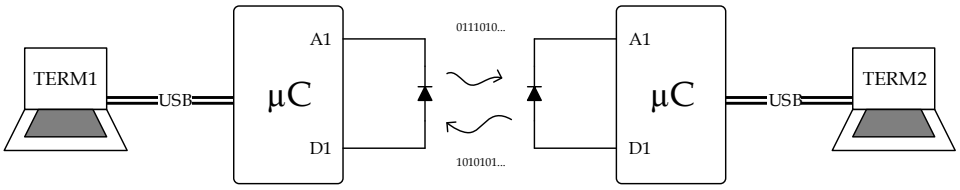

Figure 6.31: Bi-Directional LED-to-LED communication scheme.

Altering the LED's state between forward and reverse bias, it can indeed work as a transceiver, receiving in Rx state and transmitting in Tx state. Special attention is needed:

If using an LED Driver, there is need for extra circuitry responsible for LED state switching - LEDs are forward-biased when in Tx (transmission) mode, and reverse-biased when in Rx (reception) mode.

6.2.3.6 Synchronization

Although the developed system used an external synchronizing clock, common to both Tx and Rx modules, alternative synchronization techniques can be used. For systems in which both Tx and Rx modules operate off the grid, zero-crossing synchronization driven from the AC-grid can be implemented. Modern AC grids offer very little phase shift, and should suffice for synchronizing Tx and Rx modules [13]. For wireless or handheld systems, software-based synchronization like the used in the LED-to-LED system by Schmidt et al. [92] or Impulse based algorithm used for Ultra-Wide Bandwidth (UWB) [93, 94] are good contenders.

CHAPTER 7

CONCLUSIONS AND FUTURE WORK

7.1 Conclusions

This thesis proposed the investigation of two chief components of a joint communication and illumination system, mainly the LED Driver and an alternative Light Sensor, to be used as a receiver in said system.

Based on the work of Mims [8, 9] and Dietz et al [11], an alternative method os using LEDs as sensors was studied, in Chapter 4. Improvement over Dietz et al [11] work was made, with the use of a 10-bit ADC, which allowed for higher resolution. LED characteristics, such as their chip size, their package colour and the presence or absence of ESD devices were taken into account - both chip size and package colour have great impact on sensitivity. The larger the chip area and the more transparent the LED package is, the higher the sensitivity is, as more photons reach the p-n junction. Thorough analysis of the ESD device, and investigation of multiple LED behaviour when used in larger series and parallel strings and arrays were performed with aid of SPICE simulation, using a developed model. ESD devices are mostly intrusive when LEDs are used in small numbers. Using a string of series LEDs as sensors permits faster discharge rates, and thus smaller symbol widths. On the other hand, using LEDs as sensors in parallel increases equivalent capacitance, although the generated photocurrent is higher. In Chapter 6 an LED-to-LED system was experimented, using a symbol width of $t = 100\ \mu$s, and an adaptive packet-by-packet average computation algorithm, which permits its use in environments with variable ambient light. Using a 400 lm white light source, the receiver showed successful results up to the 90 cm range which, albeit lower

than similar reports [95], permitted increased throughput, with a raw bit rate of 5 kb/s. Also, results show that using LEDs in series, as opposed to using them in unity or in parallel, adds to the overall sensitivity and communication range, in accordance to the Chapter 4.

An LED Driver was designed and implemented, using the off-the-shelf LT3763 IC (Linear Technology). Two different dimming techniques were employed, using the same basic circuit. Extended simulations were performed, using both its SPICE model and a developed Simulink model. The circuit design was implemented on a 2-layer circuit board, using SMD components, and all soldering was done in-house. Experimental results are coherent with simulation results. Dimming at $f_{PWM} = 500$ kHz is achieved, using the series dimming, with efficiency figures over 90% for dimming over 20%. On the other hand, due to undersizing of the PWM Driver MOSFET, it was unable to demonstrate the dimming frequency of$f_{PWM} = 2$ MHz using a parallel dimming scheme and further investigation with this board is required. However, overall simulation and experimental outcome is coherent with other dual-purpose SMPS LED Drivers [56], showing promising results towards the possibility of VLC integration in existent SMPS LED Driver circuits, with minimal alteration.

7.2 Future Work

Given the developed work on the LED-to-LED communication system, further improvements can be done:

- Further investigation on parallel dimming, which allow for higher LED switching frequencies.

- Fully RGB Led-to-LED system with Illumination: as seen and suggested in Chapter 4, LEDs make for spectrally selective sensors. By having three different colour channels, WDM is possible, increasing throughput. Also, by not using phosphor coated LEDs, their bandwidth is extended, while still permitting white light generation, via colour mixing.

- Using larger LED source as sensors: extending the developed work on small LED strings, in series and parallel, investigation on using sources with a large number of LEDs, such as semaphore lights, ceiling LED luminaires, or even electronic billboards should be carried out. Also, the effect of variable reverse bias on LED spectral sensitivity must be detailed.

- Using CMOS image sensors as data receivers: given their construction - they are comprised of matrix of photodiodes - they should provide a perfect VLC sensor.
- Integration of full system in a PoE grid. This would allow for both powering and communication interfacing using a single physical connection.
- Integration between a LED Driver and the μC: if using a time-slot scheme on the LED, working as both Tx and Rx, LED multiplexing is required. The LED is forward biased when in Tx, and reverse biased when in Rx. While this state switching is trivial when using small LED strings, it becomes a challenge when using larger LED loads, which require higher voltage levels, and hence dedicated LED drivers. Figure 7.1 suggests some solutions. As seen in Section 4.5, LEDs strings can be reverse-biased with voltages similar to those used in forward-biasing. Thus, the driver itself can not only be used in Tx, but also in Rx, charging the junction capacitance of the LED string (Figure 7.1a). In this case, the connection between the driver and the LED string that must be sequentially switched. The ADC would probe the LED's cathode voltage exclusively in Rx periods (Figure 7.1b). Alternatively, the LED string can be disconnected entirely from the driver, and be directly charged (when in Rx) by the μC (Figure 7.1c).

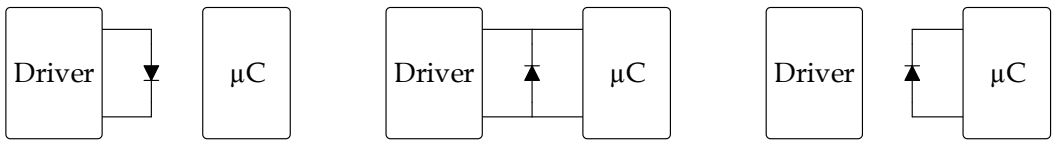

(a) Tx by LED Driver

(b) Reverse LED charged by Driver

(c) Reverse LED charged by μC

Figure 7.1: Solutions for Driver-LED-μC interface in Bi-directional scheme.

BIBLIOGRAPHY

[1] L. Coetzee and J. Eksteen. "The Internet of Things - promise for the future? An introduction". In: *IST-Africa Conference Proceedings, 2011*. May 2011, pp. 1–9.

[2] D. Evans. *The Internet of Things - How the Next Evolution of the Internet Is Changing Everything*. Tech. rep. HBD853/D, Rev.5 Apr-2014. Cisco (IBSG), Apr. 2011. URL: https://www.cisco.com/web/about/ac79/docs/innov/IoT_IBSG_0411FINAL.pdf (visited on 03/23/2015).

[3] F. Li, W. Qiao, H. Sun, H. Wan, J. Wang, Y. Xia, Z. Xu, and P. Zhang. "Smart Transmission Grid: Vision and Framework". In: *Smart Grid, IEEE Transactions on* Vol. 1.No. 2 (2010), pp. 168–177. ISSN: 1949-3053. DOI: 10.1109/TSG.2010.2053726.

[4] D. Olivares, A. Mehrizi-Sani, A. Etemadi, C. Canizares, R. Iravani, M. Kazerani, A. Hajimiragha, O. Gomis-Bellmunt, M. Saeedifard, R. Palma-Behnke, G. Jimenez-Estevez, and N. Hatziargyriou. "Trends in Microgrid Control". In: *Smart Grid, IEEE Transactions on* Vol. 5.No. 4 (2014), pp. 1905–1919. ISSN: 1949-3053. DOI: 10.1109/TSG.2013.2295514.

[5] M. Arias, A. Vazquez, and J. Sebastian. "An Overview of the AC-DC and DC-DC Converters for LED Lighting Applications". In: *Automatika - Journal for Control, Measurement, Electronics, Computing and Communications* Vol. 53.No. 2 (2012), pp. 156–172. ISSN: 0005-1144. DOI: 10.7305/automatika.53-2.154.

[6] A. Tsiatmas, C. P. M. J. Baggen, F. M. J. Willems, J. P. M. G. Linnartz, and J. W. M. Bergmans. "An illumination perspective on visible light communications". In: *IEEE Communications Magazine* Vol. 52.No. 7 (2014), pp. 64–71. ISSN: 01636804.

[7] A. Jovicic, J. Li, and T. Richardson. "Visible light communication: Opportunities, challenges and the path to market". In: *IEEE Communications Magazine*

Vol. 51.No. 12 (2013), pp. 26–32. ISSN: 01636804. DOI: 10.1109/MCOM.2013.6685754.

[8] F. M. Mims III. "LED Circuits and Projects". In: New York, NY, USA: Howard W. Sams and Co., Inc., pp. 60–61, 76–77, 122–123.

[9] F. M. Mims III. "Sun photometer with light-emitting diodes as spectrally selective detectors". In: vol. 31. No. 33. Optical Society of America, 1992, pp. 6965–6967.

[10] F. M. Mims III and R. D. Brooks. "Development of an inexpensive handheld LED-based Sun photometer for the GLOBE program". In: vol. 106. No. D5. American Geophysical Union, 2001, pp. 4733–4740.

[11] P. Dietz, W. Yerazunis, and D. Leigh. "Very Low Cost Sensing and Communication Using Bidirectional LEDS". In: *ACM International Conference on Ubiquitous Computing (UbiComp)*. Oct. 2003. URL: http://www.merl.com/publications/TR2003-35.

[12] V. Khanna. *Fundamentals of Solid-State Lighting: LEDs, OLEDs, and Their Applications in Illumination and Displays*. CRC Press, 2014. ISBN: 9781466561120.

[13] R. Laires. "Sistema de iluminação eficiente utilizando a tecnologia LED para espaços públicos interiores". MA thesis. DEE-FCT: Universidade Nova de Lisboa, 2013. URL: http://run.unl.pt/handle/10362/11127 (visited on 03/23/2015).

[14] *Golden DRAGON Plus*. Version 1.0. OSRAM. Aug. 2013. URL: http://www.osram-os.com/Graphics/XPic6/00087560_0.pdf/LCW\%20W5AM.pdf (visited on 03/23/2015).

[15] J. M. Kahn. "Wireless infrared communications". In: *Proceedings of the IEEE* Vol. 85.No. 97 (1997), pp. 265–298. ISSN: 00189219. DOI: 10.1109/5.554222.

[16] H. Elgala, R. Mesleh, and H. Haas. "Indoor optical wireless communication: Potential and state-of-the-art". In: *IEEE Communications Magazine* Vol. 49.No. 9 (2011), pp. 56–62. ISSN: 01636804. DOI: 10.1109/MCOM.2011.6011734.

[17] T. Yamazato, I. Takai, and H. Okada. "Image-sensor-based visible light communication for automotive applications". In: *IEEE Communications Magazine* No. 7 (2014), pp. 88–97.

[18] "Smart automotive lighting for vehicle safety". In: *IEEE Communications Magazine* Vol. 51.No. 12 (2013), pp. 50–59. ISSN: 01636804. DOI: 10.1109/MCOM.2013.6685757.

[19] "Visible light positioning: A roadmap for international standardization". In: *IEEE Communications Magazine* 51.No. 12 (2013), pp. 68–73. ISSN: 01636804. DOI: 10.1109/MCOM.2013.6685759.

[20] S. Rajagopal, R. Roberts, and S.-K. Lim. "IEEE 802.15.7 visible light communication: modulation schemes and dimming support". In: *Communications Magazine, IEEE* Vol. 50.No. 3 (2012), pp. 72–82. ISSN: 0163-6804.

[21] "IEEE Standard for Local and Metropolitan Area Networks–Part 15.7: Short-Range Wireless Optical Communication Using Visible Light". In: *IEEE Std 802.15.7-2011* (2011), pp. 1–309. DOI: 10.1109/IEEESTD.2011.6016195.

[22] E. C. Campos and H. E. Bedell. "Critical flicker-fusion frequency as an indicator of human receptive field-like properties". In: *Investigative Ophthalmology & Visual Science* Vol. 17.No. 6 (1978), pp. 533 –538.

[23] A Wilkins. "Intermittent Illumination from Visual Display Units and Fluorescent Lighting Affects Movements of the Eyes Across Text". In: *Hum. Factors* Vol. 28.No. 1 (Feb. 1986), pp. 75–81. ISSN: 0018-7208.

[24] S. M. Bergman, D. S. Greenhouse, R. D. Bailey, and T. W. Raasch. "Human Electroretinogram Responses to Video Displays, Fluorescent Lighting and Other High Frequency Sources". In: *Optometry and Vision Science* Vol. 68.No. 8 (1991), pp. 645 –662.

[25] D. Tsonev, S. Sinanovic, and H. Haas. "Complete Modeling of Nonlinear Distortion in OFDM-based Optical Wireless Communication". In: Vol. 31.No. 18 (2013), pp. 1–13. ISSN: 0733-8724. DOI: 10.1109/JLT.2013.2278675.

[26] J. Vucic, C. Kottke, S. Nerreter, K. D. Langer, and J. W. Walewski. "513 Mbit/s visible light communications link based on DMT-modulation of a white LED". In: *Journal of Lightwave Technology* Vol. 28.No. 24 (2010), pp. 3512–3518. ISSN: 07338724. DOI: 10.1109/JLT.2010.2089602.

[27] "3.4 Gbit/s visible optical wireless transmission based on RGB LED." In: *Optics express* Vol. 20.No. 26 (2012), B501–6. ISSN: 1094-4087. DOI: 10.1364/OE.20.00B501.

[28] "Intelligent lighting system using visible-light communication technology". In: *IEEE Conference on Cybernetics and Intelligent Systems* (2006), pp. 1–6. DOI: 10.1109/ICCIS.2006.252257.

[29] E. Schubert. *Light-emitting Diodes*. Cambridge University Press, 2003. ISBN: 9780521533515.

[30] *Silicon Photodiodes - Physics and Technology*. Tech. rep. OSI Optoelectronics, 1982. URL: http://www.osioptoelectronics.com/technology-corner/application-notes.aspx (visited on 03/23/2015).

[31] T. Carusone, D. Johns, and K. Martin. *Analog Integrated Circuit Design*. Analog Integrated Circuit Design. Wiley, 2011. Chap. 1. ISBN: 9780470770108.

[32] R. A. Millikan. "A Direct Photoelectric Determination of Planck's "h"". In: *Physical Review* Vol. 7 (Mar. 1916), pp. 355–388. DOI: 10.1103/PhysRev.7.355.

[33] C. R. Nave. *HyperPhysics - P-N Energy Bands*. URL: http://hyperphysics.phy-astr.gsu.edu/hbase/solids/pnjun2.html (visited on 01/13/2015).

[34] R. Frosch. *Constant-Voltage vs. Constant-Current LED Drivers - How Specifying the Proper LED Driver Can Provide Better Performance and Higher Quality Luminescence*. Tech. rep. Phihong USA. URL: http://btbmarketing.com/staging/phihong/Phihong_CC_vs_CV_LED_Drivers_White_Paper.pdf (visited on 03/23/2015).

[35] M. Kazimierczuk. *Pulse-width Modulated DC-DC Power Converters*. Wiley, 2008. Chap. 2,10,11,13. ISBN: 9780470694657.

[36] M. Brown. *Practical Switching Power Supply Design*. Ed. by Motorola. AP professional and technical series. Academic Press, 1990. Chap. 4. ISBN: 9780121370305.

[37] S. Maniktala. *Voltage-Mode, Current-Mode (and Hysteric Control), Technical Note TN-203*. Tech. rep. Microsemi, 2012. URL: http://www.microsemi.com/document-portal/doc_view/124786-voltage-mode-current-mode-and-hysteretic-control (visited on 03/23/2015).

[38] M. Berman. "What Type of LED Driver or Power Supply Do I Need?" In: TDK-Lambda Americas, Feb. 2012. URL: http://www.digikey.com/WebExport/SupplierContent/Lambda_285/PDF/tdk-what-led-driver.pdf (visited on 03/23/2015).

[39] C. Tse. *Complex Behavior of Switching Power Converters*. Power electronics and applications series. CRC Press, 2003. ISBN: 9780203494554.

[40] G. M. Di Blasi, P. Livreri, G. Capponi, and F. Marino. "A new current-mode control for DC/DC conveter". In: VDE-Verlag, 2005. ISBN: 9783800729050.

[41] H. J. Zhang. *Basic Concepts of Linear Regulator and Switching Mode Power Supplies*. Tech. rep. Linear Technology. URL: www.linear.com/docs/43921 (visited on 03/23/2015).

[42] *Optimum Feedback Amplifier Design For Control Systems, Technical Paper 3*. Tech. rep. Venable Industries. URL: http://venable.biz/resources/tech-papers-access-portal (visited on 03/23/2015).

[43] *Loop Compensation of Voltage-Mode Buck Converters, Application Note ANP 16*. Tech. rep. Sipex Corp, 2006. URL: http://www.exar.com/common/content/document.ashx?id=1238 (visited on 03/23/2015).

[44] D. Mattingly. *Designing Stable Compensation Networks for Single Phase Voltage Mode Buck Regulators*. Tech. rep. Intersil, 2003. URL: https://www.intersil.com/content/dam/Intersil/documents/tb41/tb417.pdf (visited on 03/23/2015).

[45] V. Vorperian. "Simplified Analysis of PWM Converters Using the Model of the PWM Switch: Parts I and II". In: *IEEE Transactions on Aerospace and Electronic Systems* No. 2 (1990).

[46] C. Deisch. "Simple Switching Control Method Changes Power Converter Into a Current Source". In: 1978, pp. 300–306.

[47] L. Dixon. *Average Current Mode Control of Switching Power Supplies*. Unitrode Seminar Section. 1990. URL: http://www.ti.com/lit/an/slua079/slua079.pdf (visited on 02/20/2015).

[48] R. Ridley. *A More Accurate Current-Mode Control Model*. Ridley Engineering. URL: http://citeseerx.ist.psu.edu/viewdoc/download?doi=10.1.1.365.5207\&rep=rep1\&type=pdf (visited on 02/21/2015).

[49] R. Holloway and G. Eirea. *Model Current-Mode Control With Ease and Accuracy*. Power Electronics Technology. Nov. 2008. URL: http://iie.fing.edu.uy/publicaciones/2008/HE08/HE08.pdf (visited on 02/20/2015).

[50] R. Sheehan. *Understanding and Applying Current-Mode Control Theory - Pratical Design Guide for Fixed-Frequency, Continuous Conduction-Mode Operation*. Power Electronics Technology Exhibition and Conference. 2007. URL: http://www.ti.com/lit/an/snva555/snva555.pdf (visited on 03/23/2015).

[51] U. Corp. *Modelling, Analysis and Compensation of the Current-Mode Converter*. Application Note U-97. Unitrode. URL: http://www.ti.com/lit/an/slua101/slua101.pdf (visited on 02/20/2015).

[52] L. H. Dixon Jr. *Current-Mode Control of Switching Power Supplies*. Unitrode Seminar. URL: http://www.ti.com/lit/ml/slup075/slup075.pdf (visited on 02/20/2015).

[53] D. Gacio, J. Alonso, J. Garcia, L. Campa, M. Crespo, and M. Rico-Secades. "PWM Series Dimming for Slow-Dynamics HPF LED Drivers: the High-Frequency Approach". In: *Industrial Electronics, IEEE Transactions on* Vol. 59.No. 4 (2012), pp. 1717–1727. ISSN: 0278-0046.

[54] S. Sarhan and C. Richardson. *A Matter of Light, Part I to IV*. Tech. rep. National Semiconductor. URL: http://www.eetimes.com/document.asp?doc_id=1273251 (visited on 03/23/2015).

[55] P. Narra and D. Zinger. "An effective LED dimming approach". In: *Industry Applications Conference, 2004. 39th IAS Annual Meeting. Conference Record of the 2004 IEEE*. Vol. Vol. 3. 2004, pp. 1671–1676.

[56] K. Modepalli and L. Parsa. "Dual-Purpose Offline LED Driver for Illumination and Visible Light Communication". In: *Industry Applications, IEEE Transactions on* Vol. 51.No. 1 (2015), pp. 406–419. ISSN: 0093-9994.

[57] B. Saleh and M. Teich. *Fundamentals of photonics*. Wiley series in pure and applied optics. Wiley, 1991. Chap. 15. ISBN: 9780471839651.

[58] K. Szolusha and T. Wong. "Boost-then-Buck LED Drivers Enable Wide PWM Dimming Range with Wide-Ranging Input Voltages". In: *Linear Technology, Journal of Analog Innovation* (Apr. 2014).

[59] *Photodiode Characteristics and Applications*. Tech. rep. OSI Optoelectronics. URL: http://www.osioptoelectronics.com/technology-corner/application-notes.aspx (visited on 03/23/2015).

[60] B. V. Zeghbroeck. *Principles of Semiconductor Devices - The p-n junction capacitance*. URL: http://ecee.colorado.edu/~bart/book/pncap.htm (visited on 01/13/2015).

[61] C. Engineering. *Lecture 9 - Transition and Depletion Capacitance*. URL: http://www.ee.columbia.edu/~bbathula/courses/SSDT/lect09.pdf (visited on 01/13/2015).

[62] *Golden DRAGON Plus Application Note*. OSRAM. Jan. 2014. URL: http://www.osram-os.com/Graphics/XPic1/00165108_0.pdf/Golden\%20DRAGON\%20Plus.pdf (visited on 03/23/2015).

[63] Hamamatsu. *Hamamatsu Opto-Semiconductor Handbook*. Chap. 2. URL: http://www.hamamatsu.com/sp/ssd/doc_en.html (visited on 03/23/2015).

[64] Y. Acharya. "Spectral and emission characteristics of LED and its application to LED-based sun-photometry". In: *Optics & Laser Technology* Vol. 37.No. 7 (2005), pp. 547 –550. ISSN: 0030-3992.

[65] E. Miyazaki, S. Itami, and T. Araki. "Using a light-emitting diode as a high-speed, wavelength selective photodetector". In: *Review of Scientific Instruments* 69.11 (1998), pp. 3751–3754.

[66] K.-T. Lau, S. Baldwin, M. O'Toole, R. Shepherd, W. J. Yerazunis, S. Izuo, S. Ueyama, and D. Diamond. "A low-cost optical sensing device based on paired emitter–detector light emitting diodes". In: *Analytica Chimica Acta* Vol 557.1–2 (2006), pp. 111 –116. ISSN: 0003-2670.

[67] *Bluetooth Low Energy*. URL: http://www.bluetooth.com/Pages/low-energy-tech-info.aspx (visited on 03/23/2015).

[68] H. Matsuoka, J. Wang, L. Jing, Y. Zhou, Y. Wu, and Z. Cheng. "Development of a control system for home appliances based on BLE technique". In: *Independent Computing (ISIC), 2014 IEEE International Symposium on*. 2014, pp. 1–5. DOI: 10.1109/INDCOMP.2014.7011751.

[69] L. T. Berger, A. Schwager, and J. J. Escudero-Garzás. "Power Line Communications for Smart Grid Applications". In: Hindawi Publishing Corporation. DOI: doi:10.1155/2013/712376.

[70] *60V High Current Step-Down LED Driver Controller*. LT3763. LT 0513 REV A. Linear Technology. 2012. URL: www.linear.com/docs/42223 (visited on 03/23/2015).

[71] *AN-1197 Selecting Inductors for Buck Converters*. Tech. rep. Texas Instruments, Apr. 2013. URL: www.ti.com/lit/an/snva038b/snva038b.pdf (visited on 03/23/2015).

[72] *0.6V to 5.5V Output, Parallelable, Average-Current-Mode DC-DC Controllers*. MAX5060. 19-3583; Rev 2; 7/05. Maxim Integrated. URL: http://datasheets.maximintegrated.com/en/ds/MAX5060-MAX5061.pdf (visited on 03/23/2015).

[73] *Controller IC for Dimmable Offline LED Lamps*. MAX16841. 19-6028; REV 1; 6/13. Maxim Integrated. URL: http://datasheets.maximintegrated.com/en/ds/MAX16841.pdf (visited on 03/23/2015).

[74] *AN2239 Maximizing Synchronous Buck Converter Efficiency*. Tech. rep. STMicroelectronics. URL: www.bdtic.com/download/st/an2239.pdf (visited on 03/23/2015).

[75] H. Bai. *Design Note - 60V, Synchronous Step-Down High Current LED Driver*. Tech. rep. Linear Technology. URL: www.linear.com/docs/44711.

[76] S. Basu, M. H. Bollen, and T. M. Undeland. "PFC Strategies in light of EN 61000-3-2". In: *APEC paper A* 123656 (2004). URL: http://www.elkraft.ntnu.no/eno/Papers\%202004/EPE04-Supratim-Bollen-Undeland.pdf (visited on 03/23/2015).

[77] *Power Factor Correction Handbook*. Tech. rep. HBD853/D, Rev.5 Apr-2014. ON Semiconductor, 2014. URL: www.onsemi.com/pub/Collateral/HBD853-D.PDF (visited on 03/23/2015).

[78] A. M. Makdessian. *The Bright New Outlook For LEDs: New Drivers, New Possibilities*. Tech. rep. Maxim Integrated, 2015. URL: http://www.maximintegrated.com/content/dam/files/products/campaigns/solutions/led-white-paper.pdf (visited on 04/30/2015).

[79] P. Savage, R. R. Nordhaus, and S. Jamieson. "DC Microgrids: Benefits and Barriers". In: *From Silos to Systems: Issues in Clean Energy and Climate Chage* (). URL: http://environment.yale.edu/publication-series/documents/downloads/0-9/05-DC-Microgrids.pdf (visited on 03/23/2015).

[80] B. Patterson. "DC, Come Home: DC Microgrids and the Birth of the "Enernet"". In: *Power and Energy Magazine, IEEE* Vol. 10.No. 6 (2012), pp. 60–69. ISSN: 1540-7977. DOI: 10.1109/MPE.2012.2212610.

[81] L. H. Koh, Y. K. Tan, Z. Z. Wang, and K. J. Tseng. "An energy-efficient low voltage DC grid powered smart LED lighting system". In: *IECON Proceedings (Industrial Electronics Conference)* (2011), pp. 2883–2888. ISSN: 1553-572X. DOI: 10.1109/IECON.2011.6119610.

[82] D. Salomonsson and A. Sannino. "Low-voltage DC distribution system for commercial power systems with sensitive electronic loads". In: *IEEE Transactions on Power Delivery* Vol. 22.No. 3 (2007), pp. 1620–1627. ISSN: 08858977. DOI: 10.1109/TPWRD.2006.883024.

[83] IEEE. *IEEE 802.3: ETHERNET*. URL: https://standards.ieee.org/about/get/802/802.3.html (visited on 03/20/2015).

[84] *Understanding 802.3at - PoE Plus Standard Increases Available Power*. Tech. rep. PD2011-1-WP. Microsemi, June 2011. URL: http://www.streakwave.com/powerdsine/Understanding_802_3at_PowerDsine.pdf (visited on 03/20/2015).

[85] H. J. Zhang. *PCB Layout Considerations for Non-Isolated Switching Power Supplies*. Tech. rep. Linear Technology. URL: www.linear.com/docs/42146 (visited on 03/23/2015).

[86] *AN-1229 PCB Layout Guidelines*. Tech. rep. Texas Instruments. URL: www.ti.com/lit/an/snva054c/snva054c.pdf (visited on 03/23/2015).

[87] *PCB Layout Techniques of Buck Converter*. Tech. rep. Rohm Semiconductor. URL: http://edge.rit.edu/content/P14251/public/Schematics/Electrical/PCB\%20Info/converter_pcb_layout_appli-e.pdf (visited on 03/23/2015).

[88] A. Brailovsky and V. Mitin. "Fast switching of light-emitting diodes". In: *Solid-State Electronics* Vol. 44.No. 4 (2000), pp. 713 –718. ISSN: 0038-1101.

[89] H. Halbritter, C. Jager, R. Weber, M. Schwind, and F. Mollmer. "High-Speed LED Driver for ns-Pulse Switching of High-Current LEDs". In: *Photonics Technology Letters, IEEE* Vol. 26.No. 18 (2014), pp. 1871–1873. ISSN: 1041-1135.

[90] *Atmel 8-bit Microcontroller with 32KBytes In-System Programmable Flash*. ATmega328P. 8271G–AVR–02/2013. Atmel. URL: http://www.atmel.com/images/doc8161.pdf (visited on 03/23/2015).

[91] G. van den Berg. *Microsmart - Advanced Arduino ADC – Faster analogRead()*. URL: http://www.microsmart.co.za/technical/2014/03/01/advanced-arduino-adc/ (visited on 02/26/2015).

[92] S. Schmid, G. Corbellini, S. Mangold, and T. Gross. "An LED-to-LED Visible Light Communication system with software-based synchronization". In: *Globecom Workshops (GC Wkshps), 2012 IEEE*. 2012, pp. 1264–1268. DOI: 10.1109/GLOCOMW.2012.6477763.

[93] M. Win and R. Scholtz. "Impulse radio: how it works". In: *Communications Letters, IEEE* 2.2 (1998), pp. 36–38. ISSN: 1089-7798. DOI: 10.1109/4234.660796.

[94] M. Win and R. Scholtz. "Ultra-wide bandwidth time-hopping spread-spectrum impulse radio for wireless multiple-access communications". In: *Communications, IEEE Transactions on* 48.4 (2000), pp. 679–689. ISSN: 0090-6778. DOI: 10.1109/26.843135.

[95] S. Schmid, G. Corbellini, S. Mangold, and T. Gross. "Connecting networks of toys and smartphones with visible light communication". In: *IEEE Communications Magazine* Vol. 52.No. 7 (2014), pp. 72–78. ISSN: 01636804. DOI: 10.1109/MCOM.2014.6852086.

APPENDIX A

COMPENSATION NETWORKS FOR VOLTAGE MODE CONTROL REGULATORS

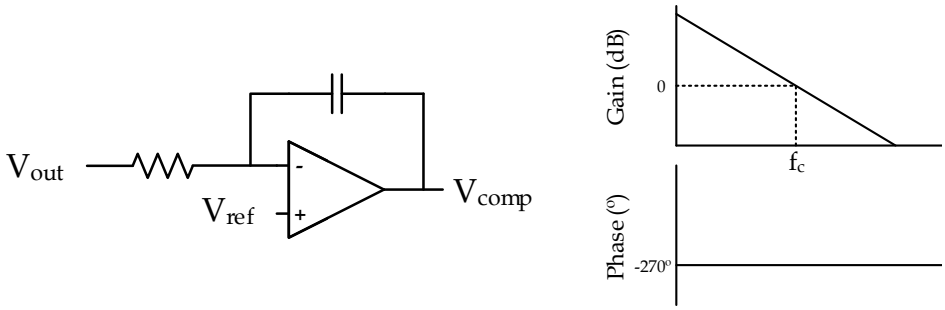

(a) (b)

Figure A.1: Type I Compensator.

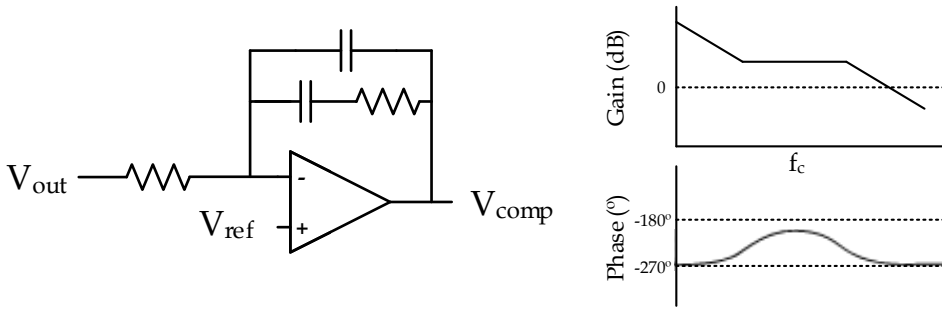

(a) (b)

Figure A.2: Type II Compensator.

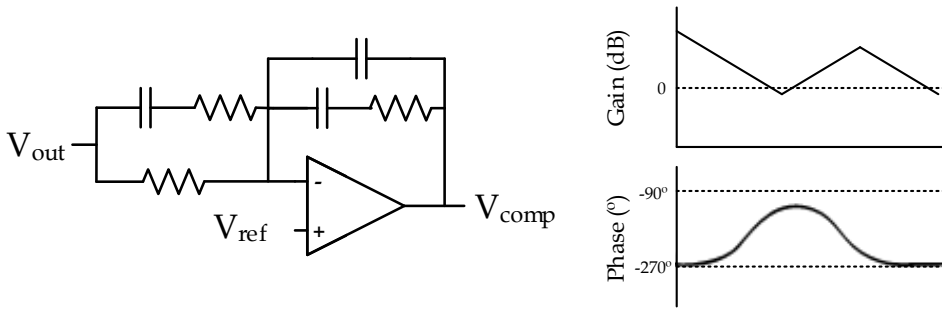

(a) (b)

Figure A.3: Type III Compensator.

APPENDIX B

CIRCUIT BOARDS AND SCHEMATICS

B.1 White LED Driver

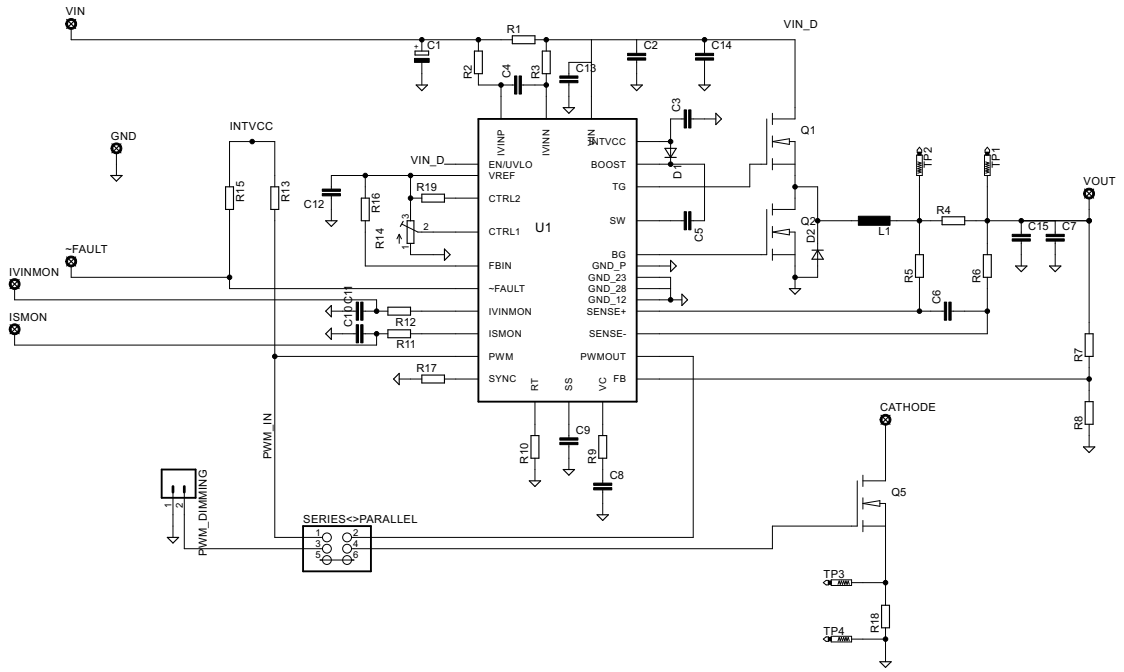

Figure B.1: White LED Driver schematic.

Table B.1: White LED Driver Bill of Materials

Part	Value	Part	Value
C1	10 μF	R1	68 mΩ
C2	4.7 μF	R2	1 kΩ
C3	22 μF	R3	1 kΩ
C4	1 μF	R4	68 mΩ
C5	220 nF	R5	10 Ω
C6	33 nF	R6	10 Ω
C9	10 nF	R7	90.9 kΩ
C10	1 nF	R8	3.1 kΩ
C11	1 nF	R11	50 Ω
C12	220 nF	R12	50 Ω
C13	1 μF	R13	100 kΩ
C14	2.2 μF	R14	50 kΩ
D1	DFLS160	R15	100 kΩ
D2	DFLS260	R16	100 kΩ
Q1	BUK9Y15-60E	R17	100 kΩ
Q2	BUK9Y15-60E	R18	10 mΩ
Q3	SSM3K339	R19	100 kΩ
U1	LT3763		

B.2 RGB LED Driver

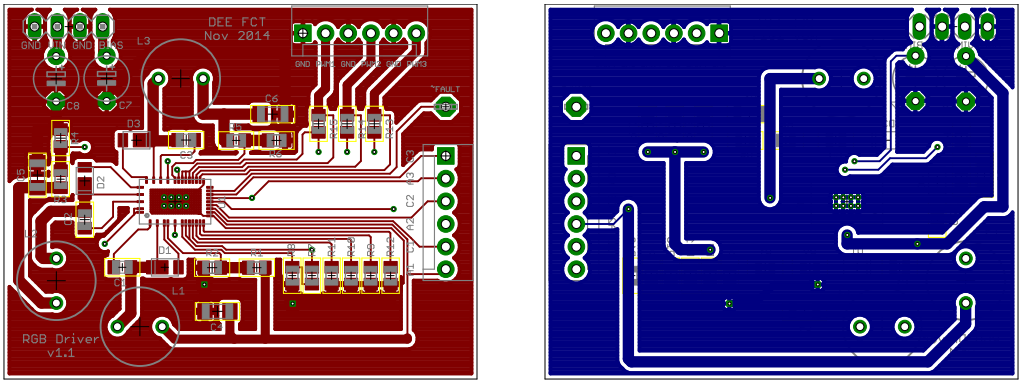

(a) Top Layer (b) Bottom Layer

Figure B.2: Circuit Board for proposed RGB LED Driver.

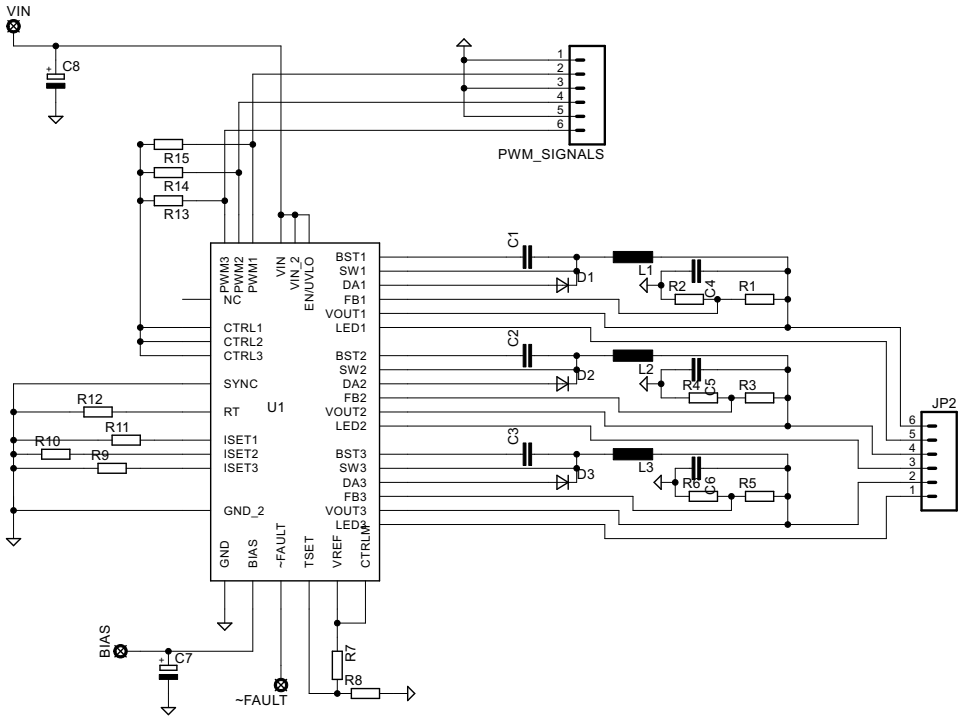

Figure B.3: RGB LED Driver schematic.

Table B.2: RGB LED Driver Bill of Materials.

Part	Value	Part	Value
C1	220 nF	R1	82 kΩ
C2	220 nF	R2	4.4 kΩ
C3	220 nF	R3	82 kΩ
C4	4.7 uF	R4	2.75 kΩ
C5	4.7 uF	R5	82 kΩ
C6	4.7 uF	R6	2.78 kΩ
C7	10 uF	R7	90.9 kΩ
C8	10 uF	R8	49.9 kΩ
D1	DFLS160	R9	20 kΩ
D2	DFLS160	R10	20 kΩ
D3	DFLS160	R11	20 kΩ
L1	100 uH	R12	33.2 kΩ
L2	100 uH	R13	100 kΩ
L3	100 uH	R14	100 kΩ
U1	LT3597	R15	100 kΩ

APPENDIX C

LED-TO-LED RX AND TX CODE

C.1 Code for Rx LED

```
#include <eRCaGuy_Timer2_Counter.h>
#define NOP __asm__ __volatile__ ("nop\n\t")
#define LED_MARK 100

//definitions for ADC prescaler mod
const unsigned char PS_16 = (1 << ADPS2);
const unsigned char PS_32 = (1 << ADPS2) | (1 << ADPS0);
const unsigned char PS_64 = (1 << ADPS2) | (1 << ADPS1);
const unsigned char PS_128 = (1 << ADPS2) | (1 << ADPS1) | (1 << ADPS0);

boolean tempo=false, tempo_ADC=false, message=false, canprint=false;
unsigned long previous, current;
int i,j;
long data_buffer[18]={0,0,0,0,0,0,0,0};
int marker = 12; // marker output pin

void setup()
{
        timer2.setup();
        _SFR_IO8(0x35) |= 0x10;   // global disable pull up resistors
        Serial.begin(9600);
    ADCSRA &= ~PS_128;  // remove bits set by Arduino library
    ADCSRA |= PS_16;
    DDRB |= 1 << 4; //pin A0 as output
    bitSet(PORTB, 4);
    attachInterrupt(0, main_loop, CHANGE);
}

void loop(){ //ADC values are decoded
```

```
  if (canprint) {
    int sum,avg;
    for (i=0;i<18;i++){
      sum+=data_buffer[i];
    }
    avg=sum/18;

    for (i=0;i<18;i++){
      if (data_buffer[i] > avg)
        data_buffer[i]=0;
      else
        data_buffer[i]=1;
    }
    if(!data_buffer[0] && data_buffer[1]) {
      message=true;
      char buff=0x00;
      for (i=2,j=0;i<18;i=i+2,j++){
        if (!data_buffer[i] && data_buffer[i+1]==1)
          buff |= (0x00 << (7-j));
        else if (data_buffer[i] && !data_buffer[i+1])
          buff |= (0x01 << (7-j));
      }
      Serial.print(buff,BIN); //received byte is printed to serial monitor
    }
    else {
      message=false;
    }
    canprint=false;
  }
}

void main_loop(){ //LED is reversed, charged and ADC reads value

    for (i=0;i<18;i++){
      previous = timer2.get_count(); //get time

      //charge capacitance
      DDRC |= 1 << 0; //pin A0 as output
      DDRD |= 1 << 7; //pin 7 as output
      PORTD &= ~(1 << 7); //pull pin7 low
      PORTC |= (1 << 0); //write HIGH in PIN A0

      //wait
      delayMicroseconds(20);

      //discharge
      DDRC &= ~(1 << 0); //pin A0 as INPUT
      PORTC &= ~(1 << 0); //write LOW in A0

      //esperar por ADC
      while(!tempo_ADC){
        current=timer2.get_count();
        if ((current-previous) >= (2*(LED_MARK-50))){
          tempo_ADC=true;
```

```
        }
      }
      bitClear(PORTB, 4);
      data_buffer[i]=analogRead(A0);
      bitSet(PORTB, 4);
      tempo_ADC=false;

      while(!tempo){
        current=timer2.get_count();
        if ((current-previous) >= (2*LED_MARK)-15){
          tempo=true;
        }
      }
      tempo=false;
    }
    DDRC |= 1 << 0; //pin A0 as output
    PORTC &= ~(1 << 0); //write LOW in A0
    canprint=true;
}
```

C.2 Code for Tx LED

```
#define LED_MARK 100
#define TOPBIT 0x80000000

char incomingByte='A';   // for incoming serial data
const char* data_string[]={"1 - Teste VLC, Low data-rate.","2 - LED-to-LED
    Communication.","3 - LED as Transmitter.","4 - LED as Receiver.","5 - Andre
     Bispo 31545.","6 - FCT-UNL."};
char bufCustom[20];
String customString;
char hello[]="Hello!";
int string_size, i=0, j=0, dimming=50, pwm_LED=600, string_number=0, k=0;
volatile int dimming_LED=2000;
volatile int mode=1;
unsigned long previous, current;
boolean tempo=false, val=false, can_loop=false, string_available=false, DATA=
    true, varCustom=false;
boolean string_begin_Tx=true, string_begin_Rx=true, mensagem_BLE=false;
long int dimLevel;
char buf[20];
int len = 0;
byte c;

void setup()
{
  DDRB |= 1 << 4; //pin 7 as output
  PORTB &= ~(1 << 4); //pull pin7 low

  //BLEMini.begin(57600);
  Serial1.begin(57600);
  Serial.begin(57600);
  delay(1000);
```

```
  for (int j = 0; j < 6 ; j++){
    Serial1.write(hello[j]);
  }
  delay(1000);
  attachInterrupt(0, int_loop, RISING);
}

void loop()
{
  if (Serial1.available() && !mensagem_BLE){ //se nao tem mensagem ja lida
        c = Serial1.read();
        Serial.write(c);
        if ((len<19) && (c!='.')){
          buf[len] = c;
          len++;
        }
        else if (len<20 && c=='.'){
          buf[len] = c;
          len=0;
          Serial.println(" Mensagem Recebida");
          mensagem_BLE=true;
        }
        else if (len==19 && c!='.'){
          len=0;
          Serial.println("Comando errado\n");
        }

  }

  //interpreta mensagem BLE
  else if (mensagem_BLE) {
    //Serial.print("Mensagem");
    switch(buf[0]) {

    //dimming
    case 'D':
      if (buf[1] == ';'){
        dimming=atoi(&buf[2]);
        if ((dimming >= 0) && (dimming <28)){
          DATA=false;
          Serial.print("D) Dimming sem dados ajustado para "); Serial.println(
              dimming);
        }
        else if ((dimming >=28) && (dimming <=100)){
          DATA=true;
          if (dimming>=78) dimming=78;
          Serial.print("D) Dimming com dados ajustado para "); Serial.println(
              dimming);
        }
        //varCustom=false; k=0;
      }
      else   Serial.println("D) Mensagem de ajuste de Dimming com erro");
      break;
```

```
  //preset string
  case 'P':
    if (buf[1] == ';'){
      string_number=atoi(&buf[2])-1;
      if (string_number>=0 && string_number<6){
        Serial.print("P) Preset String: ");
        Serial.println(string_number+1);
        varCustom=false; k=0;
        break;
      }
    }
    Serial.println("P) Mensagem de mudanca de string com erro");
    break;

  //new string
  case 'S':
    if (buf[1] == ';'){
      String strbuf(buf);
      customString=strbuf.substring(2,sizeof(buf));
      Serial.print("S) Nova string: ");
      Serial.println(customString);
      varCustom=true;
      k=0;
      break;
      }
    else Serial.println("S) Mensagem de mudanca de string com erro");
    break;

  //illumination only
  case 'I':
    if (buf[1] == ';'){
      dimming=atoi(&buf[2]);
      DATA=false;
      Serial.print("I) Dimming sem dados ajustado para "); Serial.println(
          dimming);
    }
    else   Serial.println("I) Mensagem de ajuste de Dimming com erro");
    break;

  //default
  default:
    Serial.println("Erro no comando");
    break;
  }
  mensagem_BLE=false;
}

if (tempo){
if (DATA && (dimming >28) && (dimming <=78)){
    dimming_LED=map(dimming,28,78,0,1990);
}
else if (DATA && (dimming==28)){
  tempo=false;
  PORTB &= ~(1 << 4);
```

```
    return;
  }
  else dimming_LED=map(dimming,0,100,0,3950);

  if (dimming!=100){
    delayMicroseconds(dimming_LED);
    PORTB &= ~(1 << 4);
  }
  else  PORTB |= (1 << 4);
    tempo=false;
  }

}


void int_loop() {
  if (DATA)  {
      PORTB &= ~(1 << 4); //pull pin 10 low
      if (!varCustom) {
        sendLED(data_string[string_number][i], 8);
        if (data_string[string_number][i]=='.') {
          i=0;
        }
        else i++;
      }
      else  {
        //customString.toCharArray(bufCustom, 20);
        sendLED(customString[k], 8);
        if (customString[k]=='.')
          k=0;
        else k++;
      }
      PORTB |= (1 << 4); //pull pin 10 high

  }
  else PORTB |= (1 << 4); //pull pin 10 high

  tempo=true;
  return;
  val=true;

}


void sendLED(unsigned long data, int nbits){

  data = data << (32 - nbits);
  spaceLED(LED_MARK);
  markLED(LED_MARK);

  for (int i = 0; i < nbits; i++) {
    if (data & TOPBIT) {
      markLED(LED_MARK);
      spaceLED(LED_MARK);
```

```
    }
    else {
      spaceLED(LED_MARK);
      markLED(LED_MARK);
    }
    data <<= 1;
  }
  PORTB &= ~(1 << 4);

}


void markLED(int time) {
  PORTB |= (1 << 4); //pull pin 10 high
  if (time > 0) delayMicroseconds(time);
}

void spaceLED(int time) {
  PORTB &= ~(1 << 4); //pull pin 10 low
  if (time > 0) delayMicroseconds(time);
}
```

APPENDIX D

LT3763 BLOCK DIAGRAM

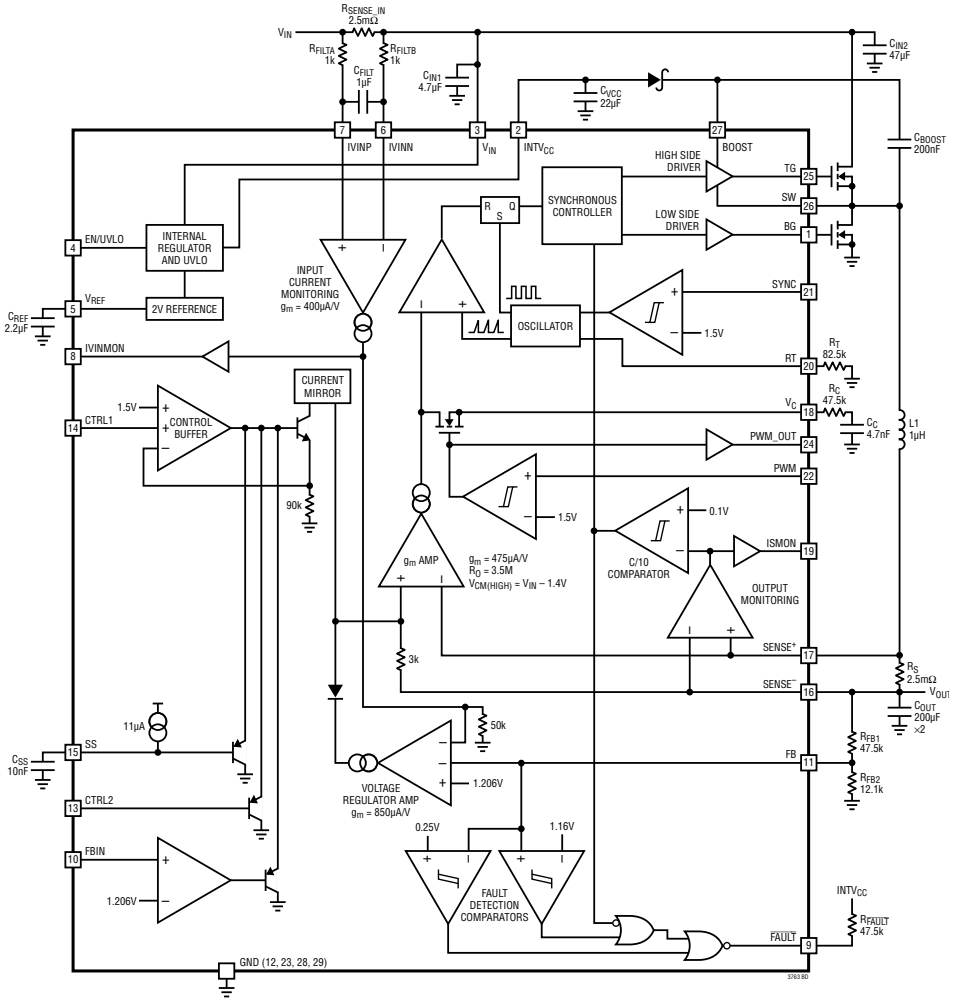

Figure D.1: LT3763 Block Diagram (from [70]).